

IMT School for Advanced Studies, Lucca
Lucca, Italy

**Numerical Modeling and Optimization of Fractured
Structures via Machine Learning and Topology
Optimization**

PhD Program in Systems Science
Track in Computer Science and Systems Engineering
XXXV Cycle

By

Tota Rakesh Kumar

2024

The dissertation of Tota Rakesh Kumar is approved.

PhD Program Coordinator: Prof. Alberto Bemporad, IMT School for
Advanced Studies Lucca

Advisor: Prof. Marco Paggi, IMT School for Advanced Studies Lucca

The dissertation of Tota Rakesh Kumar has been reviewed by:

Prof. Jose Antonio Reinoso Cuevas, Universidad de Sevilla

Prof. Pattabhi Ramaiah Budarapu, Indian Institute of Technology Bhubaneswar

Prof. Flavia Libonati, University of Genoa

IMT School for Advanced Studies Lucca
2024

Dedicated to the memory of people affected by COVID-19

Contents

List of Figures	x
List of Tables	xvi
Acknowledgements	xviii
Abstract	xxi
1 Introduction	1
1.1 Recent advancement in computational fracture mechanics	1
1.2 Importance of phase-field fracture parameters	2
1.3 Machine learning perspective to anisotropic phase-field models for fracture	4
1.4 Investigation on the strength of bonded cohesive interfaces	6
1.5 Damage tolerant structures to improve fracture resistance .	8
1.6 Research Objectives	12
1.7 Outline of the thesis	15
2 Theory and numerical implementation of Fracture Mechanics models	16
2.1 Phase-field modelling of fracture	17
2.1.1 Theoretical background	17
2.2 Finite element implementation of the phase-field approach	21
2.2.1 Isotropic case	22
2.2.2 Strain energy split decomposition method	24
2.2.3 Anisotropic case	27

2.3	Phase-field formulation for topology optimization problems	27
2.4	Graded cohesive zone interface model	29
2.4.1	Finite element formulation	30
2.4.2	Constitute model for cohesive interfaces	32
2.5	Optimum functional grading properties of cohesive inter- faces	35
2.5.1	Analysis of a linearly graded cohesive interface . .	35
3	Data-driven models for the identification of fracture mechanics parameters	40
3.1	Theory on metaheuristic algorithms	41
3.2	Fracture parameters identification using PSO algorithm . .	43
3.2.1	Identification of phase-field fracture parameters . .	44
3.2.2	Particle swarm optimization methodology	49
3.2.3	Identification of cohesive zone graded interface prop- erties	53
3.3	Comparison of machine learning techniques	57
4	Topology optimization methods for structural problems	65
4.1	Mathematical formulation of topology optimization	66
4.1.1	Filtering technique	67
4.1.2	Benchmark tests for structural topology optimization	68
4.2	Topology optimization of substrates prone to delamination	74
4.2.1	Impact of volume fraction	75
4.2.2	Examples	76
4.3	Mathematical formulation for topology optimization ap- plied to phase-field fracture	83
4.4	Non linear system sensitivity analysis	85
4.5	Examples	89
5	Machine learning applied to polymer materials	103
5.1	Application to ABS co-polymer	104
5.1.1	Uni-axial tensile tests	104
5.1.2	Three-point bending tests	106
5.2	Applications to 3D printing PLA material	112

5.2.1	Experimental characterization	113
5.2.2	Parameters' identification and sensitivity analysis .	117
6	Conclusions and future developments	124
6.1	Conclusion on identification of fracture parameters	124
6.1.1	Investigation on phase-field fracture parameters . .	125
6.1.2	Investigation on cohesive zone interface parameters	127
6.2	Conclusion of topology optimization of fracture resistant structures	127
6.3	Future developments	129

List of Figures

1	(a) Schematic representation of the continuum Ω with a crack Γ and boundaries $\partial\Omega^u, \partial\Omega^t$. (b) Approximation of the sharp crack into a diffusive region of width l_c , where Φ denotes the phase-field damage variable.	18
2	Illustration of the staggered scheme to solve the coupled nonlinear phase-field problem.	24
3	Schematic representation of a zero thickness interface element.	31
4	Tvergaard exponential law cohesive zone model	34
5	Linear graded interface model: critical cohesive normal and tangential gaps, g_{n_c} and g_{t_c} for complete decohesion vs. interface position x/L , where L denoted the maximum extension of the interface. The curve in blue shows the value of the parameters for an interface with uniform properties averaged over the interface length.	35
6	Model sketch of the peeling test.	36
7	Reaction force P versus imposed displacement for a linearly graded interface in comparison to an interface with uniform properties.	37
8	Comparison of normal tractions vs. position for a linearly graded interface and an interface with uniform interface properties for different far-field prescribed displacements increasing in the curves from red to light blue.	39

9	Benchmark problem: geometry, loading and boundary conditions.	45
10	Cost function vs. No. of PSO iterations for the benchmark test.	45
11	Scatter representation of particles in the iterations of the PSO algorithm for the benchmark test problem.	47
12	Force-displacement curve and target curve.	48
13	Convergence study of the PSO algorithm for cases 4, 7, and 8, see Table. 2.	50
14	Scatter representation of particles' position for cases 4, 5, and 6 whose parameters are collected in Table. 2.	51
15	Scatter representation of particles' position for cases 1, 2, and 3 whose parameters are collected in Table. 2.	52
16	Model sketch of the peeling test.	54
17	(a) Cost function vs. number of PSO iterations; (b) comparison between PSO identified response and target response at convergence for the peeling test problem with a linearly graded interface.	55
18	Position of the particles during the progress of the iterations of the PSO algorithm applied to the peeling test problem with a linearly graded interface.	56
19	Geometry and boundary conditions of the tensile test problem for an edge notched specimen.	58
20	Geometry and boundary conditions of the SENB test problem.	59
21	Comparison of the particles' position predicted by the different optimization algorithms for the tensile test problem with an edge-notched specimen. Not all the algorithms converge to the target response shown with a red star.	62
22	Comparison of the particles' position predicted by the different optimization algorithms for the SENB test problem. Not all the algorithms converge to the target response shown with a red star.	63

23	Force vs. displacement curves at the end of the execution of the different optimization algorithms; the target response is highlighted by blue stars.	64
24	Cost function vs. number of iterations for the different meta-heuristic algorithms.	64
25	Structural topology evolution of cantilever beam subjected to point load	69
26	Structural topology evolution of cantilever beam subjected to uniformly distributed load	70
27	Structural topology evolution of simple supported beam subjected to point load	71
28	Structural topology evolution of simple supported beam subjected to uniformly distributed load	72
29	Structural topology evolution of L-bracket subjected to point load	73
30	Sketch of peeling test with boundary conditions for a substrate with a delaminating interface, where the topology of the substrate has to be optimized to maximize the stiffness of the mechanical system for different levels of delamination.	74
31	Comparison of compliance value with respect to number of design iterations for different volume fractions f	77
32	Trend showing mean compliance (C) as a function of volume fraction (f)	77
33	Flow chart showing combined FEM-TO algorithm for topology optimization of substrate in correspondence of different portions of initial delamination along the interface.	78
34	Optimized substrate topology for different volume fractions.	79
35	Structural topology evolution of the substrate for an interface with initial debonding of 0.08 mm.	79
36	Structural topology evolution of the substrate for an interface with initial debonding of 0.2133 mm.	80

37	Sketch of L-shape structure with boundary condition and loading for a substrate with a delaminating interface, where the topology of the substrate has to be optimized to maximize the stiffness of the mechanical system for different levels of delamination.	81
38	L-shape structural topology evolution of the substrate section for an interface with initial debonding of 0.14 mm. . .	82
39	L-shape structural topology evolution of the substrate section for an interface with initial debonding of 0.2 mm. . . .	83
40	Geometry, boundary conditions and meshing details of already fractured composite plate subjected to incremental traction load along x-direction	91
41	Topology evolution of inclusion region ($v^{inc} = 10\%$) and respective crack pattern for induced damaged structure of test problem 1	92
42	Reaction force-displacement curve of the already fractured structure for the initial and final optimized design ($v^{inc} = 10\%$) for test problem 1	93
43	Fracture resistance and crack growth of the initial design and final optimized inclusion phase design ($v^{inc} = 10\%$) of test problem 1	94
44	Geometry, boundary conditions and meshing details of already fractured plate subjected to incremental normal load along y-direction	95
45	Topology evolution of inclusion region ($v^{inc} = 10\%$) and respective crack pattern for a predefined matrix region of test problem 2	96
46	Reaction force-displacement curve of the already fractured structure for the initial and final optimized design ($v^{inc} = 10\%$) of test problem 2	97
47	Fracture resistance and crack growth of the initial design and final optimized inclusion phase design ($v^{inc} = 10\%$) of test problem 2	98

48	Geometry, boundary conditions and meshing details of already fractured plate subjected to incremental normal load along y-direction	99
49	Topology evolution of inclusion region ($v^{inc} = 10\%$) and respective crack pattern for induced damaged structure of test problem 3	100
50	Reaction force-displacement curve of the already fractured structure for the initial and final optimized design of test problem 3 ($v^{inc} = 10\%$)	101
51	Fracture resistance and crack growth of the initial design and final optimized inclusion phase design ($v^{inc} = 10\%$) concern test problem 3	101
52	Flow chart showing combined PFF-TO algorithm for topology optimization of initial damaged structures to enhance crack resistance.	102
53	Photo of the specimen, dimensions and boundary conditions, FE mesh.	105
54	Experimental and numerical simulation results identified (corresponding to the identified model parameters).	106
55	Experiment specimen and geometrical details (in mm), loading, boundary condition, meshing details of a numerical model for three-point bending loading case	108
56	Mesh convergence study for 3pt bending PF simulation.	109
57	Representation of experimental and numerical simulations of 15 force-displacement curve results.	109
58	Comparison between numerical results with parameters identified: (i) from uni-axial tensile tests ($l_c = 1.37$ mm, $E = 1157.90$ MPa, $G_C = 7.5$ N/mm); (ii) from notched three-point bending tests ($l_c = 0.35$ mm, $E = 1153.07$ MPa, $G_C = 8.85$ N/mm). The comparison highlights that it is necessary to identify the AT2 PF model parameters independently for each type of test.	111
59	SolidWorks generated CAD geometry models	112

60	Photos of the 3D printed PLA specimens.	115
61	Experimental stress-strain curves from tensile tests.	116
62	Finite element mesh of the simulated SENB tests.	118
63	Sensitivity analysis of anisotropic phase-field fracture parameters	118
64	force - displacement curve for $\theta = 0^\circ$, and different β values	119
65	Force vs. displacement curves for different test cases ($\alpha = 0^\circ, \beta = 25$) as mentioned in Table. 11	122
66	SENB geometric model with meshing details for case $\alpha = 0^\circ, \beta = 25$	123
67	force-displacement curve for SENB numerical problem (see Fig. 66) for case $\alpha = 0^\circ, \beta = 25$	123

List of Tables

1	Degradation function $g(\Phi)$ to be satisfied without violating the damage mechanics process.	19
2	Set of input data to generate target responses and range of parameters for the robustness test. The last column reports the error of the identified parameters with respect to the values used in input.	48
3	Input data to generate target responses and range of parameters for the search space of the identification algorithms. 59	
4	Material properties of the matrix and inclusion phase during numerical simulations	90
5	PSO identified E and l_c parameters for the 15 tests in Fig. 54, with their mean and standard deviation values.	107
6	PSO identified E , G_c and l_c parameters for the 15 tests in Fig. 57, with their mean and standard deviation values.	111
7	Process parameters for the DIVIDE_ BY ZERO AION 500 MK2 3D printer.	113
8	Experimental data obtained by processing the tensile and the SENB tests of 3D printed PLA material.	116
9	Set of input data to generate target responses and range of parameters for the sensitivity analysis of the anisotropic fracture tensor.	119

- 10 Sensitivity analysis of β and percentage (%) change in P_{max} , G_c values for different values of β with respect to case - $\alpha = 0^\circ, \beta = 0$ 120
- 11 Showing test cases involving varying crack density functions with and without the application of a correction factor for conducting PFF numerical test ($\alpha = 0^\circ, \beta = 25$). . . 122

Acknowledgements

I would like to express my deep and heartfelt gratitude to my respected guide and mentor, Prof. Marco Paggi, for his valuable advice, support, good wishes, and encouragement throughout my PhD journey. His expertise, patience, and encouragement have been instrumental in shaping my research and academic development. During the meetings and his FraMCoS-XI conference visit to India, the insightful technical discussion I had with him about research and its progression enriched my research experience and prepared me for future endeavors in my field.

I am profoundly grateful to the members of my doctoral committee, Prof. Jose Antonio Reinoso Cuevas, Prof. Pattabhi Ramaiah Budarapu, and Prof. Flavia Libonati, for their valuable comments on the improvement and refinement of my PhD thesis. I sincerely appreciate their dedicated time and effort in reviewing my PhD thesis work.

I extend my sincere thanks to IMT School for Advanced Studies Lucca, Italy, for providing me with the opportunity and resources to pursue my PhD studies. During my stay at Lucca, the research environment, library facilities, and support from PhD office at IMT have been phenomenal. I also would like to thank IMT friends for the discussions and parties.

I would like to extend my heartfelt thanks to my family, particularly my parents and in-laws, for their support and understanding throughout my PhD journey. It is worth mentioning my wife's patience, understanding, and belief in me, which have been invaluable, providing the foundation upon which I could pursue and achieve this significant milestone.

I am deeply thankful for her sacrifice, love, and time, which have been instrumental in shaping my academic and personal growth.

Journal Publications

1. Tota Rakesh Kumar, Marco Paggi (2023) - "A robust identification procedure for phase field fracture mechanics parameters" - Theoretical and Applied Fracture Mechanics, ISSN 0167-8442, vol. 127, pp. 104005.
doi=<https://doi.org/10.1016/j.tafmec.2023.104005>
2. Tota Rakesh Kumar, Marco Paggi (2024) - "Data-driven and physics-based methods to optimize structures against delamination" - Mechanics of Advanced Materials and Structures, pp. 1-17.
doi = <https://doi.org/10.1080/15376494.2024.2372696>.
3. Tota Rakesh Kumar, Marco Paggi (2024) - "Anisotropic phase-field fracture: a machine learning perspective" submitted and under review, available at SSRN: <http://dx.doi.org/10.2139/ssrn.4861857>
4. Tota Rakesh Kumar, Marco Paggi (2024) - "An integrated topology optimization and phase-field approach for the design of defect tolerant structures" - under preparation.

Conference Publications

1. Tota Rakesh Kumar, and Marco Paggi. "A pso identification procedure for phase-field fracture mechanics parameters" - 11th International Conference on Fracture Mechanics of Concrete and Concrete Structures (FraMCoS-11) on September 10-14, 2023 at IISc Bangalore, India.
2. Tota Rakesh Kumar, Marco Paggi. "Structural Topology Optimization Of Fractured Materials"- 6th National Conference on Multidisciplinary Design, Analysis, and Optimization on December 6-8, 2023 at IIT Guwahati, India.

Abstract

During the continuous development of science and technology, optimization plays a tremendous role in improving our resources without compromising the quality of performance.

This thesis work investigates the application of the phase-field method for fracture (PFF) in brittle materials, focusing on the understanding of the influence of the model parameters, both for the isotropic and the anisotropic cases, in capturing the mechanical response of experimental results. For the PFF isotropic case, an experimental investigation was carried out on an ABS co-polymers. A MATLAB-based algorithm combining particle swarm optimization (PSO) with PFF has been utilized to determine optimal values of Young's modulus (E), fracture toughness (G_c), and the PFF internal length scale (l_c) through uni-axial tensile and three-point bending tests. To understand the potential of bio-polymers in various industrial applications, 3D printed PLA materials were fabricated via fusion deposition modeling, and due to their anisotropic behavior, an anisotropic PFF approach was exploited. A metaheuristic machine learning algorithm coupled with PFF demonstrates robustness in estimating fracture parameters (G_c , l_c , β) and a strong influence of β the penalty parameter on the predicted force-displacement curves.

The thesis examine also the critical issue of delamination at internal interfaces/adhesive joints and internal cracks in composite and multi-material components, which can lead to catastrophic failures. Existing structural topology optimization (TO) methods typically assumes perfect bonding, which urges the development of approaches that explicitly optimize struc-

tures against delamination. The proposed data-driven heuristic optimization strategy has been applied to identify optimal cohesive interface properties with linear grading, enhancing the composite structure's resistance to peeling. Additionally, it explored the application of the Solid Isotropic Material with Penalty (SIMP) topology optimization approach to optimize substrate internal structures affected by interface delamination.

The integration of a phase-field for fracture (PFF) approach with TO has been highlighted as a robust mathematical framework to mitigate crack progression in structures compromised by initial damage under operational loads. Employing the SIMP technique and optimality criteria (OC) method, the research validated its effectiveness through numerical examples, demonstrating potential improvements in fracture resistance for damaged structures crucial in aerospace, marine, automotive, and civil engineering industries.

Nomenclature

Acronyms

2D	Two dimensional space
ABC	Ant Bee Colony
ABS	Acrylonitrile Butadiene Styrene
CS	Cuckoo Search
CZI	Cohesive Zone Interface
CZM	Cohesive Zone Model
FDM	Fused Deposition Modelling
FEA	Finite Element Analysis
FEM	Finite Element Method
GA	Genetic Algorithm
MLA	Machine Learning Algorithm
PPF	Phase-Field for Fracture
PLA	PolyLactic Acid
PMMA	Poly Methyl MethAcrylate
PSO	Particle Swarm Optimizaition

SENB	Single Edge Notch Bending
SIMP	Solid Isotropic Material with Penalization
STD	Standard deviation
TLBO	Teaching Learning Based Optimization
TO	Topology Optimization

Variable notation

\mathbf{u}	Displacement field
K	stiffness
E	Young's modulus
ν	Poisson ratio
Φ	Phase-field variable
ϕ	Design variable
σ_n	Normal traction
τ_t	Tangential traction
Υ	PSO target cost function
G_c	Fracture energy
g_{n_c}	Critical normal gap
g_{t_c}	Critical tangential gap
l_c	Internal length scale parameter

Chapter 1

Introduction

Chapter 1 is partially based on the content of publications [1, 2] and article in press [3].

1.1 Recent advancement in computational fracture mechanics

The phase field approach to fracture is an emerging computational technique for simulating complex crack paths in solids and structures. The development of numerical methods within the Finite Element Analysis (FEA) to predict fracture onset, propagation, and branching in materials and structures has been the subject of intensive research since the 1970s. Those methods are requested to tackle technical problems that analytical techniques cannot address. In this regard, the Cornell Fracture Group [4] developed FEA software based on linear elastic fracture mechanics (LEFM). These methods included inserting singular finite elements at the crack tip to approximate the singular stress field and compute the stress-intensity factors according to the displacement correlation technique or the J-integral method. Although efficient for 2D problems, the extension of the methodology to 3D geometries, also with multiple materials, is quite complex since the theoretical definition of the generalized stress-intensity factors and the implementation of the related computational

procedures require a significant effort [5].

Alternatively, Continuum Damage Mechanics (CDM) models accounting for a smeared crack representation [6] can address both crack nucleation and propagation stages. To avoid mesh dependency of local damage formulations, integral-based nonlocal and gradient-enhanced procedures have been proposed [7, 8, 9, 10, 11]. Moreover, extended FE strategies with nodal kinematic enrichment (extended-FEM, X-FEM) that rely on Partition of Unity Methods (PUM) [12, 13, 14] and element enrichment formulations (enhanced-FEM, E-FEM) [15, 16, 17, 18] have also seen a considerable development. These methods present limitations for simulating complex failure modes that require predicting crack initiation, propagation, branching, and coalescence from multiple points.

In this regard, the phase field (PF) approach to fracture proposed in [19] based on Γ -convergence [20] presents several advantages. The above approach incorporates a non-local formulation that can retrieve the classical energy-based Griffith criterion [21] as a limit case when the internal length scale of the model tends to zero. Significant progress has been made regarding the numerical implementation of the phase field approach to fracture in FEA codes, see e.g. [22, 23, 24]. This methodology appears to be very promising in reproducing not only the limit case of LEFM but also diffuse damage scenarios depending on the choice of the model parameters.

1.2 Importance of phase-field fracture parameters

The phase field fracture parameters play a significant role in predicting crack growth and direction and mechanical response of the structure quantitatively. The phase field methodology described in Section 2.2.1 has been tested in relation to real experiments on brittle PMMA samples with notches and holes in [25]. Results have shown that the phase field approach to fracture can closely reproduce the experimental results not only in terms of the crack pattern but also in terms of force displacement and local stress measures. In [25], parameters' identification for each

type of simulated test was conducted manually. Still, preliminary results showed significant concerns, especially for the popular AT2 phase field model (see [26]). Specifically, the internal length scale of the phase field approach was quite a complex parameter to be identified.

The value of the peak traction in a simulated uni-axial tensile test is affected by the choice of the internal length scale of the phase field model. A possible correlation between material strength (σ_c) and the internal length scale (l_c) can be formally established, see [26], which has led to the wide belief that l_c estimated from uni-axial tensile tests can be consistently valid also for any other geometry and loading conditions. This belief has been questioned in [25], where manual identification of the internal length scale for all the conducted tests on PMMA samples with different geometry and loading conditions has shown that, especially for the AT2 model, it is not possible to use the value of the uni-axial tensile tests to reproduce all the experimental trends accurately. This motivates the need to develop a robust identification procedure to extract the optimal value of the internal length scale directly from experimental results. In the literature, [27] applied the Bayesian approach to estimate the phase field model's bulk and shear moduli, tensile strength, and fracture toughness to match the three-point bending test experimental result data. In the above work, to calculate the internal length scale parameter, an expression for the uni-axial case mentioned in [26] is used, and no information about how to choose the internal length scale parameter for the phase field model if there is a change in geometry and loading condition. Thus, an automatic identification procedure is required and can be applied to evaluate the internal length scale parameter of the phase field model directly from the experimental data for conditions different from the uni-axial tensile tests.

Therefore, in Section 3.2, we propose a robust material parameters' identification procedure for the phase field approach to fracture based on Particle Swarm Optimization (PSO). This heuristic approach has been demonstrated to be extremely robust in the case of mechanical problems involving multiple nonlinearities, as shown in [28], such as plasticity and cohesive fracture. Therefore it is considered an excellent candidate also

for phase field diffuse damage.

1.3 Machine learning perspective to anisotropic phase-field models for fracture

Over the past years, additive manufacturing (AM), also known as 3D printing, has become a very popular field and revolutionized the manufacturing industry with supremacy over conventional processes in creating complex structures [29, 30] with polymers, ceramics, metals, and also composites materials. AM played a significant role in Industry 4.0 by reducing material wastage and promoting a sustainable, cleaner production process, a subject of interest in academia and industry [31]. In this regard, different types of additive manufacturing techniques and methods developed and successfully implemented at the industry level such as selective laser melting (SLM) [32], selective laser sintering (SLS) [33], fused filament fabrication (FFF) [34], fused deposition modeling (FDM) [35], direct energy deposition (DED)[36] etc. Among the above-mentioned methods, FDM has mostly adopted technique [37] in the engineering field because the components produced by the FDM process [38] are maintained of high quality with excellent retention of mechanical properties and also maintain good dimensional accuracy with repeatability. FDM works on the layer-by-layer concept in which the 3D-printed material is extruded from a nozzle tip in a semi-solid state, deposited on a substrate, and then allowed to solidify, resulting in a solid 3D-printed part.

The mechanical strength behavior of various 3D printed polymer materials available in the market like acrylonitrile butadiene styrene (ABS), polylactic acid (PLA), polycarbonate (PC), polyethylene terephthalate glycol (PETG), and polyamide (PA) are studied [39, 40, 41, 42]. Out of the polymers mentioned above, the strength and fracture analysis of 3D printed PLA material has been investigated widely since it is eco-friendly and biodegradable. PLA can also be blended with other materials to accelerate the degradation [43, 44] and serve automobiles [45], biomedical applications [46, 47], etc. 3D printed material using the FDM method

is best suitable for bio-degradable materials [48]. The printing process parameters such as raster orientation, layer thickness, printing speed, and extruded temperature, to name a few, are to be set optimum [49] and should be maintained consistently throughout the printing process. During the experimental testing investigation; it was found that the process parameters of 3D printed PLA parts by FDM process strongly affect the mechanical and fracture strength [50, 42, 48, 51]. Even the mechanical behavior of 3D printing material changes by altering the printing orientation [52]. This motivates the study of the mechanical and fracture strength of PLA materials concerning particular printing process parameters and, in general, the numerical investigation of the anisotropic behavior of materials.

In Section 5.2.1 we conducted two experimental tests on 3D-printed PLA materials. Experimental tensile tests are conducted as per ASTM standards [53] to investigate the mechanical properties [54] such as Young's modulus E , maximum tensile strength σ_{max} . The single edge notch bending (SENB) experimental tests are conducted as per ASTM standard [55] to investigate the fracture toughness G_C of the material [56, 57]. The printing process parameters are set consistently to prepare both testing 3D printed samples. Since the PLA material in the 3D printed process is deposited layer-by-layer therefore, the material might exhibit anisotropic behavior [49, 58]. Material properties obtained from the above tests are susceptible to 3D printing process parameters, and there might be a possibility of reduction in strength by over 50 % than manufactured by injection molding process [59]. The numerical finite element analysis (FEA) based on the phase field for fracture (PFF) method described in Section 2.2.3 proposed by [60] is implemented in Section 5.2.2. The anisotropic PFF closely imitates the fracture behavior of 3D-printed PLA materials.

Since 3D printed materials experience anisotropic behavior, therefore anisotropic structural tensor ω should be incorporated in the crack surface density function term [61, 62] of phase field formulation [60]. The anisotropic tensor term contributes to the directionality of the crack evolution and consists of penalty parameter β that significantly influences the crack orientation [63] during crack propagation. Several researchers

[64, 65, 63, 66] studied the crack propagation phenomenon exploiting anisotropic phase field for fracture numerical models. To the best of the author's knowledge, the crack path due to anisotropic behavior has been studied intensively. However, how the effect of penalty parameter β influences the global force-displacement response of the experimental results is an open question yet to be investigated. In Section 5.2.2, the author analyzed the effect of this value β by using a parameter identification procedure using the inverse method to match the target force-displacement curve to a numerically simulated response. The material parameters E , G_C , β , l_C are identified by minimizing the user-defined cost function. In the literature, particle swarm optimization (PSO)[67] algorithm is applied to fracture[68] and interface [69] problems to identify respective parameters. The question arises of which metaheuristic optimization algorithm best suits fracture parameter identification problems. In this direction, Section 3.1 explored evolutionary machine learning algorithms (MLA) such as PSO [70, 67], PSO-GA [71], ABC-PSO[72, 73], CS[74], TLBO [75], and EJAYA[76, 77] are applied to isotropic PFF ($\beta = 0$) test problems. In Section 3.3, all metaheuristics algorithms are compared to find the best efficient algorithm in identifying phase-field fracture mechanics parameters. After that, the best algorithm obtained was applied to the proposed combined approach PFF-MLA to determine the effect of penalty parameter β in identifying target input fracture mechanics parameters.

1.4 Investigation on the strength of bonded cohesive interfaces

Material components are often bonded together by adhesive materials, and they play a major role in determining the strength of the whole assembly for aerospace, automobile, fashion industry, and many other industrial sectors. Peeling tests are routinely performed to assess the quality of bonding and determine the adhesive properties requested to withstand applied loading. The peeling test gives in output the peeling force required to delaminate a deformable layer/film from the sub-

strate. As compared to a fully bonded interface where the continuity of tractions and displacements is guaranteed at the material discontinuity, the response of an adhesive interface evolves during debonding, with a progressive separation and tractions that are nonlinearly function of the displacement discontinuities [78, 79]. The expression of the traction-separation relation is usually called cohesive zone model (CZM), see [80, 81, 82, 83, 84, 85] for some relevant examples and functional relations.

Analytical solutions for peeling tests addressing the mixed-mode deformation problems have been notably derived in [86, 87, 88]. Other relevant contributions towards the understanding of the mechanics and failure of cohesive interfaces in statics and dynamics, among the many published in the literature, are those in [89, 90, 91, 92, 93]. In terms of computational methods, the CZM for adhesive interfaces can be efficiently implemented within the finite element method (FEM) according to an intrinsic approach, duplicating the nodes of finite elements sharing an interface and inserting zero-thickness interface finite elements along the adhesive interface. In case of non-conforming meshes, node-to-segment interface elements can be considered as well, as shown in [94]. The method is robust in handling non-linear problems using a full-implicit Newton-Raphson incremental-iterative scheme.

In this thesis, the exponential CZM formulation in [82] is adopted to describe the nonlinear response of an adhesive joining a bi-material system which may undergo delamination as mentioned in Section 2.4.1. Instead of setting all the parameters of the CZM, which are the peak tractions in Mode I and Mode II, and the critical normal and tangential gaps for complete decohesion (or, analogously, the Mode I and the Mode II fracture energies which are functions of the above parameters), we explore here the possibility to identify optimal properties of the interface to preserve the response of the composite even in presence of evolving debonded regions. Specifically, the possibility of a functionally graded interface with a linear variation of fracture energy along the interface coordinate is explored, motivated by the fact that such kind of interfaces could be technologically manufactured by acting on their microstructure, for instance by varying the geometry and/or the density of mushroom

micro-pillars in Gecko's bio-inspired adhesives [95, 96, 97, 98, 99, 100]. The main objective is assessed in Section 2.5 to estimate the potential of such functionally graded interfaces in withstanding debonding, to make the composite material delamination-tolerant.

Therefore, the material parameter identification of the CZM parameters becomes an inverse problem. To solve it, non-gradient-based algorithms which can be included within a category of *data-driven* approaches are genetic algorithms [101]: particle swarm optimization [102], Cuckoo search algorithm [103], evolutionary algorithms [104], teaching and learning based algorithm [105], to name a few. In the literature, data-driven machine learning models [106, 107, 108, 109] have been employed to gain insights into the traction-separation relationship and the underlying physics of interface problems. Several researchers [110, 111, 112, 113] worked on non-gradient optimization models for inverse parameter identification of cohesive zone interface properties. In Section 3.2.3, the particle swarm optimization (PSO) algorithm is employed since it has already been proven to be efficient for non-convex, strongly nonlinear problems in the context of plasticity and cohesive fracture [28] and for material identification problems in phase field fracture [1].

1.5 Damage tolerant structures to improve fracture resistance

Over the past years, engineering product design tools paved a novel approach to additive manufacturing [114, 115] using 3D printing technology [116]. The mentioned technology creates a complex lightweight structure by topology optimization (TO) approach without violating human requirements, less impacting the economy and environment. Virtual prototyping [117, 118] extends further development to visualize structure before manufacturing the product. In this line of research to create such structures, topology optimization is the powerful numerical optimization technique that attracted researchers and scientists to study further materials in general and engineering structures in particular. The foundation of the TO approach was laid down by Bendsoe and Kikuchi,

which is based on the homogenization method [119]. From then on, several TO methods evolved such as density-based Solid Isotropic Material with Penalization (SIMP) [120], evolutionary structural optimization (ESO) [104, 121], bidirectional evolutionary structural optimization (BESO) [122, 123], level-set [124] e.t.c., to name a few. These TO methods have been extensively used in engineering design to determine the most efficient material layout within a given design space for a given set of loads, boundary conditions, and constraints to maximize the system's performance. This versatile tool has undergone thorough investigation and utilization across various fields, encompassing designs with geometric nonlinearity [125], materials with elastoplastic properties [126, 127], structures influenced by thermal elasticity [128], and, most significantly, in the topology optimization of structures affected by cracking [129]. The utilization of topology optimization in enhancing structure fracture resistance represents a dynamic and growing area of study. It opens up innovative opportunities for creating more robust, lighter structures than traditional designs. TO applied to fracture materials has significant potential for ongoing research and advancements in structural engineering.

We examine the well-known phase-field for fracture (PFF) method to comprehend structural fractures. The phase field (PF) approach to fracture simulation, introduced by Francfort and Marigo [130] and further developed by Bourdin [131], perfectly aligns with the principles of brittle fracture, employing variational techniques that focus on minimizing energy [132]. The robust numerical implementation of the PFF by Miehe [23] is renowned for its computational efficiency in managing intricate crack patterns. The phase field method has several advantages over traditional fracture mechanics approaches [133, 134, 135, 136, 137]. It can naturally handle complex crack patterns, including branching and merging, and does not require remeshing as the crack evolves. This makes it suitable for simulating fracture in heterogeneous materials [138] and complex geometries [139]. Recent advancements in phase field modeling have extended its application to various materials and loading conditions, including brittle [140, 141], ductile [142, 143], polymers [1], ceramics [144] and fatigue fracture [145, 146, 147]. The PF method's flexibility

and robustness make it a powerful tool for predicting material failure and designing structures with improved fracture resistance using TO.

The fundamental aim of TO is to enhance the material's resistance to crack initiation and propagation. This involves designing materials or structures that can withstand significant stress and strain without failing. The final outcome of the TO process is typically targeted to improve the material's mechanical properties, such as toughness, strength, stiffness, etc. It may also involve the design of microstructural features [148, 149] that can help to prevent or delay the onset of fracture. Recent developments in TO methods applied to fracture resistance structures investigated complex physical phenomena such as plasticity [150], damage mechanics [151], composite structures [152, 153], functional graded materials [154] as well as the explicit modeling of dynamic crack propagation [155, 156]. These advancements have opened up new possibilities for designing strong materials capable of energy dissipation and crack growth resistance. We believe that topology optimization of structural material with initial induced damage due to a certain load to resist crack growth is an unexplored area of research.

Therefore, in Section 4.3, we proposed a combined PFF-TO method to find the TO of already damaged structures. The PFF approach is initially applied on an intact structure (without damage) up to a certain load called a service load. It leads to some damage to the structure. Then, the TO approach is applied to the initial damage configuration, quantifying how the material is distributed to such an initial damage in the structure. Finally, the PFF approach is applied to the optimized structure to assess how the internal material arrangement delays crack propagation in improving mechanical properties. There are numerous TO methods available in the literature to tackle fracture problems. For example, topology optimization (TO) employing the Solid Isotropic Material with Penalization (SIMP) method has been integrated with the phase field fracture (PFF) approach [157, 153, 155, 158] to monitor crack propagation. In certain studies, the PFF method has been substituted with the peridynamics (PD) approach [159, 160], extended finite element method (X-FEM) [161] to study the crack resistance in the structure. Alternatively, the level-set

method [162] and BESO [152, 163, 156] are incorporated through integration with PFF to develop structures resistant to cracking. In the aforementioned studies, the design variables of the structure are updated during the topology optimization (TO) process using either the optimality criteria (OC) method [164] or the method of moving asymptotes (MMA) [165]. In Section 4.5, we employed the TO method based on the SIMP approach [164] and worked on test problems to maximize the structure's stiffness to a pre-defined material volume fraction.

The second objective of the Section 1.5 is to assess the possibility to make a bi-material component with an imperfect adhesive interface tolerant to interfacial defects by acting on the optimization of the topology of the surrounding continuum. Topology optimization is carried out for this class of inverse problems based on physics-based simulated data. Relevant publications on topology optimization (TO) used in simpler contexts without fracture are [166, 167, 168, 169]. The technique is usually applied to design lightweight structures preserving the mechanical response [170]. The Optimality Criteria (OC) [171] are employed here to solve the topology evolution of structural problems within the design constraints. In recent research, TO has been effectively applied to enhance the toughness of heterogeneous adhesive films [172] by strategically arranging stiff and soft material blocks and in the other work exploring functionally graded materials in the context of phase-field fracture [173].

In Section 4.2, we seek topology optimization of the substrate corresponding to a certain portion of the deformable layer peeled off. The interface response is described by a linearly graded CZM, as analyzed in Section 2.5.1. The substrate stiffness is considered an objective function with volume constraints. The sensitivity analysis of the objective function with respect to the design variable is carried out, and the OC method is applied to evolve the design variable with design iterations until the user-defined condition is met. Finally, the optimized substrate topology is determined. The evolution of the optimal substrate topology patterns for different amounts of interface delamination is also investigated to assess the robustness of the identified topology under perturbations in the

extent of the onset of delamination.

1.6 Research Objectives

The AT-2 phase-field model for fracture is a popular method for simulating crack propagation in materials due to its ability to smoothly represent crack surfaces, maintain thermodynamic consistency, and handle complex geometries and diffuse damage without explicit crack tracking or specialized techniques. However, the model also has several limitations, including high computational costs due to mesh dependency, sensitivity to fracture parameter selection, lack of inherent control over crack directionality. Additionally, it may struggle with accurately capturing complex crack interactions and requires higher-order discretization schemes to avoid numerical artifacts. Despite its strengths in robustness and flexibility, these weaknesses necessitate careful management of computational resources and fracture model parameters. In this direction the primary objectives of this thesis is to investigate numerical fracture models in brittle materials to gain a deeper understanding of how model parameters affect the mechanical behavior of structures, with a focus on accurately replicating experimental outcomes, including crack patterns, delamination fractures, and force-displacement responses. Additionally, the thesis explores structural topology optimization for enhancing material resistance to fracture and delamination in interface structures. The detailed research objectives are outlined below

Objective 1:

The phase-field method for fracture has been tested on isotropic brittle materials in the literature with notches and holes, demonstrating its ability to accurately reproduce experimental results in terms of crack patterns, force displacement, and local stress measures. However, manual parameter identification, particularly for the AT2 phase-field model, revealed challenges in determining the internal length scale parameter (l_c), which is influenced by geometry and loading conditions. Traditional approaches using fracture parameters from uniaxial tensile tests are not universally applicable to other geometrical and loading conditions, high-

lighting the need for a more robust identification procedure for varying geometry and loading conditions. This study achieves the objective by proposing the implementation of Particle Swarm Optimization (PSO) for the automated and accurate material parameter identification in phase-field models, which are well-suited for capturing diffuse damage in complex mechanical problems.

On the other hand researchers in the literature has extensively studied crack propagation using anisotropic phase-field fracture models. The specific impact of the penalty parameter β on the mechanical response has not been thoroughly investigated. To address the research gap, this study utilizes an inverse parameter identification procedure integrated with a phase-field fracture (PFF) model and evolutionary machine learning algorithms (MLAs) such as Particle Swarm Optimization (PSO) to accurately identify fracture parameters. The outcome of this work determines β value needs to be properly investigated for good prediction of quantitative results in addition to qualitative analysis of the crack path.

Objective 2:

In this objective, the research gap lies in the challenge of accurately identifying the optimal cohesive zone model (CZM) parameters for adhesive joints in bi-material systems, particularly under conditions of evolving debonded regions. Traditional methods for setting CZM parameters, such as peak tractions in Mode I and Mode II, and critical gaps for decohesion, do not fully address the complexities of functionally graded interfaces that can enhance delamination resistance. Existing approaches often overlook the potential of interfaces with graded fracture energy profiles, which can be technologically realized through microstructural variations, such as those inspired by Gecko's bio-adhesives. To bridge this gap, the study proposes an inverse problem formulation for the identification of CZM parameters using non-gradient-based optimization algorithms, specifically the Particle Swarm Optimization (PSO) technique. PSO is chosen for its robustness in avoiding local minima, a common limitation of other optimization methods available in the literature. This approach leverages data-driven models to capture the traction-separation relationship more accurately, facilitating the development of delamination-

tolerant composite materials.

Objective 3:

Traditional topology optimization (TO) methods, such as density based approaches, level-set methods, ESO, and BESO, have primarily focused on designing lightweight structures that maintain mechanical integrity without considering the complexities introduced by imperfect adhesive interfaces and evolving damage. In the literature, TO have been extensively studied in simpler contexts without fracture, their application to problems involving interfacial defects and fracture remains underdeveloped or studied a few. The research gap addressed in this work pertains to the limited exploration of TO strategies for enhancing the tolerance of bi-material components with imperfect adhesive interfaces to interfacial defects. This study aims to fill this gap by optimizing the topology of the surrounding continuum of bi-material components to make them more defect-tolerant. The approach involves using the Optimality Criteria (OC) method, which is selected for its computational efficiency and simplicity in implementation. By employing TO based on physics-based simulated data, this work seeks to advance the understanding of material distribution strategies that enhance the toughness and fracture resistance of adhesive interfaces, ultimately contributing to the development of more resilient composite materials.

Objective 4:

Recent advancements in topology optimization (TO) methods have investigated complex structural fracture resistance phenomena in conditions of plasticity, damage mechanics, composite structures, functionally graded materials, and dynamic crack propagation e.t.c., to name a few. The TO approaches primarily focus on designing intact materials or structures to enhance mechanical properties like toughness, strength, and stiffness without considering how initial accumulated damage influences material distribution and fracture resistance. There remains a significant gap in optimizing materials or structures that already have induced damage due to operational loads. So the research gap identified in this study pertains to the limited exploration of topology optimization (TO) methods specifically tailored for structures with pre-existing dam-

age to enhance their resistance to crack initiation and propagation. This study aims to address this gap by proposing a novel integrated Phase Field Fracture-Topology Optimization (PFF-TO) methodology to optimize the topology of structures with pre-existing damage. The approach involves applying the PFF model to simulate initial damage under service loads, followed by TO to redistribute material in response to the damage configuration. The final optimized structure is then assessed for crack propagation resistance using the PFF approach to evaluate improvements in mechanical properties. By employing the Solid Isotropic Material with Penalization (SIMP) method for TO and validating through numerical benchmark problems, this work seeks to maximize the stiffness of damaged structures while adhering to material constraints, ultimately advancing the field of fracture-resistant material design.

1.7 Outline of the thesis

The content of the thesis work is organized as follows: Chapter 2 describes the theory and numerical implementation of fracture models, such as phase field for fracture in isotropic and anisotropic cases and cohesive zone interface fracture. In Chapter 3, different metaheuristic machine learning algorithms are described in detail and their application to the identification of fracture parameters. In Chapter 4, the mathematical formulation of topology optimization applied to structural problems is derived with application to optimize structures against fracture resistance. In Chapter 5, the issue of phase-field fracture parameter in capturing the mechanical response of polymer material (injection molding ABS copolymer, 3D printed PLA material) numerically is investigated. Finally, Chapter 6 concludes the thesis work by summarizing the results and suggestions for future work.

Chapter 2

Theory and numerical implementation of Fracture Mechanics models

Chapter 2 is partially based on the content of publication [1] and article in press [3].

This chapter is structured into two main sections. The first section provides a theoretical foundation for the phase-field for fracture (PFF) model as applied to polymer materials in the Chapter 5. The second section delves into the Cohesive Zone Interface (CZI) model, typically employing the traction-separation (T-S) law along the interface region. The discussion on PFF models is limited to brittle materials, considering both isotropic and anisotropic cases. A thorough explanation and derivation of governing equations, along with finite element numerical implementation, are presented based on the variational minimization principle. Subsequently, the crucial aspect of the CZM, namely the exponential traction-separation law, is discussed, followed by a description of the numerical implementation procedure of the CZI compatible with the four-noded finite element in FEM software. This section concludes with a discussion on uniform and linearly graded cohesive interface properties.

2.1 Phase-field modelling of fracture

This section gives an overview of the well-known phase-field approach to fracture generalized to handle both isotropic and anisotropic brittle materials. The underlining concept of phase-field applied to fracture emerged from the fundamental principles of Griffith theory [132] applied to brittle materials, which states that a crack propagates when the fracture surface energy needed to generate the new crack surface equals the amount of elastic strain energy released in the material due to crack growth. The mathematical expression of Griffith's total energy function Π_T includes the contribution of the internal elastic strain energy Π_E , the fracture surface energy Π_S , and the potential energy \mathcal{P} due to external loading:

$$\Pi_T := \Pi_E + \Pi_S - \mathcal{P} \quad (2.1)$$

2.1.1 Theoretical background

Let us consider a linear elastic continuum domain $\Omega \subset \mathbb{R}^B$ in the reference configuration with dimension $B \in [1, 3]$ with external boundary $\partial\Omega$ and an evolving internal cracked discontinuity $\Gamma \subset \mathbb{R}^{B-1}$. The displacement field \mathbf{u} is imposed on the Dirichlet boundary $\partial\Omega^u$ and surface tractions $\bar{\mathbf{t}}$ are applied on the Neumann boundary $\partial\Omega^t$, see Fig. 1, where $\partial\Omega = \partial\Omega^u \cup \partial\Omega^t$ and $\partial\Omega^u \cap \partial\Omega^t = \emptyset$. Body forces \mathbf{b} , if any, are applied on the continuum Ω . A crack may nucleate and propagate from existing notches or regions characterized by stress concentrations, leading to a displacement field \mathbf{u} in the body, which may present a discontinuity in correspondence with the localized propagating crack. In the phase-field approach to fracture, the sharp displacement discontinuity will be smeared out by introducing a suitable nonlocal regularization, which introduces an unknown scalar damage variable Φ in the domain. The problem reduces to find the displacement \mathbf{u} and the phase-field damage variable Φ , subject to the equilibrium conditions of the solid body, the evolution equation for damage coupled with the mechanical field, and the boundary conditions related to the specific model geometry.

The total potential energy functional of the continuum Ω proposed by Francfort-Marigo [130] with a prospective evolving crack surface Γ reads:

$$\Pi_T(\mathbf{u}, \Phi) = \underbrace{\int_{\Omega} \Psi_E(\boldsymbol{\varepsilon}(\mathbf{u}), \Phi) \, d\Omega}_{\Pi_E} + \underbrace{\int_{\Gamma} G_c \, d\Gamma}_{\Pi_S} - \underbrace{\int_{\Omega} \mathbf{b} \cdot \mathbf{u} \, d\Omega - \int_{\partial\Omega^t} \bar{\mathbf{t}} \cdot \mathbf{u} \, d\Omega^t}_{\mathcal{P}} \quad (2.2)$$

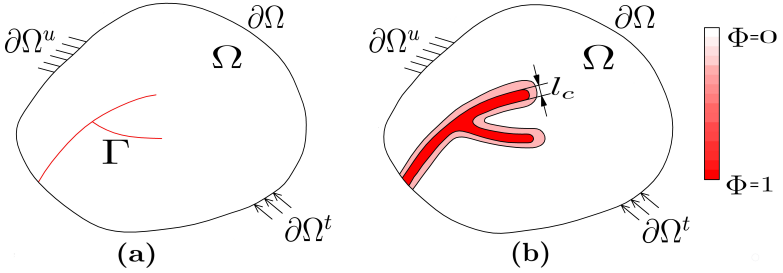


Figure 1: (a) Schematic representation of the continuum Ω with a crack Γ and boundaries $\partial\Omega^u$, $\partial\Omega^t$. (b) Approximation of the sharp crack into a diffusive region of width l_c , where Φ denotes the phase-field damage variable.

where the first term $\Psi_E(\boldsymbol{\varepsilon}(\mathbf{u}), \Phi)$ in the Eq. (2.2) represents internal energy density function [60] which is defined as

$$\Psi_E(\boldsymbol{\varepsilon}(\mathbf{u}), \Phi) = g(\Phi)\Psi_0(\boldsymbol{\varepsilon}) \quad (2.3)$$

where $g(\Phi)$ is the degradation function. The choice of degradation function $g(\Phi)$ plays an important role in the elastic stiffness of the material. While there is a liberty in choosing the degradation function, it must adhere to the condition mentioned in Table. 1. In the literature, numerous researchers [174, 175, 176, 177] proposed degradation function $g(\Phi)$ depending on the application. In the present work, the quadratic degradation function $g(\Phi) = (1 - \Phi)^2$ proposed by [174] is adopted since it is best suited for understanding fracture in brittle materials.

Condition	Meaning
$g(0) = 1$	Intact material
$g(1) = 0$	Fully fracture material
$g'(\Phi) < 0$	$g(\Phi)$ monotonically decreasing function
$g'(1) = 0$	Ensure zero crack driving force for fully fractured material $\Phi = 1$

Table 1: Degradation function $g(\Phi)$ to be satisfied without violating the damage mechanics process.

The Eq. (2.3) results in unrealistic crack propagation behavior due to the multiplication of $g(\Phi)$ to the strain energy density function since crack propagates only due to tension behavior and doesn't affect due to compression. Several researchers [178, 179, 60] have proposed additive decomposition of strain energy density into positive strain energy Ψ_0^+ and negative strain energy Ψ_0^- part with the contribution of $g(\Phi)$ in Ψ_0^+ . The material degradation is controlled by the evolution of the phase-field function $g(\Phi) = (1 - \Phi)^2 + \kappa_p$ also called as stress degradation function with a parameter κ_p of the order of 10^{-6} to avoid ill-conditioning of the stiffness matrix when $\Phi \rightarrow 1$. This thesis adopts the strain energy split decomposition method proposed in [60] for analysis. Therefore the internal elastic energy of the function Π_E in Eq. (2.2) reads :

$$\Pi_E = \int_{\Omega} \Psi_E(\boldsymbol{\varepsilon}(\mathbf{u}), \Phi) d\Omega = \int_{\Omega} [g(\Phi)\Psi_0^+(\boldsymbol{\varepsilon}) + \Psi_0^-(\boldsymbol{\varepsilon})] d\Omega \quad (2.4)$$

To enforce the irreversibility of the phase-field damage ($\dot{\Phi} > 0$), a history variable \mathcal{H} [60] is introduced, which takes the maximum strain energy value during the damage evolution process:

$$\mathcal{H} = \begin{cases} \Psi_0^+(\boldsymbol{\varepsilon}) & \text{if } \Psi_0^+(\boldsymbol{\varepsilon}) > \mathcal{H}_n \\ \mathcal{H}_n & \text{otherwise} \end{cases} \quad (2.5)$$

where \mathcal{H}_n is the value of Ψ_0^+ at the previous pseudo-time step of a quasi-static simulation with pseudo-time increasing applied displacements/loads. Note that the function \mathcal{H} satisfies the Karush-Kuhn-Tucker conditions:

$$\Psi_0^+ - \mathcal{H} \leq 0, \dot{\mathcal{H}} \geq 0, \dot{\mathcal{H}} (\Psi_0^+ - \mathcal{H}) = 0 \quad (2.6)$$

The second term in Eq. (2.2) can be expressed in the regularised form [131] by approximating the sharp crack Γ into a diffusive region with a phase-field damage variable Φ as shown in Fig. 1. The value of Φ ranges between 0 and 1, with 0 representing an intact material and 1 corresponding to a fully cracked material. The regularised expression reads

$$\Pi_S(\Phi) := \int_{\Gamma} G_c \, d\Gamma \approx \int_{\Omega} G_c \gamma(\Phi, \nabla\Phi) \, d\Omega \quad (2.7)$$

in which G_c is the fracture energy and $\gamma(\Phi, \nabla\Phi)$ represents the crack surface density function that can be expressed in general form [180] as

$$\gamma(\Phi, \nabla\Phi) = \frac{1}{C_0} \left[\frac{\alpha(\Phi)}{l_c} + l_c \nabla\Phi \cdot \nabla\Phi \right] \quad (2.8)$$

where l_c is the regularized internal length scale parameter that governs the width of the diffusive crack. When $l_c \rightarrow 0$, the regularized crack surface Γ -converges to the sharp crack [181], satisfying the Griffith's criterion [132].

In the literature, the commonly used Ambrosio–Tortorelli AT-1 and AT-2 models are frequently employed for phase-field fracture (PFF) analysis. In this work, we specifically utilize the AT-2 model [182]. Therefore the crack geometric function $\alpha(\Phi)$ and the normalized factor C_0 in Eq. (2.8) are [174, 60]:

$$\alpha(\Phi) = \Phi^2, C_0 = 2 \quad (2.9)$$

Hence, the surface energy term Π_S in Eq. (2.7) for an isotropic material assumes the following form:

$$\Pi_S(\Phi) = \frac{G_c}{2} \int_{\Omega} \left[\frac{\Phi^2}{l_c} + l_c \nabla\Phi \cdot \nabla\Phi \right] \, d\Omega \quad (2.10)$$

To consider the material anisotropy in the PFF analysis, the second-order structural tensor ω is incorporated in the nonlocal part of isotropic crack surface density for an anisotropic case as shown in Eq. (2.11):

$$\gamma(\Phi, \nabla\Phi, \omega) = \frac{1}{2} \left[\frac{\alpha(\Phi)}{l_c} + l_c \nabla\Phi \cdot \omega \cdot \nabla\Phi \right] \quad (2.11)$$

The second-order tensor ω is invariant (orientation independent). The surface energy for crack propagation depends on the material orientation α , which characterizes the anisotropic failure of the material. Following Clayton and Knap [61], ω can be defined as

$$\omega = \mathbb{1} + \eta(\mathbb{1} - f \otimes f), \quad \mathbb{1} = \begin{bmatrix} 1 & 0 \\ 0 & 1 \end{bmatrix} \quad (2.12)$$

where $\mathbb{1}$ is a second-order identity tensor and f represents a vector normal to the material orientation plane α . $\eta \gg 1$ represents the degree of anisotropy contributing to the crack evolution in the surface energy term Π_S along the direction of material orientation plane α . The isotropic material behavior can be retrieved when the penalty parameter η is vanishing.

Therefore, the surface energy term Π_S in Eq. (2.7) for an anisotropic material assumes the following final form:

$$\Pi_S(\Phi) = \frac{G_c}{2} \int_{\Omega} \left[\frac{\Phi^2}{l_c} + l_c \nabla\Phi \cdot \omega \cdot \nabla\Phi \right] d\Omega \quad (2.13)$$

2.2 Finite element implementation of the phase-field approach

In this section, we discuss the finite element implementation of phase-field formulation for isotropic and anisotropic fractured materials, a typical behavior observed in polymers, ceramics, etc. First, we apply the FEM to the PFF model in the context of isotropic materials and then generalize it to an anisotropic fracture case. Finally, the phase-field formulation necessary for studying the resistance to topology-optimized fractured structures is being investigated.

2.2.1 Isotropic case

The elastic energy term Π_E in Eq. (2.4) and the isotropic surface energy term Π_S in Eq. (2.10) are introduced into Eq. (2.2). The total energy functional for the isotropic case Π_{iso} therefore, reads:

$$\begin{aligned} \Pi_{iso}(\mathbf{u}, \Phi) = & \int_{\Omega} (g(\Phi)\Psi_0^+(\varepsilon) + \Psi_0^-(\varepsilon))d\Omega \\ & + \int_{\Omega} \frac{G_c}{2} \int_{\Omega} \left[\frac{\Phi^2}{l_c} + l_c \nabla\Phi \cdot \nabla\Phi \right] d\Omega - \int_{\Omega} \mathbf{b}\mathbf{u} d\Omega - \int_{\partial\Omega^t} \bar{\mathbf{t}}\mathbf{u} d\partial\Omega^t \end{aligned} \quad (2.14)$$

The weak form of the displacement field \mathbf{u} and phase-field Φ are then obtained by applying the energy minimization principle to Eq. (2.14) with respect to the state variables (\mathbf{u}, Φ) :

$$\frac{\partial\Pi(\mathbf{u}, \Phi)}{\partial\mathbf{u}} = \int_{\Omega} \sigma \delta\varepsilon d\Omega - \int_{\Omega} \mathbf{b} \delta\mathbf{u} d\Omega - \int_{\partial\Omega^t} \bar{\mathbf{t}} \delta\mathbf{u} d\partial\Omega^t = 0 \quad (2.15a)$$

$$\frac{\partial\Pi(\mathbf{u}, \Phi)}{\partial\Phi} = \int_{\Omega} 2(1 - \Phi)\mathcal{H}\delta\Phi d\Omega + \int_{\Omega} \frac{G_c}{2} \left[\frac{1}{l_c} 2\Phi\delta\Phi - l_c(\nabla\Phi \cdot \nabla\delta\Phi) \right] d\Omega = 0 \quad (2.15b)$$

The strong form associated with the weak form in Eq. (2.15) is:

$$\nabla \cdot \sigma + \mathbf{b} = 0 \text{ in } \Omega, \quad \sigma \cdot \mathbf{n} = \bar{\mathbf{t}} \text{ on } \partial\Omega^t, \quad u = \bar{u} \text{ on } \partial\Omega^u \quad (2.16)$$

$$-G_c l_c \nabla^2 \Phi + \left[\frac{G_c}{l_c} + 2\Psi(\varepsilon) \right] \Phi = 2\Psi(\varepsilon) \text{ in } \Omega, \quad \nabla\Phi \cdot \mathbf{n} = 0 \text{ on } \partial\Omega \quad (2.17)$$

To solve the above weak form, finite element discretization is introduced by projecting Eq. (2.15) onto a suitable functional space. Usually, a functional space composed of linear or quadratic polynomials is a natural choice. However, other spaces like those defined by NURBS could be exploited [183], and it is a current research direction. Moreover, in the case of polynomials, $h-$, $p-$, and $hp-$ refining schemes are currently being investigated to improve the efficiency of the computational method.

The above projection implies a discretization of the continuum Ω , whose spatial coordinates are interpolated using the same shape functions used for the field variables (and of the corresponding test functions) in the isoparametric FE schemes. Therefore, this leads to the approximate discretized geometry and field variables, where the index h recalls the spatial discretization: $\mathbf{x} \sim \mathbf{x}_h$, $\mathbf{u} \sim \mathbf{u}_h$, $\Phi \sim \Phi_h$.

Therefore in the FEM framework, at an elemental level, the displacement field \mathbf{u} and phase-field Φ are discretized by shape functions \mathbf{N}_u and \mathbf{N}_Φ expressed as follows. The corresponding derivatives of displacement and phase-field values are also mentioned below.

$$\mathbf{u} = \mathbf{N}_u \mathbf{u}_e, \quad \Phi = \mathbf{N}_\Phi \Phi_e, \quad \boldsymbol{\varepsilon} = \mathbf{B}_u \mathbf{u}_e, \quad \nabla \Phi = \mathbf{B}_\Phi \Phi_e \quad (2.18)$$

Similarly, the virtual variation terms of primary variables and their derivatives are defined as

$$\delta \mathbf{u} = \mathbf{N}_u \delta \mathbf{u}_e, \quad \delta \Phi = \mathbf{N}_\Phi \delta \Phi_e, \quad \delta \boldsymbol{\varepsilon} = \mathbf{B}_u \delta \mathbf{u}_e, \quad \nabla \delta \Phi = \mathbf{B}_\Phi \delta \Phi_e \quad (2.19)$$

where \mathbf{B}_u , \mathbf{B}_Φ are the derivatives of the shape functions \mathbf{N}_u , \mathbf{N}_Φ respectively.

The arbitrariness of test functions leads to the following residual mechanical field and phase-field terms expressed as:

$$\mathbf{R}_u = \int_{\Omega^e} \mathbf{B}_u^T \boldsymbol{\sigma} \, d\Omega - \int_{\Omega^e} \mathbf{N}_u^T \mathbf{b} \, d\Omega - \int_{\partial\Omega^e} \mathbf{N}_u^T \bar{\mathbf{t}} \, d\partial\Omega \quad (2.20)$$

$$\mathbf{R}_\Phi = \int_{\Omega^e} G_c l_c \mathbf{B}_\Phi^T \nabla \Phi \, d\Omega + \int_{\Omega^e} \left[\frac{G_c}{l_c} + 2\mathcal{H} \right] \mathbf{N}_\Phi^T \Phi \, d\Omega - \int_{\Omega^e} 2\mathbf{N}_\Phi \mathcal{H} \, d\Omega \quad (2.21)$$

The solution to the above nonlinear problem can be achieved via the application of the full Newton-Raphson solution scheme, which requires the linearization of the residual vectors with respect to its field variable:

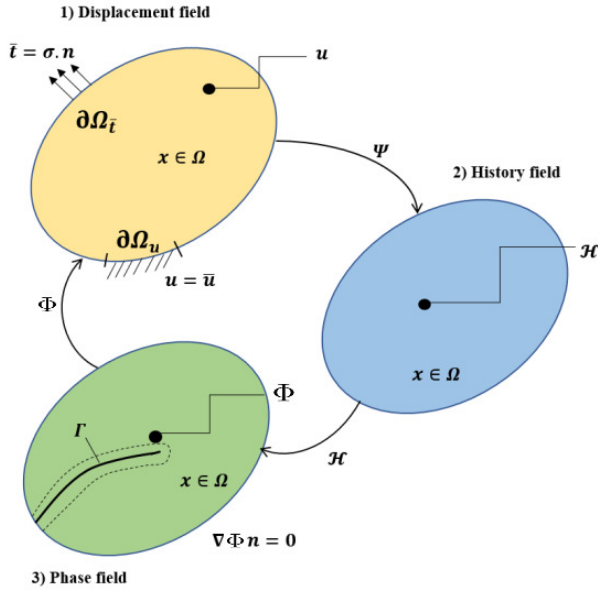
$$\mathbf{K}_u = \frac{\partial \mathbf{R}_u}{\partial \mathbf{u}} = \int_{\Omega^e} \mathbf{B}_u^T \mathbb{C} \mathbf{B}_u \, d\Omega \quad (2.22)$$

$$\mathbf{K}_\Phi = \frac{\partial \mathbf{R}_\Phi}{\partial \Phi} = \int_{\Omega^e} G_c l_c \mathbf{B}_\Phi^T \mathbf{B}_\Phi \, d\Omega + \int_{\Omega^e} \left[\frac{G_c}{l_c} + \mathcal{H} \right] \mathbf{N}_\Phi^T \mathbf{N}_\Phi \, d\Omega \quad (2.23)$$

The computation of the fourth order stiffness tensor \mathbb{C} and the second order stress tensor σ are detailed in Section 2.2.2.

Therefore, the Newton-Raphson incremental-iterative scheme following a staggered solution algorithmic procedure 1, as proposed in [23] (see also Fig. 2) is implemented by parametrization of the above equation with a pseudo-time 't'

$$\begin{Bmatrix} \mathbf{u} \\ \Phi \end{Bmatrix}_{t+\Delta t} = \begin{Bmatrix} \mathbf{u} \\ \Phi \end{Bmatrix}_t + \begin{bmatrix} \mathbf{K}_u & \mathbf{0} \\ \mathbf{0} & \mathbf{K}_\Phi \end{bmatrix}_t^{-1} \begin{Bmatrix} \mathbf{R}_u \\ \mathbf{R}_\Phi \end{Bmatrix}_t \quad (2.24)$$



(a)

Figure 2: Illustration of the staggered scheme to solve the coupled nonlinear phase-field problem.

2.2.2 Strain energy split decomposition method

To consider for the crack to propagate only in tension mode, which means no crack propagation in compression loading, the strain tensor is decom-

posed into tension and compression parts

$$\varepsilon = \varepsilon_+ + \varepsilon_- \quad (2.25)$$

with $\varepsilon = \sum_{i=1}^{\delta} \varepsilon^i \mathbf{n}^i \otimes \mathbf{n}^i$, where $\{\varepsilon^i\}_i = 1 \dots \delta$ and $\{\mathbf{n}^i\}_i = 1 \dots \delta$ are the principal strains and its corresponding strain directions, respectively. The strain splits are represented as

$$\varepsilon_+ = \sum_{i=1}^{\delta} \langle \varepsilon^i \rangle_+ \mathbf{n}^i \otimes \mathbf{n}^i \quad \varepsilon_- = \sum_{i=1}^{\delta} \langle \varepsilon^i \rangle_- \mathbf{n}^i \otimes \mathbf{n}^i \quad (2.26)$$

where $\langle \cdot \rangle$ is Macaulay bracket represented as $\langle x \rangle_+ := (x + |x|)/2$ and $\langle x \rangle_- := (x - |x|)/2$. The strain energy in an undamaged solid is expressed as

$$\Psi_0(\varepsilon) = \lambda \text{tr}^2[\varepsilon]/2 + \mu \text{tr} [\varepsilon^2] \quad (2.27)$$

with λ and μ are lame's constant. The strain energy function is split into positive and negative parts with the inclusion of lames constants in the equation shown below

$$\begin{aligned} \Psi(\varepsilon) &= \Psi_0^+(\varepsilon) + \Psi_0^-(\varepsilon) \\ \Psi_0^+(\varepsilon) &= \lambda \langle \text{tr}[\varepsilon] \rangle_+^2 / 2 + \mu \text{tr} [\varepsilon_+^2] \\ \Psi_0^-(\varepsilon) &= \lambda \langle \text{tr}[\varepsilon] \rangle_-^2 / 2 + \mu \text{tr} [\varepsilon_-^2] \end{aligned} \quad (2.28)$$

Now, the stress tensor σ can be found from the first derivation of the strain energy function

$$\sigma := \partial_{\varepsilon} \Psi(\varepsilon, \Phi) = [(1 - \Phi)^2 + k] [\lambda \langle \text{tr}[\varepsilon] \rangle_+ \mathbb{1} + 2\mu \varepsilon_+] + [\lambda \langle \text{tr}[\varepsilon] \rangle_- \mathbb{1} + 2\mu \varepsilon_-] \quad (2.29)$$

where $\mathbb{1}$ represents second-order identity tensor. The fourth-order stiffness tensor \mathbb{C} is expressed as

$$\begin{aligned} \mathbb{C} &= ((1 - \Phi)^2 + k) \partial_{\varepsilon} [\sigma_+(\varepsilon)] + \partial_{\varepsilon} [\sigma_-(\varepsilon)] \\ &= ((1 - \Phi)^2 + k) \partial_{\varepsilon_+} [\sigma_+(\varepsilon_+)] \mathbb{P}^+ + \partial_{\varepsilon_-} [\sigma_-(\varepsilon_-)] \mathbb{P}^- \\ &= ((1 - \Phi)^2 + k) 2\mu \mathbb{P}^+ + 2\mu \mathbb{P}^- \end{aligned} \quad (2.30)$$

$$\begin{aligned}
\mathbb{P}^\pm &= \partial_\varepsilon [\varepsilon^\pm(\varepsilon)] \\
&= \sum_{a=1}^3 H(\pm\varepsilon_a) \mathbb{Q}_a + \frac{1}{2} \sum_a^3 \sum_{b \neq a}^3 \theta_{ab} (\mathbb{G}_{ab} + \mathbb{G}_{ba}) \theta_{ab} \\
&= \begin{cases} \frac{\langle \varepsilon_a \rangle_\pm - \langle \varepsilon_b \rangle_\pm}{\varepsilon_a - \varepsilon_b} & \text{if } \varepsilon_a \neq \varepsilon_b \\ H(\pm\varepsilon_a) & \text{if } \varepsilon_a = \varepsilon_b \end{cases}
\end{aligned} \tag{2.31}$$

Algorithm 1 Staggered solution scheme

- 1: Data initialization \mathbf{u}_0, Φ_0 and \mathcal{H}_0 at time t_0 are known
 - 2: **for** all time incremental steps: starts at $i = 1$ **do**
 - 3: $t_i \leftarrow t_o + \Delta t$ (Δt :small time increment)
 - 4: Iteration n=0
 - 5: **while** $\max \left\{ \frac{\|\mathbf{R}_u^n\|}{\|\mathbf{R}_u^0\|}, \frac{\|\mathbf{R}_\Phi^n\|}{\|\mathbf{R}_\Phi^0\|} \right\} \leq 10^{-3}$ **do**
 - 6: $n \leftarrow n + 1$
 - 7: Step 1: Determine displacement field by prescribing boundary condition $\mathbf{u}, \mathbf{p}, t$ at current time step
 - 8: Compute maximum strain energy \mathcal{H}_{\max} at each gauss points
 - 9: Compute residual \mathbf{R}_u^0
 - 10: $\mathbf{K}_u du = \mathbf{R}_u^0$
 - 11: $\mathbf{u}_i^n = \mathbf{u}_0 + du$
 - 12: Step 2: Determine phase-field at current time step iteration by fixing displacement field at current iteration n
 - 13: Compute residual \mathbf{R}_Φ^0
 - 14: $\mathbf{K}_\Phi d\Phi = \mathbf{R}_\Phi^0$
 - 15: $\Phi_i^n = \Phi_0 + d\Phi$
 - 16: $\mathbf{u}_0 \leftarrow \mathbf{u}_i^n, \Phi_0 \leftarrow \Phi_i^n$
 - 17: n \leftarrow n+1
 - 18: { /* for while condition $\mathbf{R}_u^0, \mathbf{R}_\Phi^0$ taken from iteration n = 1 for the current time step */ }
 - 19: { /* maximum strain energy \mathcal{H}_{\max} at each gauss point from iteration n = 1 is fixed for the current time step */ }
 - 20: **end while**
 - 21: $i \leftarrow i+1, t_o \leftarrow t_i$
 - 22: **end for**
-

2.2.3 Anisotropic case

The elastic energy term Π_E in Eq. (2.4) and the anisotropic surface energy term Π_S in Eq. (2.13) are introduced into Eq. (2.2). The weak form of the displacement field \mathbf{u} and phase-field Φ are then obtained by applying the energy minimization principle to Eq. (2.2) with respect to the state variables (\mathbf{u}, Φ) :

$$\begin{aligned} \frac{\partial \Pi(\mathbf{u}, \Phi)}{\partial \mathbf{u}} &= \int_{\Omega} \sigma \delta \varepsilon d\Omega - \int_{\Omega} \mathbf{b} \delta \mathbf{u} d\Omega - \int_{\partial \Omega^t} \bar{\mathbf{t}} \delta \mathbf{u} d\partial \Omega^t = 0 \\ \frac{\partial \Pi(\mathbf{u}, \Phi)}{\partial \Phi} &= \int_{\Omega} 2(1 - \Phi) \mathcal{H} \delta \Phi d\Omega \\ &+ \int_{\Omega} \frac{G_c}{2} \left[\frac{1}{l_c} 2\Phi \delta \Phi - l_c \nabla \cdot (\boldsymbol{\omega} \cdot \nabla \delta \Phi) \right] d\Omega = 0 \end{aligned} \quad (2.32)$$

The numerical implementation of the PFF formulation into the finite element method (FEM) is performed as in [23]. The weak forms in Eq. (2.32) are solved using a staggered scheme to obtain the displacement field \mathbf{u} and the phase-field Φ solutions; see [23] for more details. Both equations are connected with the history field variable \mathcal{H} as mentioned in Eq. (2.5) to exchange the state variables during the iterative scheme, as shown in Fig. 2.

2.3 Phase-field formulation for topology optimization problems

The only difference while deriving the phase-field finite element formulation when integrating with topology optimization to investigate structure optimization for fracture resistance problems is the history field variable \mathcal{H} . An irreversibility condition upon Φ has to be introduced in Eq. (2.14) to avoid material healing during damage evolution. Moreover, Eq. (2.14) is monotonically increasing and might accumulate stress degradation even at low strain values. So, to avoid the situation, we employ the energy damage evolution criteria from [184] to introduce the history variable \mathcal{H} in Eq. (2.14) and by applying the energy minimization principle, which yields.

$$\begin{aligned} \delta\Pi = & \int_{\Omega} \sigma \delta \varepsilon d\Omega - \int_{\Omega} 2(1 - \Phi) \mathcal{H} \delta \Phi(\varepsilon) d\Omega \\ & + \int_{\Omega} 2\Psi_c (l_c^2 \nabla \Phi \nabla \delta \Phi + \Phi \delta \Phi) d\Omega - \int_{\Omega} b \delta u d\Omega - \int_{\partial\Omega^t} \bar{t} \delta u d\partial\Omega^t \end{aligned} \quad (2.33)$$

where in which history field variable given as

$$\mathcal{H} = \mathcal{H}(\varepsilon) = \max_{s \in [0, t]} [\langle \Psi_0^+(\varepsilon, s) - \Psi_c \rangle_+] \quad (2.34)$$

where Ψ_c is the specific fracture energy density given by

$$\Psi_c = \frac{1}{2E} \sigma_c^2 \quad (2.35)$$

in which σ_c is the critical fracture stress and E is the Young's modulus.

The strong form associated with the weak form in Eq. (2.33) is:

$$\nabla \cdot \sigma + \mathbf{b} = 0 \text{ in } \Omega, \quad \sigma \cdot \mathbf{n} = \bar{t} \text{ on } \partial\Omega^t, \quad u = \bar{u} \text{ on } \partial\Omega^u \quad (2.36)$$

$$-\Psi_c l_c^2 \nabla^2 \Phi + [\Psi_c + \mathcal{H}(\varepsilon)] \Phi = \mathcal{H}(\varepsilon) \text{ in } \Omega, \quad \nabla \Phi \cdot \mathbf{n} = 0 \text{ on } \partial\Omega \quad (2.37)$$

The arbitrariness of test functions at the element level leads to the following residual mechanical field \mathbf{u} and phase-field Φ terms expressed as:

$$\mathbf{R}_{\mathbf{u}} = \int_{\Omega^e} \mathbf{B}_{\mathbf{u}}^T \boldsymbol{\sigma} d\Omega - \int_{\Omega^e} \mathbf{N}_{\mathbf{u}}^T \mathbf{b} d\Omega - \int_{\partial\Omega^e} \mathbf{N}_{\mathbf{u}}^T \bar{\mathbf{t}} d\partial\Omega \quad (2.38)$$

$$\mathbf{R}_{\Phi} = \int_{\Omega^e} [\mathcal{H} + \Psi_c] \mathbf{N}_{\Phi}^T \Phi d\Omega + \Psi_c l_c^2 \mathbf{B}_{\Phi}^T \nabla \Phi d\Omega - \int_{\Omega^e} \mathbf{N}_{\Phi} \mathcal{H} d\Omega = 0 \quad (2.39)$$

The above nonlinear Eq. (2.38) can be solved without performing the Newton linearization by using the shifted strain tensor split algorithm proposed in [185]. Finally, the equation can be solved in a linear system of equations:

$$\mathbf{K}_u \mathbf{u} = \mathbf{F}_u \quad (2.40)$$

$$\mathbf{K}_u = \int_{\Omega^e} \mathbf{B}_{\mathbf{u}}^T \mathbb{C} \mathbf{B}_{\mathbf{u}} d\Omega \quad (2.41)$$

$$\mathbf{F}_u = \int_{\Omega^e} \mathbf{N}_u^T \mathbf{b} \, d\Omega - \int_{\partial\Omega^e} \mathbf{N}_u^T \bar{\mathbf{t}} \, d\partial\Omega \quad (2.42)$$

The details of computation of the fourth order stiffness tensor \mathbb{C} and the second order stress tensor $\boldsymbol{\sigma}$ are outlined in [185].

The phase-field solution can be solved in linear equation form which read as :

$$\mathbf{K}_\Phi \Phi = \mathbf{F}_\Phi \quad (2.43)$$

$$\mathbf{K}_\Phi = \int_{\Omega^e} \{ [\mathcal{H} + \Psi_c] \mathbf{N}_\Phi^T \mathbf{N}_\Phi + \Psi_c l_c^2 \mathbf{B}_\Phi^T \mathbf{B}_\Phi \} \, d\Omega \quad (2.44)$$

$$\mathbf{F}_\Phi = \int_{\Omega^e} \mathbf{N}_\Phi \mathcal{H} \, d\Omega \quad (2.45)$$

Therefore, the staggered solution scheme procedure [23] is implemented to find the displacement field \mathbf{u} and phase-field Φ solution to study the topology evolution of the structure subjected to fracture, which is discussed in Section 4.3.

2.4 Graded cohesive zone interface model

The computation mechanical framework of a cohesive interface between a deformable body and a substrate is presented here. The current framework assumes that the structure behavior obeys the small strain deformation theory. As shown in Fig. 3, we consider a continuum domain Ω in which a deformable substrate B1 and a second material B2 are connected by an adhesive, which mathematically provides continuity of tractions at the interface and a separation in the normal and in the tangential directions (computed with respect to the local reference system). By the principle of virtual work, the total energy in the weak form, including the contribution of cohesive interface tractions, reads:

$$\delta\Pi = \int_{\Omega} \boldsymbol{\sigma} \delta\boldsymbol{\varepsilon} \, d\Omega - \int_{\Omega} \mathbf{b} \delta\mathbf{u} \, d\Omega - \int_{\partial\Omega_t} \bar{\mathbf{t}} \delta\mathbf{u} \, d\partial\Omega_t - \int_{\partial\Omega_s} t_{\text{coh}} \delta\Delta\mathbf{u} \, d\partial\Omega_s \quad (2.46)$$

where $\boldsymbol{\sigma}$ represents the Cauchy stress tensor, $\delta\boldsymbol{\varepsilon}$ denotes the virtual variation of the strain field associated to the displacement field \mathbf{u} , \mathbf{b} and

$\bar{\mathbf{t}}$ represent the body forces and the imposed boundary tractions acting on Ω and $\partial\Omega_t$, respectively. The vector of cohesive tractions is t_{coh} , which contributes to the virtual work through the associated virtual variation of the relative displacement vector $\delta\Delta\mathbf{u}$ along the interface $d\partial\Omega_s$.

The finite element formulation associated to the cohesive interface model used in the present work is based on the 4-noded zero thickness interface finite element whose matrix expression and algorithmic implementation as a user element can be found in [94] and are represented here for understanding purpose. The same formulation has been implemented in a user element for a finite element research code [186] based on MATLAB R2022.

2.4.1 Finite element formulation

The present work deals with 2D problems, so we adopt standard four-noded quadrilateral finite elements (FE) for the structure's continuum domain Ω . For our convenience, the interface region is also discretized with four-noded FE, which is compatible. Therefore, each node in the interface element has two degrees of freedom in the global reference system, and the displacement vector \mathbf{u} of one interface FE is given as

$$\mathbf{u} = (u_1, v_1, u_2, v_2, u_3, v_3, u_4, v_4)^T \quad (2.47)$$

Where u_i, v_i represents horizontal and vertical displacements of node i respectively ($i \rightarrow 1 - 4$). The cohesive interface region is proposed to be zero-thickness finite elements. Therefore, the local coordinate system will be defined by drawing the central axis with normal vector \mathbf{n} and tangential vector \mathbf{t} between the top Γ^+ and bottom Γ^- sides of the cohesive interface. Generally, the central axis is rotated by an angle θ concerning the global x -axis. Two gauss points were chosen at zero-thickness FE along the central axis. The linear shape functions (\mathbf{N}) were incorporated at each gauss point in the interface element for interpolation purposes with values $N_1 = (1 - \xi)/2$ and $N_2 = (1 + \xi)/2$ where $\xi \in [-1, +1]$. The cohesive traction (t_{coh}), normal and tangential gap (g_n, g_t) values are calculated at each gauss point. g_n and g_t denote the normal and tangential gap along the zero-thickness finite element in the local reference system.

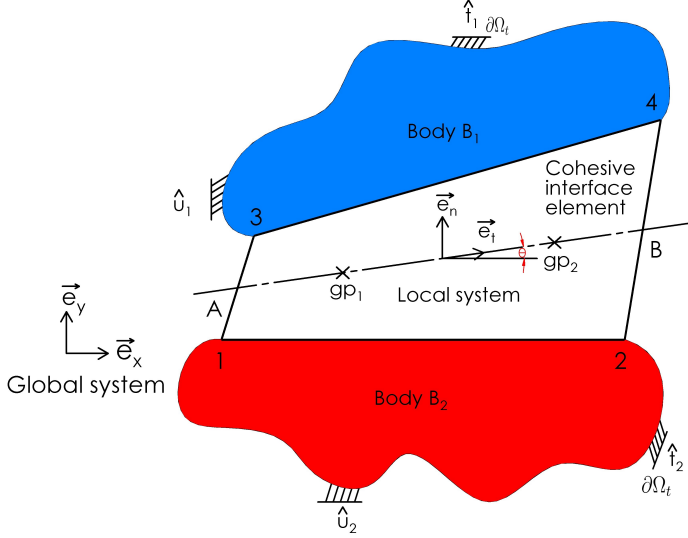


Figure 3: Schematic representation of a zero thickness interface element.

First, due to external loading, there might be a slight displacement change on the cohesive interface's top and bottom sides, creating a normal and tangential gap along the interface region. This phenomenon is captured along the zero-thickness interface FE at each gauss point with gap vector $\mathbf{g} = (g_t \ g_n)^T$. The following procedure is followed in context with each gauge point of interface FE. Gap vector \mathbf{g} can be determined as $\mathbf{g} = \mathbf{R} \mathbf{N} \Delta \mathbf{u}'$ which is computed by multiplying rotational matrix \mathbf{R} with the relative generalized displacement vector $\Delta \mathbf{u}'$ using the interpolation function \mathbf{N} . \mathbf{R} represent the rotational matrix in the local reference system, \mathbf{N} being shape function considering standard two-noded isoparametric FE. The \mathbf{R} , \mathbf{N} and $\Delta \mathbf{u}'$ expressions are given below

$$\mathbf{R} = \begin{bmatrix} \cos \theta & \sin \theta \\ -\sin \theta & \cos \theta \end{bmatrix} \quad (2.48)$$

$$\mathbf{N} = \begin{bmatrix} N_1 & 0 & N_2 & 0 \\ 0 & N_1 & 0 & N_2 \end{bmatrix} \quad (2.49)$$

$$\Delta \mathbf{u}' = (u_4 - u_1, v_4 - v_1, u_3 - u_3, v_3 - v_2)^T \quad (2.50)$$

Where $\Delta \mathbf{u}'$ is about local reference system and computed as $\Delta \mathbf{u}' = \mathbf{L} \mathbf{u}$. \mathbf{L} is an operator matrix that is related to the relative displacements considering the top and bottom sides (Γ^+ , Γ^-) of the interface.

$$\mathbf{L} = \begin{bmatrix} -1 & 0 & 0 & 0 & 0 & 0 & +1 & 0 \\ 0 & -1 & 0 & 0 & 0 & 0 & 0 & +1 \\ 0 & 0 & -1 & 0 & +1 & 0 & 0 & 0 \\ 0 & 0 & 0 & -1 & 0 & +1 & 0 & 0 \end{bmatrix} \quad (2.51)$$

The above procedure leads to finding gap vector $\mathbf{g} = \mathbf{R} \mathbf{N} \mathbf{L} \Delta \mathbf{u} = \mathbf{R} \mathbf{B} \Delta \mathbf{u}$ at each gauss point in relation to the nodal displacement vector of the global system. The contribution of the cohesive interface element to the weak form in Eq. (2.46) is given below :

$$\delta G_{int} = \int_{S_{int}} \delta \mathbf{g}^T t_{coh} dS \quad (2.52)$$

The interface delamination proceeds until the relative normal g_n displacement and the tangential g_t displacements greater than critical normal g_{n_c} and tangential g_{t_c} gap indicating stresses reached adhesion strength of the interface.

2.4.2 Constitute model for cohesive interfaces

Due to external loading applied on the structure, the cohesive interface region can delaminate and is governed by a Mixed Mode traction-separation relation proposed by Tvergaard [82]. The σ_n and τ_t cohesive tractions composing the vector t_{coh} are nonlinear functions of the normal and tangential gaps g_n and g_t :

$$\begin{aligned} \sigma_n &= \sigma_{\max} \frac{g_n}{g_{n_c}} f(\eta) \\ \tau_t &= \tau_{\max} \frac{g_t}{g_{t_c}} f(\eta) \end{aligned} \quad (2.53)$$

where g_n, g_t represents normal and tangential components of local gap vector and g_{n_c}, g_{t_c} are critical normal and tangential displacements for complete decohesion under pure Mode I or Mode II fracture, $f(\eta)$ is a function which establishes a measure of the combined Mixed Mode deformation at the interface. $\sigma_{\max}, \tau_{\max}$ are the maximum normal and tangential traction of the interface corresponding to when g_n, g_t reaches g_{n_c}, g_{t_c} values. For the Tvergaard CZM we have:

$$\eta = \sqrt{\left(\frac{g_n}{g_{n_c}}\right)^2 + \left(\frac{g_t}{g_{t_c}}\right)^2} \quad (2.54)$$

$$f(\eta) = \begin{cases} \frac{27}{4} (1 - 2\eta + \eta^2), & \text{for } 0 \leq \eta \leq 1 \\ 0, & \text{otherwise} \end{cases} \quad (2.55)$$

The linearization of cohesive traction obtains the tangent constitutive matrix for Tvergaard exponential law CZM with respect to the gap vector which reads below:

$$\mathbf{C}_T = \begin{bmatrix} \frac{\partial \tau}{\partial g_t} & \frac{\partial \tau}{\partial g_n} \\ \frac{\partial \sigma}{\partial g_t} & \frac{\partial \sigma}{\partial g_n} \end{bmatrix} = \begin{bmatrix} \tau_{\max} \frac{f}{g_{t_c}} + \tau_{\max} \frac{g_t}{g_{t_c}} \frac{\partial f}{\partial \eta} \frac{\partial \eta}{\partial g_t} & \tau_{\max} \frac{g_t}{g_{t_c}} \frac{\partial f}{\partial \eta} \frac{\partial \eta}{\partial g_n} \\ \sigma_{\max} \frac{g_n}{g_{n_c}} \frac{\partial f}{\partial \eta} \frac{\partial \eta}{\partial g_t} & \sigma_{\max} \frac{f}{g_{n_c}} + \sigma_{\max} \frac{g_n}{g_{n_c}} \frac{\partial f}{\partial \eta} \frac{\partial \eta}{\partial g_n} \end{bmatrix} \quad (2.56)$$

where $t_{\text{coh}} = (\tau_t \ \sigma_n)^T$ represents tangential and normal tractions. Therefore, the interface constitutive law will be linearized for its implementation in the Newton-Raphson iterative scheme.

$$t_{\text{coh}} = \mathbf{C}_T \mathbf{g} = \mathbf{C}_T \mathbf{R} \mathbf{B} \mathbf{u} \quad (2.57)$$

Where \mathbf{C}_T represents the tangent constitutive matrix of the interface element given by the traction-separation law of the CZM. The CZM relation is graphically shown in a qualitative manner in Fig. 4 in terms of t_{coh}

vs. g_n and g_t . Under pure Mode I conditions, the area below the t_{coh} vs. g_n curve for $g_t = 0$ leads to the Mode I fracture energy G_{IC} . Similarly, the area below the t_{coh} vs. g_t curve for $g_n = 0$ leads to the Mode II fracture energy G_{IIC} .

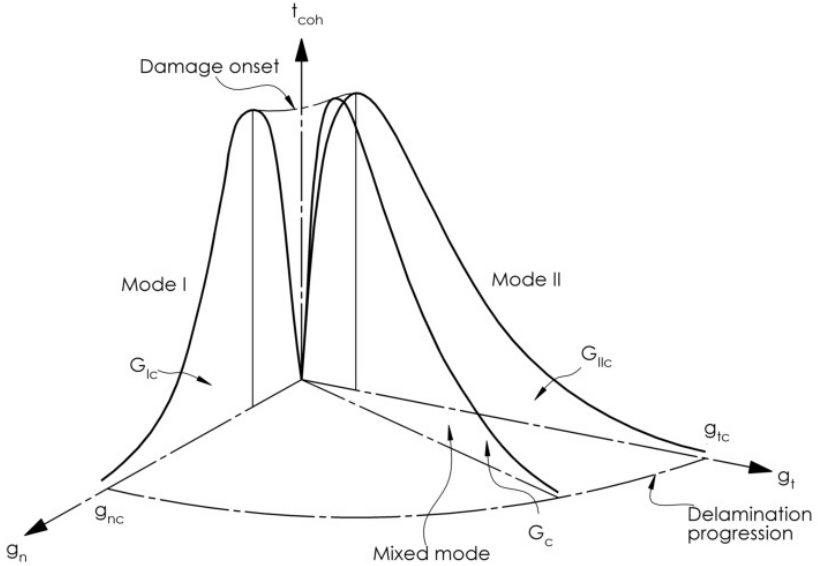


Figure 4: Tvergaard exponential law cohesive zone model

Here, we shall consider two functional forms for the CZM relation: (i) homogeneous properties throughout the interface (ii) linearly graded fracture toughness. In both cases, maximum tractions are the same, while the graded interface model introduces a linear dependency of the critical normal and tangential displacements upon the interface coordinate x defined in the global reference frame, see Fig. 5.

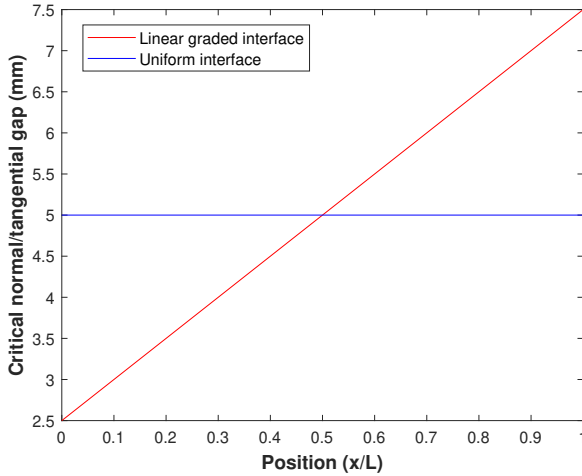


Figure 5: Linear graded interface model: critical cohesive normal and tangential gaps, g_{n_c} and g_{t_c} for complete decohesion vs. interface position x/L , where L denoted the maximum extension of the interface. The curve in blue shows the value of the parameters for an interface with uniform properties averaged over the interface length.

2.5 Optimum functional grading properties of cohesive interfaces

In this section, we analyze the failure of linearly graded interfaces and compare their performance with that of an interface with uniform averaged properties. Then, we show how to apply a data-driven machine learning technique to automatically find the properties of the linearly graded interface to maximize the functional performance of a structure subject to delamination.

2.5.1 Analysis of a linearly graded cohesive interface

The 2D numerical model of the peeling test that will be used as a benchmark for the analyses is shown in Fig. 6. The deformable layer with

a height of 0.05 mm is peeled off from a stiffer substrate, which is 1 mm deep. The lateral size of the whole numerical model is $L = 1$ mm. The progress of separation till failure of the interface is governed by the traction-separation (TS) law.

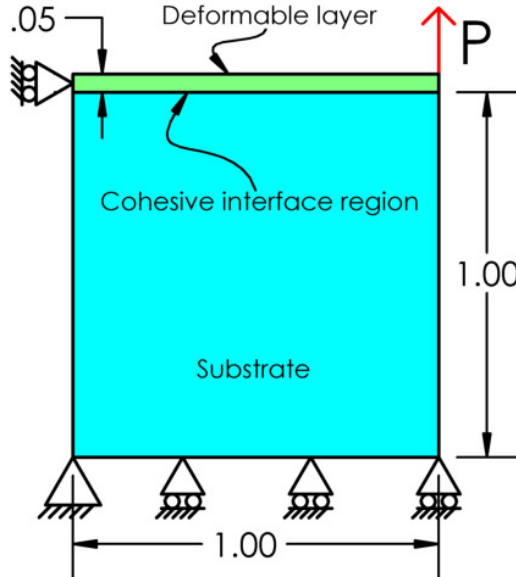


Figure 6: Model sketch of the peeling test.

The Youngs' modulus of the deformable layer is set equal to 2.8 GPa, and that of the substrate 73 GPa, which is a physical scenario for a thin deformable layer bonded onto an almost rigid substrate. For what concerns the boundary conditions, Fig. 6, the bottom left corner node is constrained in the horizontal and vertical direction while the remaining nodes at the bottom edge are constrained on the vertical direction. For the deformable layer, horizontal displacements at the nodes belonging to the edge on the left are constrained.

Contact constraints were incorporated into the CZM using the penalty method active in compression with a stiffness $k_p = 1000 \text{ N/mm}^2$ to avoid

the compenetration of materials along the interface. The linearly graded interface properties for the Tvergaard CZM are: $\sigma_{\max} = \tau_{\max} = 20$ MPa, $g_{n_c} = g_{t_c} \in (2.5 - 7.5)$ mm. Hence, the critical normal and tangential gaps vary linearly from 2.5 mm at $x = 0$ to 7.5 mm at $x = L$, as shown in Fig. 5. For this benchmark problem, the Mode I and Mode II TSL properties are the same.

FEM simulations are conducted under plane strain assumptions. The peeling test problem has been discretized with 4-noded isoparametric quadrilateral elements. The substrate has been discretized with 100×4 elements, since it is almost rigid. The interface region has been discretized with 100 elements along its length, while the deformable layer has been discretized with 100 elements along its length and 6 over its thickness, to capture its bending deformation.

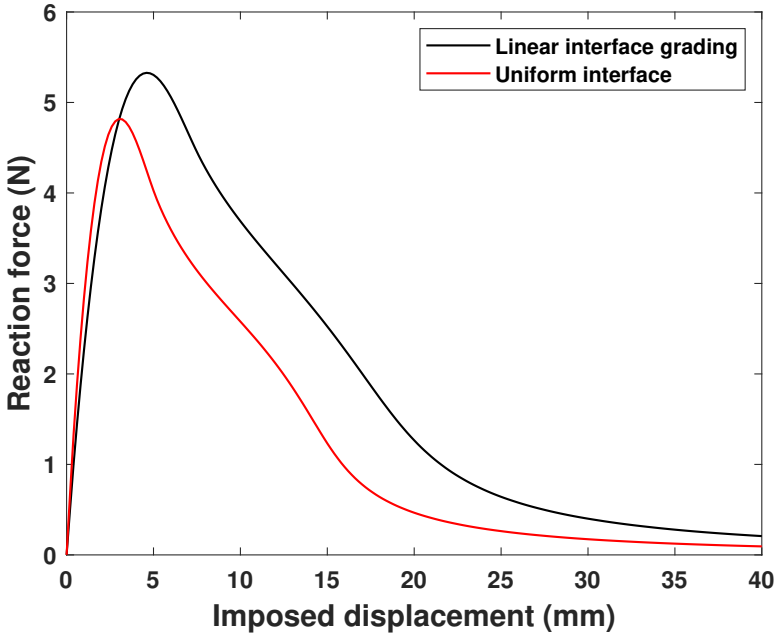
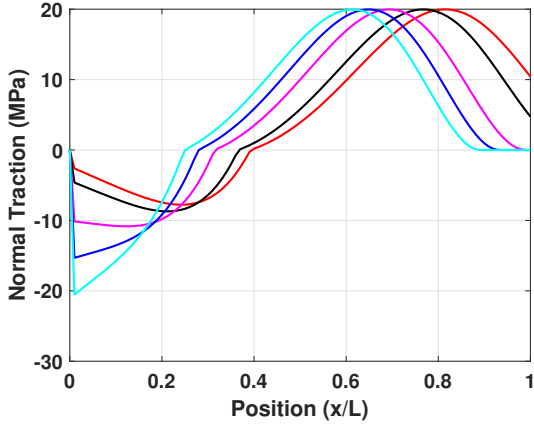


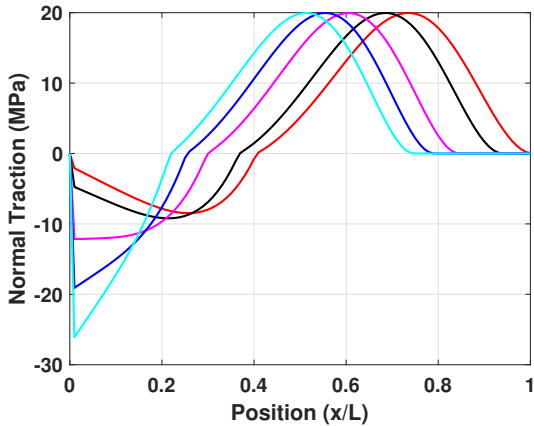
Figure 7: Reaction force P versus imposed displacement for a linearly graded interface in comparison to an interface with uniform properties.

The top right corner of the deformable layer is subject to a prescribed displacement as external loading. The corresponding force P is computed as a reaction force in the node. For the model test problem chosen, the mentioned loading leads to Mixed-Mode delamination. The evolution of the reaction force P for an interface with uniform properties and for a linearly graded one are shown versus the imposed displacement in Fig. 7, with a typical trend as reported in the literature [91, 187, 92]. The linearly graded interface, although in average has the same properties of the uniform one, has a spatial distribution of its fracture toughness which is highly beneficial, since it offers a stronger opposition to the onset of debonding through its higher value of G_C at $x = L$. As a consequence, the peak force for the onset of debonding is enhanced.

Looking into more details on what happens along the interface in the two scenarios, we notice that the interface with graded properties generates a non-uniform normal traction at the interface which is quite different as compared to the uniform case, see Fig. 8. Normal traction curves vs. x/L superimposed to those figures correspond to an increasing applied displacement (moving from the curve in red to the one in light blue). The graded interface allows delaying the onset for delamination as compared to the interface with uniform properties, see the red curve at $x/L = 1$ that, for the uniform one, is already approaching zero while for the graded interface has a residual value of about 10 MPa, i.e., it is still partially bonded.



(a) Linear graded cohesive interface



(b) Uniform cohesive interface

Figure 8: Comparison of normal tractions vs. position for a linearly graded interface and an interface with uniform interface properties for different far-field prescribed displacements increasing in the curves from red to light blue.

Chapter 3

Data-driven models for the identification of fracture mechanics parameters

Chapter 3 is partially based on the content of publication [1] and article in press [3].

Data-driven models, a subset of machine learning techniques, are increasingly utilized for parameter identification due to their robust optimization capabilities and adaptability to complex structural problems. In this chapter, we employed metaheuristic algorithms to simulate the process of natural evolution and large datasets to identify trends, employing machine learning and statistical analysis techniques to iteratively improve the solution. In parameter identification, metaheuristic algorithms explore a wide search space to determine the optimal set of parameters best fit a given trend. This process involves evaluating the fitness of each candidate solution against a predefined objective function, gradually converging towards the optimal parameters. The use of metaheuristic algorithms in parameter identification is particularly advantageous for nonlinear, multi-dimensional, and noisy problems, where traditional optimization methods may struggle. By leveraging the principles of natural selection, these algorithms offer a powerful and flexible approach to solving challenging parameter identification tasks across various engineering and biomedical fields. This chapter is

dedicated to discussion on different metaheuristics algorithms and their application to fracture models to identify the fracture mechanics parameters. These techniques come under the category of inverse problems, which are in very high demand in the additive manufacturing industry.

3.1 Theory on metaheuristic algorithms

Metaheuristic algorithms, such as genetic algorithms, particle swarm optimization, EJAYA algorithm e.t.c to name a few, have been effectively applied to fracture problems for the identification of fracture parameters. These algorithms excel in handling the complexity and nonlinearity inherent in fracture mechanics. By optimizing objective functions that quantify the difference between experimental data and model predictions, metaheuristics can efficiently navigate the vast parameter space to identify critical fracture parameters. Their robustness and flexibility make them invaluable tools in predicting fracture behavior, leading to more accurate assessments and improved material design in engineering applications.

The integration of machine learning algorithms and the formulation of the fracture models, as discussed in Chapter 2, is proposed to identify fracture mechanics parameters for a user-defined purpose. The issue of material parameters' identification to fulfill the desired system functionality and identify new material design solutions is a timely research topic. The optimization algorithms can tackle the inverse problems, and the metaheuristic algorithms [188], which are inspired by natural phenomena, are particularly efficient for this task. Although the metaheuristic algorithms [189, 190] employ various search strategies, they typically balance local exploitation with global exploration to solve the inverse problems. The objective of local exploitation is to find better solutions in the vicinity of the current search space, while global exploration is to find superior solutions across the complete space of admissible solutions. This combination resolves the problems encountered by gradient-based optimization algorithms that contain only local information [69].

The metaheuristic optimization approach called particle swarm opti-

mization (PSO) [102] is inspired by a flock of birds' behavior in search of food when they help each other reach their destination by exchanging information to find the optimal solution. To increase the performance of the PSO algorithm, a velocity of the constriction factor-based approach [70, 191] is implemented. Alternatively, genetic algorithms (GA) [192] can be exploited for inverse analyses, mimicking the process of population evolution by using several genetic processes, including crossover, mutation, and selection, to produce a new generation within the present population and progressively move it closer to an optimal solution. The ABC algorithm [193], for instance, is based on the approach used by a swarm of honey bees to find food sources. Two distinct beehive groups exchange information to discover these sources with success. First, there are the employee bees working and taking advantage of a food supply. Secondly, unemployed bees (scout bees) are constantly searching for a food supply. The implementation details of hybrid algorithms PSO-GA [71] and ABC-PSO [72, 73] take advantage of their respective individual algorithms and solve the inverse problems. The cuckoo's brood parasitic behavior is the basis for the Cuckoo Search (CS) algorithm [74]. Lévy flights are used by CS to search the solution space and create step size efficiently. Switch probability is used for the local search when a specific percentage of solutions are eliminated.

The teaching-learning-based optimization algorithm (TLBO), on the other hand, is an algorithm that draws inspiration from the teaching-learning process [194, 195] and is based on how a teacher's influence affects the work that students do in a class. The program simulates how a teacher and students would interact in a classroom. The population-based TLBO approach algorithm implementation details can be found in [194]. Another approach that can be used to solve the inverse problem is the Enhanced JAYA (EJAYA) algorithm [76], whose goal is to find a search mechanism that fully utilizes population data using a combination of local exploitation and global exploration tactics. A global exploration approach and a local exploitation strategy are part of the planned search mechanism, which was missing in the JAYA algorithm [105]. A detailed procedure description is found in [76].

All the above algorithms do not rely on the gradient of the objective function, while they require the objective function to be evaluated in the hyper-parameters design space. The converged solution has to be identified by minimizing the objective function Υ . For the mechanical fracture problems, the cost function to be minimized can be set as the difference between the predicted and the target reaction force-displacement curves.

Initially, we investigate the issue of model parameters' identification for the fracture problems using the phase-field for fracture, cohesive zone models as discussed in Chapter 2 and relevant for technical applications, as outlined in the Chapter 1 introduction part. Then, we compare the different machine learning algorithms as mentioned above to identify the best optimization method for fracture problems. First, we propose and assess the performance of a metaheuristic optimization technique called Particle Swarm Optimization (PSO), which has proven to be very effective in identifying model parameters for nonlinear fracture mechanics problems involving plasticity and cohesive fracture [28].

3.2 Fracture parameters identification using PSO algorithm

Particle Swarm Optimization (PSO) [102] is an algorithm that allows the scattering of a certain population of particles in a pre-defined parametric design space and optimizes the particles by achieving a minimum target cost function (Υ) to match the user desired mechanical response. In the present problem, Young's modulus (E), fracture toughness (G_c), and the phase-field internal length scale parameter (l_c) are the parameters defining each swarm particle position. Considering a force-displacement mechanical response (from experiments or desired), the target cost function (Υ) for every swarm particle is defined as

$$\Upsilon(\chi) = \sqrt{\sum_{d=1}^N \left[\frac{\Delta F_d(\chi)}{\hat{F}_d(\chi)} \right]^2} \quad (3.1)$$

where $\Delta F_d(\chi) = F_d - \hat{F}_d(\chi)$, where F_d denotes the history of simulated forces for the range of imposed pseudo-time steps d ($d = 1, \dots, N$) for a test under displacement control till ' N ' number of imposed displacements and for a given set of trial model parameters. Analogously, $\hat{F}_d(\chi)$ represents the target values of forces for the same ' N ' imposed displacements. The PSO algorithm is detailed in Algorithm 2 in relation to the methodology outlined in the Section 3.2.2. First, we identify the phase-field fracture parameters using PSO and next, followed by the identification of cohesive zone model parameters.

3.2.1 Identification of phase-field fracture parameters

The issue of finding phase-field fracture parameters to accurately predict the experimental force-displacement curve with the numerical PFF model is still a challenging problem. As a benchmark test, to show the applicability of PSO to parameters identification of phase-field fracture models, we consider here a Mode I single edge notch test (see Fig. 9) setting the following properties in input for the simulation ($E = 210$ GPa, $G_c = 2.7$ kN/mm, $l_c = 0.1$ mm). The finite element discretization consists of 1949 four-noded bilinear quadrilateral finite elements with a minimum mesh size of 0.05 mm along the potential crack path. The force-displacement curve predicted by phase-field simulation is taken as the target function \hat{F}_d to be subsequently matched by the PSO algorithm applied to identify the material parameters that are considered to be unknown.

In this regard, we attempt the simultaneous identification of all three material parameters. In the 3D parameter space, we consider $N_p = 30$ particles as population size, a maximum of 150 iterations, and the following PSO parameters: inertia weight $\mathbf{W}_i = 0.9$, damping weight $w_{\text{damp}} = 0.99$, cognitive coefficient $\mathbf{C}_c = 0.2$ and social coefficient $\mathbf{S}_c = 0.1$. The design-constrained particle space is defined as follows:

$$\mathcal{Z} = \{180 < E < 230 \text{ GPa}; 1.2 < G_c < 3.8 \text{ kN/mm}; 0.02 < l_c < 0.2 \text{ mm}\} \quad (3.2)$$

which includes the values of the three parameters to be identified.

The evolution of swarm particles' position within the design space for a selection of PSO iterations is shown in Fig. 11. The identified values of the model parameters were $E = 209.967$ GPa, $G_c = 2.699$ kN/mm, $l_c = 0.099$ mm, which are almost coincident with the parameters used to numerically generate the target response.

The cost function vs. number of iterations is shown in Fig. 10, with an error in the force-displacement curve at the 54-th iteration lower than 1×10^{-4} .

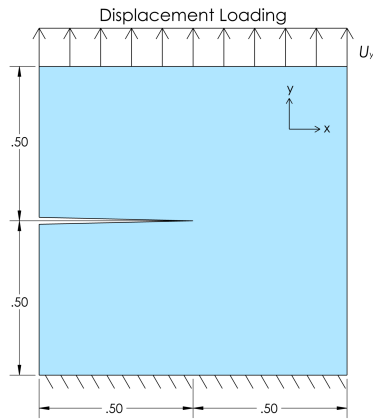


Figure 9: Benchmark problem: geometry, loading and boundary conditions.

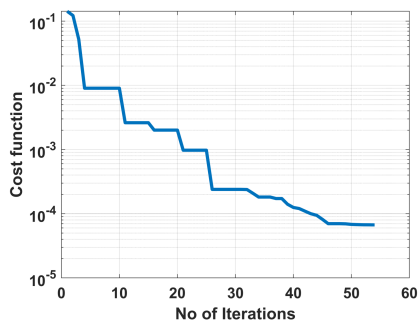
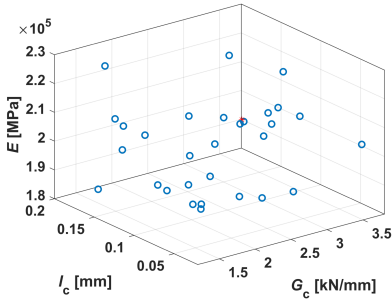


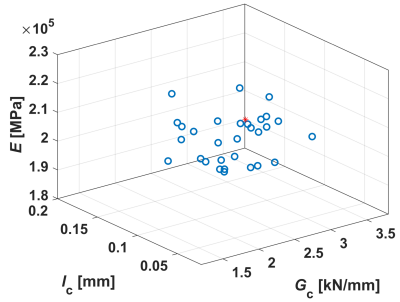
Figure 10: Cost function vs. No. of PSO iterations for the benchmark test.

Algorithm 2 Particle swarm optimization

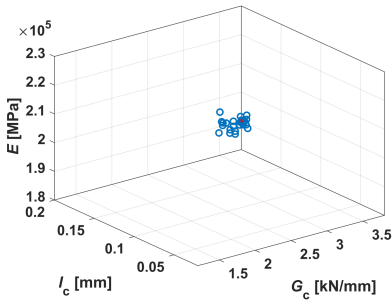
- 1: **Input data** : number of swarm particles N_p , maximum number of iterations It_{\max} , PSO algorithm parameters $\mathbf{W}_i, \mathbf{C}_c, \mathbf{S}_c, W_{\text{damp}}$
 - 2: **Output data** : optimized particle solutions \mathbf{P}_g for minimum cost function Υ
 - 3: ————**Initialization**———
 - 4: **for all** $i = 1 : N_p$ **do**
 - 5: Generate a population of swarm particles with random particle position χ_i^0 in three dimensional ($\wp = 3$) parametric space (E, G_c, l_c) variables under constrained solution search space for example as defined in Eq. (3.2)
 - 6: Evaluate cost function $\Upsilon(\chi_i^0)$
 - 7: Assign local best swarm particle position vector $\mathbf{P}_i^0 \leftarrow \chi_i^0$
 - 8: Assign zero swarm particle velocity vector \mathbf{V}_i^0
 - 9: **end for**
 - 10: Assign $\mathbf{P}_g^0 \leftarrow \underset{\chi_i^0}{\text{argmin}} \Upsilon(\chi_i^0)$
 - 11: Assign particle velocity range $V_r = [v_{\min} \ v_{\max}]$
 - 12: ————**Main loop of PSO algorithm**———
 - 13: **for** $k = 1 : It_{\max}$ **do**
 - 14: **for all** $i = 1 : N_p$ **do**
 - 15: Update particle velocity vector \mathbf{V}_i^k from Eq. (3.4)
 - 16: check \mathbf{V}_i^k in limits of V_r , if not reassign \mathbf{V}_i^k in range V_r
 - 17: Update particle position vector χ_i^k from Eq. (3.5)
 - 18: **if** $\chi_i^k \notin \wp$ **then**
 - 19: reassign randomly χ_i^k in \wp
 - 20: **end if**
 - 21: **if** $\Upsilon(\chi_i^k) < \Upsilon(\mathbf{P}_i^{k-1})$ **then**
 - 22: Update local best particle position \mathbf{P}_i^k from Eq. (3.6)
 - 23: **if** $\Upsilon(\mathbf{P}_i^k) < \Upsilon(\mathbf{P}_g^{k-1})$ **then**
 - 24: Update global best particle position \mathbf{P}_g^k from Eq. (3.7)
 - 25: **end if**
 - 26: **end if**
 - 27: **end for**
 - 28: $\mathbf{W}_i \leftarrow \mathbf{W}_i \times W_{\text{damp}}$
 - 29: **end for**
-



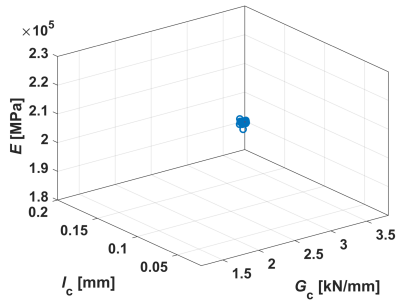
(a) Initial particles' position



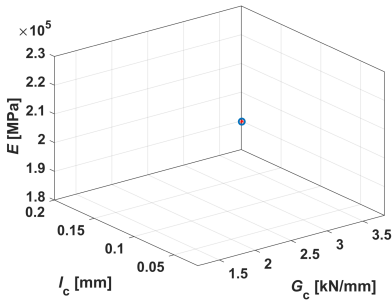
(b) Iteration No. 3



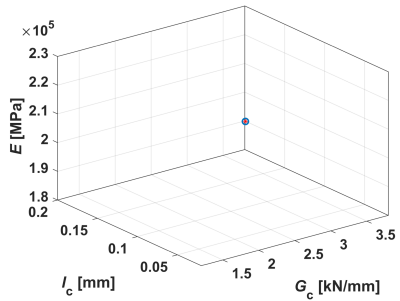
(c) Iteration No. 15



(d) Iteration No. 25



(e) Iteration No. 40



(f) Iteration No. 54

Figure 11: Scatter representation of particles in the iterations of the PSO algorithm for the benchmark test problem.

For the sake of completeness, the force-displacement curve corresponding to the identified model parameters accurately matches the target one; see Fig. 12.

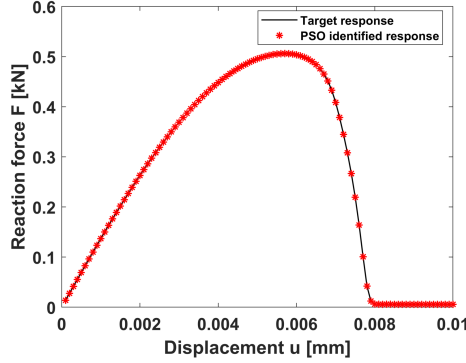


Figure 12: Force-displacement curve and target curve.

The robustness of the PSO algorithm is also assessed by considering six different cases with parameters spanning over the G_c and l_c space for a fixed value of $E = 210$ GPa, see Table. 2. The same geometry and loading conditions are considered for analysis as mentioned in Fig. 9.

Case	G_c (kN/mm)	l_c (mm)	Range E (GPa)	Range G_c (kN/mm)	Range l_c (mm)	Absolute error % $\{E, G_c, l_c\}$
1	2.7	0.3	180 – 230	1.2 – 3.8	0.02 – 0.45	{0.078, 0.10, 0.037}
2	2.7	0.5	180 – 230	1.2 – 3.8	0.02 – 0.70	{0.116, 0.07, 0.018}
3	2.7	0.7	180 – 230	1.2 – 3.8	0.02 – 0.90	{0.312, 0.11, 0.048}
4	4.0	0.1	180 – 230	1.2 – 5.5	0.02 – 0.20	{0.297, 0.38, 0.032}
5	6.5	0.1	180 – 230	1.2 – 8.0	0.02 – 0.20	{0.078, 0.28, 0.015}
6	8.0	0.1	180 – 230	1.2 – 10.0	0.02 – 0.20	{0.252, 0.28, 0.014}
7	4.0	0.1	180 – 230	1.2 – 5.5	0.02 – 0.20	{1.075, 1.49, 0.107}
8	4.0	0.1	180 – 230	1.2 – 5.5	0.02 – 0.20	{0.120, 0.14, 0.009}

Table 2: Set of input data to generate target responses and range of parameters for the robustness test. The last column reports the error of the identified parameters with respect to the values used in input.

Initial and final particles' positions are shown in Fig. 14 for cases 1, 2 and 3 related to the different values of l_c and in Fig. 15 for cases 4, 5 and 6 related to the different values of G_c . Further to assess convergence of the PSO algorithm, velocity of the constriction factor-based approach

[191] is adopted for case 8 (see Eq. (3.3)) with positive weights applied to certain force-displacement points to set a priority while determining cost function (Υ) and all point in the force-displacement curve are treated equally (no different weights are applied). In this approach to guarantee stability [196], φ was set as 4.1 and $\mathbf{C}_c = \mathbf{S}_c = 2.05$. The velocity of the swarm particles is computed according to the following equation:

$$\begin{aligned} \mathbf{V}_i^k &= \kappa \times (\mathbf{V}_i^{k-1} + \mathbf{C}_c \times \mathbf{r}_1 \times (\mathbf{P}_i^k - \chi_i^k) + \mathbf{S}_c \times \mathbf{r}_2 \times (\mathbf{P}_g^k - \chi_i^k)) \\ \kappa &= \frac{2}{|2 - \varphi - \sqrt{\varphi^2 - 4\varphi}|}, \text{ where } \varphi = \mathbf{C}_c + \mathbf{S}_c, \varphi > 4 \end{aligned} \quad (3.3)$$

where κ is a constriction factor and $\mathbf{r}_1, \mathbf{r}_2$ are random numbers between 0 and 1. The remaining parameters explanation is mentioned in Section 3.2.2

3.2.2 Particle swarm optimization methodology

Particle swarm optimization (PSO) is applied to a continuous spatial domain where the cost function Υ is minimized to converge swarm particles in the solution space region to the optimized position. Let us assume there are N_p swarm particle size population in a ' φ ' dimensional parametric space domain. $\chi_i := [\mathbf{x}_{i1}, \mathbf{x}_{i2} \dots, \mathbf{x}_{i\varphi}]$, $\mathbf{V}_i := [\mathbf{v}_{i1}, \mathbf{v}_{i2} \dots, \mathbf{v}_{i\varphi}]$ is the individual swarm particle's position vector, velocity vector respectively where $i = 1, 2, \dots, N_p$ denotes the swarm particle number. $\mathbf{P}_i := [\mathbf{P}_{i1}, \mathbf{P}_{i2} \dots, \mathbf{P}_{i\varphi}]$ is each swarm particle's optimal position vector. $\mathbf{P}_g := [\mathbf{P}_{g1}, \mathbf{P}_{g2} \dots, \mathbf{P}_{g\varphi}]$ is the swarm global optimum position vector considering all swarm particle's.

In the main loop of PSO at each iteration k individual swarm particle updates its position by first computing updated velocity vector in φ space region considering previous results in φ search space such as velocity \mathbf{V}_i^{k-1} (inertia influence), best-known position \mathbf{P}_i^{k-1} (cognitive influence), swarm best known global position \mathbf{P}_g^{k-1} (social influence) and PSO algorithm parameters $\mathbf{W}_i, \mathbf{C}_c, \mathbf{S}_c$

$$\mathbf{V}_i^k = \mathbf{W}_i \times \mathbf{V}_i^{k-1} + \mathbf{C}_c \times (\mathbf{P}_i^k - \chi_i^k) + \mathbf{S}_c \times (\mathbf{P}_g^k - \chi_i^k) \quad (3.4)$$

$$\chi_i^k = \chi_i^{k-1} + V_i^k \quad (3.5)$$

The local and global best particle position is calculated by following the equation

$$\mathbf{P}_i^k = \begin{cases} \chi_i^k & \text{if } \Upsilon(\chi_i^k) < \Upsilon(\mathbf{P}_i^{k-1}) \\ \mathbf{P}_i^{k-1} & \text{otherwise} \end{cases} \quad (3.6)$$

$$\mathbf{P}_g^k = \begin{cases} \mathbf{P}_i^k & \text{if } \Upsilon(\mathbf{P}_i^k) < \Upsilon(\mathbf{P}_g^{k-1}) \\ \mathbf{P}_g^{k-1} & \text{otherwise} \end{cases} \quad (3.7)$$

The robustness of the PSO algorithm is further examined by comparing case 4 without weights, case 7 with weights, and case 8 with weights but also considering the constriction factor for velocity. Fig. 13 clearly shows better convergence of case 8 as compared to cases 4 and 7.

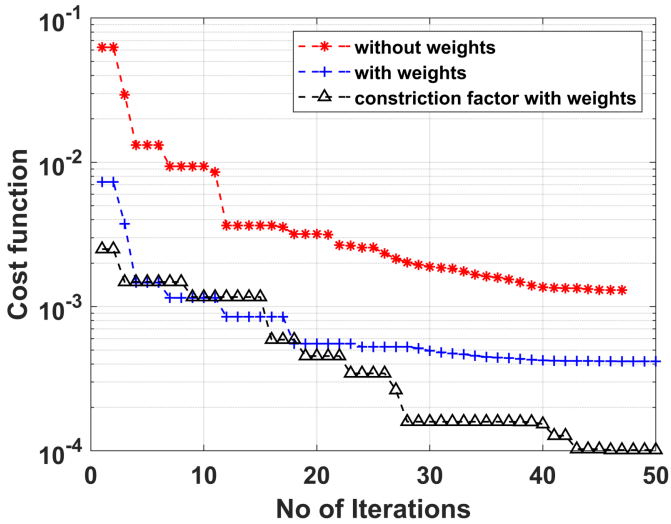
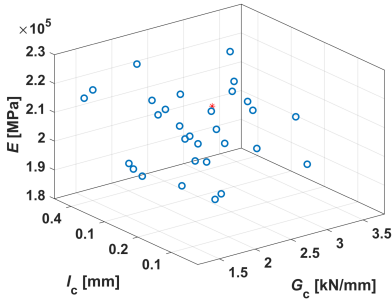
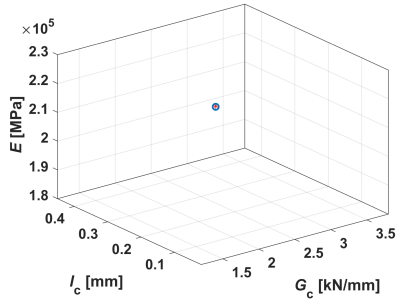


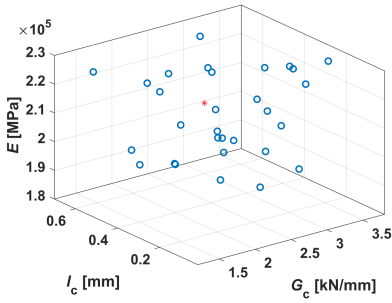
Figure 13: Convergence study of the PSO algorithm for cases 4, 7, and 8, see Table. 2.



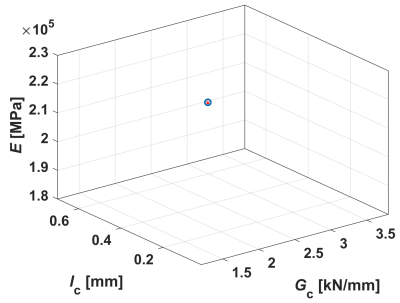
(a) Initial particles' position (case 1)



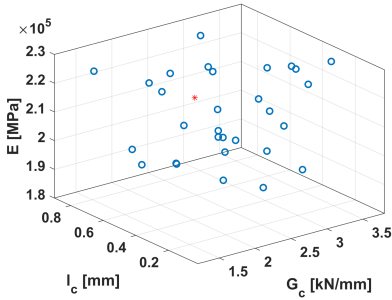
(b) Iteration No. 44



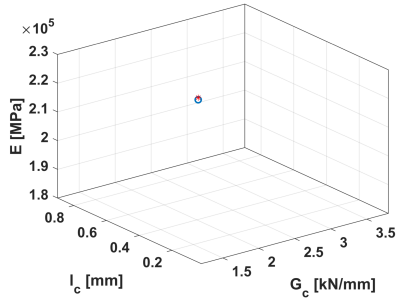
(c) Initial particles' position (case 2)



(d) Iteration No. 50

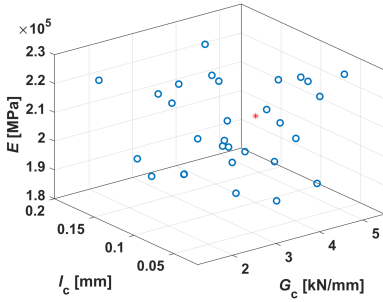


(e) Initial particles' position (case 3)

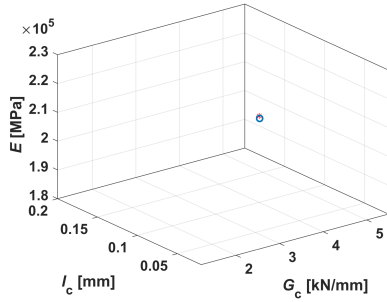


(f) Iteration No. 51

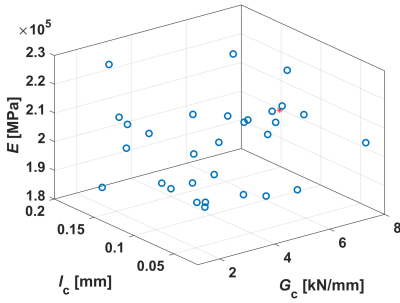
Figure 14: Scatter representation of particles' position for cases 4, 5, and 6 whose parameters are collected in Table. 2.



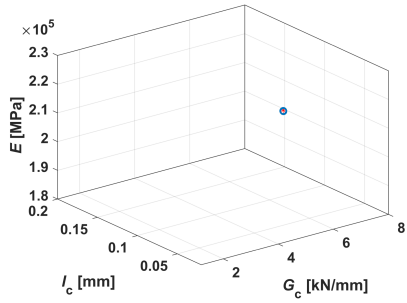
(a) Initial particles' position (case 4)



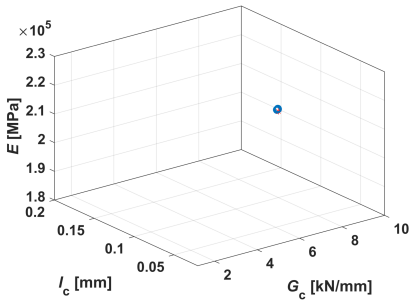
(b) Iteration No. 47



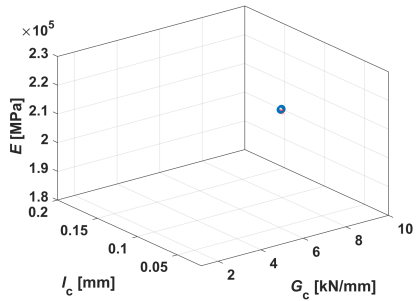
(c) Initial particles' position (case 5)



(d) Iteration No. 42



(e) Initial particles' position (case 6)



(f) Iteration No. 38

Figure 15: Scatter representation of particles' position for cases 1, 2, and 3 whose parameters are collected in Table. 2.

3.2.3 Identification of cohesive zone graded interface properties

The benchmark test in Section 2.5 motivates the development of a machine learning technique that can automatically identify the properties of a linearly graded cohesive interface to achieve a desired (target) mechanical response. For those problems, the target response can be the maximum reaction force measured during the peeling test or even a measure of the error in a suitable norm between the predicted force-displacement curve and the experimental one to be identified.

For what concerns the candidate algorithms, there are numerous nature inspired [102, 101, 103], evolutionary [197], and population [105] based algorithms available in the literature. In the present work, particle swarm optimization (PSO), a machine learning algorithm best suited for data-driven inverse problems [28, 1], is exploited to identify the interface properties. PSO [102] is a nature-inspired algorithm that looks for the best answer inside the solution space. It does not rely on the gradient of the objective function, whose functional expression is unknown, while it requires the sampling of the objective function in the hyper-parameter space, so it can be considered as a data-driven approach.

The method is based on a certain number of swarm particles dispersed in the solution space, and we seek to converge to a solution that minimizes the cost function Υ . The model test problem (see Fig. 16) with linearly graded interface properties is herein examined. The cost function to be minimized is herein defined as the error in the L2 norm between the predicted and the desired reaction force-displacement curve:

$$\Upsilon(\chi) = 1 - \frac{1}{N} \sum_{d=1}^N \sqrt{\left[\frac{\Delta R x_d(\chi)}{\hat{R} x_{\max}(\chi)} \right]^2} \quad (3.8)$$

where $\Delta R x_d(\chi) = R x_s - R x_t(\chi)$. $R x_s$ denotes the history of simulated reaction forces for the range of imposed pseudo-time steps d ($d = 1, \dots, N$). The model test problem is conducted under displacement control till the N values of applied displacement are imposed, for a given set of PSO model parameters. Analogously, $R x_t(\chi)$ represents the tar-

get value of the reaction forces for the same values of the N imposed displacements. $\hat{R}x_{\max}(\chi) = \max(\max(Rx_s), \max(Rx_t(\chi)))$ denotes the maximum value of the reaction force out of the $Rx_s, Rx_t(\chi)$ values considering N imposed displacements. The cost function would tend to $\Upsilon(\chi) = 1$ if the PSO simulated curve and the target response are the same. The properties chosen to numerically generate the target response for a linear graded interface are $\sigma_{\max} = \tau_{\max} = 20$ MPa, $g_{n_c} = g_{t_c} \in (2.5 - 7.5)$ mm.

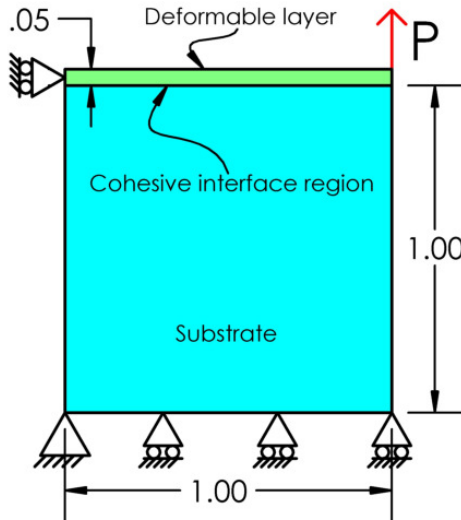
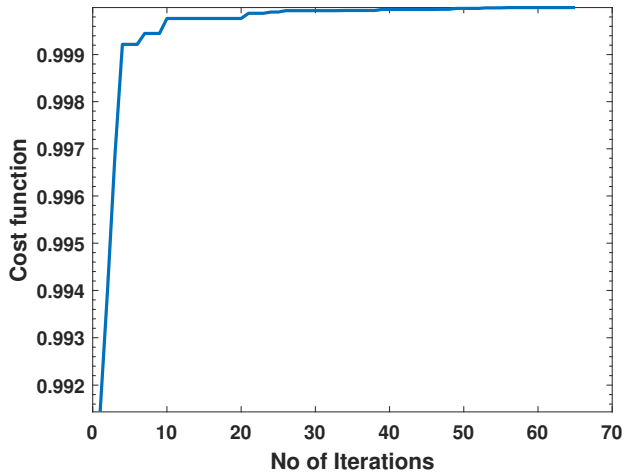
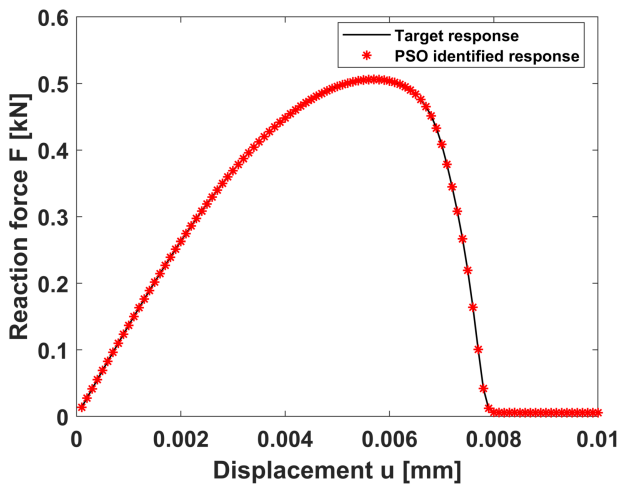


Figure 16: Model sketch of the peeling test.

For the inverse parameter identification problem, three properties are considered as free parameters: the maximum normal traction, σ_{\max} , the critical normal gap $(g_{n_c})_L$ for the interface at $x = L$, and the critical normal gap $(g_{n_c})_0$ at $x = 0$. The Mode II model parameters: the maximum shear traction, τ_{\max} , the critical tangential gaps $(g_{t_c})_L, (g_{t_c})_0$ for the interface at $x = L, x = 0$ respectively are set the same as Mode I model parameters during analysis and therefore are not included in the parametric space.

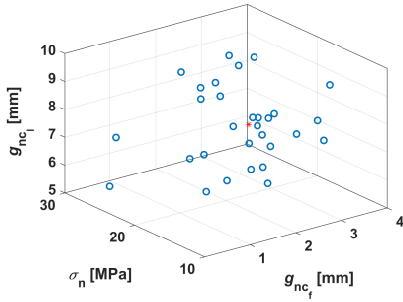


(a) Cost function

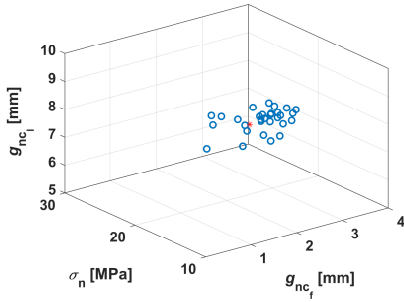


(b) Identified response at convergence

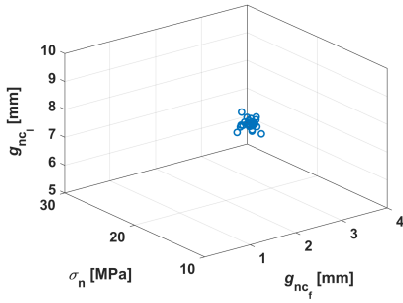
Figure 17: (a) Cost function vs. number of PSO iterations; (b) comparison between PSO identified response and target response at convergence for the peeling test problem with a linearly graded interface.



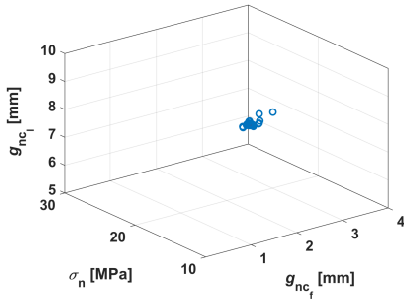
(a) Initial particles' position



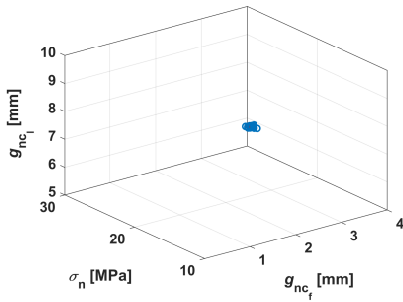
(b) Iteration No. 4



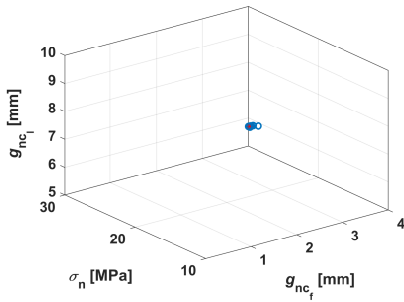
(c) Iteration No. 15



(d) Iteration No. 30



(e) Iteration No. 45



(f) Iteration No. 65

Figure 18: Position of the particles during the progress of the iterations of the PSO algorithm applied to the peeling test problem with a linearly graded interface.

The feasibility domain is defined sufficiently wide to explore all the physical solutions of the problem that are of potential interest:

$$\mathcal{L} = \{10 < \sigma_n < 30 \text{ MPa}; 0.01 < (g_{n_c})_0 < 4 \text{ mm}; 5 < (g_{n_c})_L < 10 \text{ mm}\} \quad (3.9)$$

The implementation of the PSO constriction factor-based approach [191], as discussed in Section 3.2.1, is exploited here to identify the cohesive interface parameters. The application of PSO to the present problem leads to the evolution of swarm particles' position within the design solution space shown in Fig. 18. The identified interface fracture properties at the end were $\sigma_{max} = 20.0001 \text{ MPa}$, $(g_{n_c})_0 = 2.5221 \text{ mm}$, and $(g_{n_c})_L = 7.5 \text{ mm}$, which are very close to the values used to generate the target curve.

The evolution of the cost function is depicted in Fig. 17(a), and the comparison between the identified response and the target response at convergence is shown in Fig. 17(b).

3.3 Comparison of machine learning techniques

From previous Section 3.2, we confirm that the PSO algorithm accurately identifies fracture parameters. Now the question arises: is PSO the best out of all meta-heuristic algorithms mentioned in Section 3.1?. The present section answers the above posed question by investigating the performance of metaheuristic optimization algorithms when applied to inverse phase-field fracture mechanics problems, which are required to identify model parameters to match a given output response. The above-selected algorithms as mentioned in Section 3.1 are compared in relation to a notched specimen tested under tensile loading and for a single edge notched bending (SENB) testing geometry to evaluate their efficiency in the identification of the phase-field fracture mechanics parameters. The initial population is set the same for all algorithms for the purpose of a consistent comparison. The geometry, loading, and boundary conditions of the two test problems are shown in Figs. 19 and 20, respectively. The following material properties are considered to be identi-

fied: Young’s modulus E , the fracture energy G_c , and the internal length scale parameter l_c . The isotropic case ($\beta = 0$) is examined and the target force-displacement target response curves for each test are synthetically generated based on the set of parameters collected in Table. 3. The set of parameters for the two test problems are selected to be very different to assess the reliability of the methods in the case of materials with very small or very large fracture energies. The initial population size of the variables is $N_p = 30$ and is randomly dispersed in the design-constrained space. The search space is defined in such a way to obtain a feasible optimal parameter solution. The design-constrained space is also reported in the same table. The combined PFF-MLA pseudo algorithm, which integrates all the various optimization algorithms, is described in Algorithm.3.

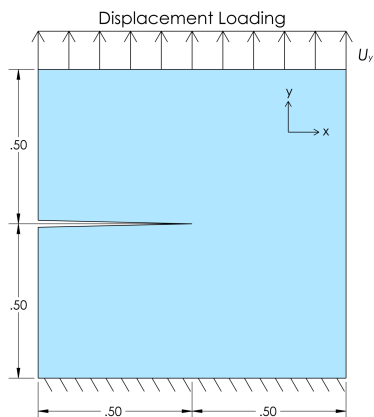


Figure 19: Geometry and boundary conditions of the tensile test problem for an edge notched specimen.

The particles’ position within the design space at the end of the execution of the PFF-MLA algorithms (solution corresponding to the respective minima of the cost functions) for the two test problems are shown in blue in Figs. 21, 22, respectively.

For the first test case related to the edge-notched specimen under

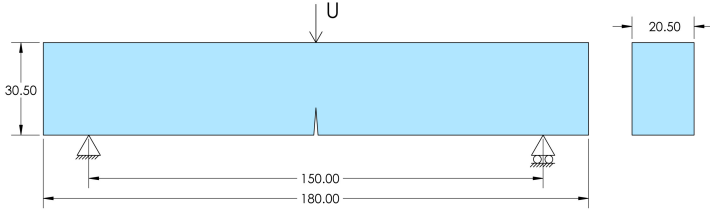


Figure 20: Geometry and boundary conditions of the SENB test problem.

Test problem	E (GPa)	G_c (N/mm)	l_c (mm)	Range E (GPa)	Range G_c (N/mm)	Range l_c (mm)
Tensile test	210	2700	0.3	180 - 230	1200 - 3800	0.02 - 0.45
SENB test	1.4	7.5	1.2	0.9 - 2.5	1.5 - 12.5	0.3 - 3

Table 3: Input data to generate target responses and range of parameters for the search space of the identification algorithms.

tensile loading (Fig. 21), the values to be identified are $E = 210$ GPa, $G_c = 2.7$ kN/mm, $l_c = 0.1$ mm and are shown with a red star in the figures. They were closely matched by the PSO algorithm, see Fig. 21(a). The PSO-GA and the ABC-PSO algorithms almost converged to the optimum solution, although not exactly matching the target (Figs. 21(b) and 21(c)). The CS algorithm did not converge to the target solution (Fig. 21(d)) because the variables are trapped within their local minima. The solution variables from the EJAYA and TLBO optimization algorithms converged to a single point (Figs. 21(e) and 21(f)), which however does not match the target values.

The same analysis is herein repeated for the SENB test problem (Fig. 22). The PSO algorithm shows a good convergence to the target solution ($E = 1400$ MPa, $G_c = 7.5$ N/mm, $l_c = 1.2$ mm), see Fig. 22(a). The PSO-GA, EJAYA, and the TLBO algorithms converge to points away from the target solution, see Figs. 22(b), 22(e), and 22(f). The ABS-PSO and CS algorithms, as for the previous test problem, do not converge, see Figs. 22(c) and 22(d).

Hence, the above analysis shows that PSO is the most accurate and robust algorithm for phase-field fracture mechanics parameters' identification as compared to the PSO-GA, ABC-PSO, CS, EJAYA, and TLBO algo-

rithms. This is further observed by the comparison among the simulated force-displacement curves obtained at the end of the execution of each optimization algorithm, where the PSO algorithm accurately matches the target response curve for both test problems, see Figs. 23(a) and 23(b).

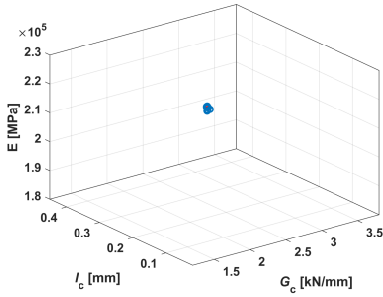
The results are further supported by checking and ensuring the solution obtained from the PSO algorithm during each optimization iteration is trapped in local minima. The value of the cost function $f(\chi_{\text{opt}})$ during each iteration is calculated from Eq. 3.10 and it steadily decays with the number of iterations in both testing problems, see Fig. 24. The plot further confirms the comments on the results plotted in Figs. 21 and 22, showing the difficulty of some meta-heuristic algorithms to reduce the value of the cost function towards zero.

$$f(\chi_{\text{opt}}) = \sqrt{\sum_{d=1}^n \left[\frac{\Delta R x_d(\chi_{\text{opt}})}{R x_t(\chi_{\text{opt}})} \right]^2} \quad (3.10)$$

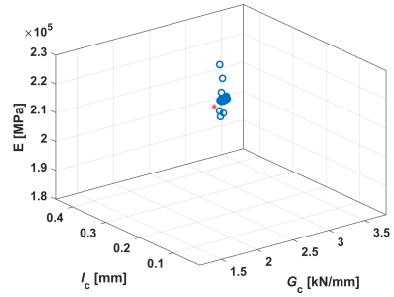
The above results confirm that the PSO algorithm is an efficient and robust optimization method compared to PSO-GA, ABC-PSO, CS, EJAYA, and TLBO algorithms to identify phase-field fracture mechanics parameters. Therefore, the PSO algorithm is explored in Section 5.2.2 to study the influence of anisotropic parameter β in addition to E, G_c, l_c parameters.

Algorithm 3 Integrated phase-field fracture (PFF) - machine Learning algorithm (MLA) for parameters' identification

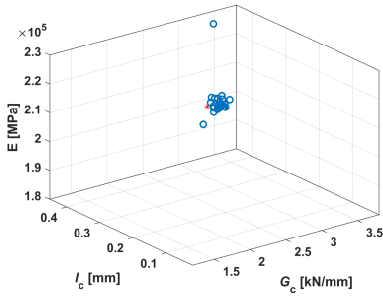
- 1: Initialization
 - 2: **Input data:** population size N_p , maximum number of iterations It_{\max} , MLA algorithm tuning parameters (if required)
 - 3: **Output data:** optimized solutions \mathbf{P}_{opt} at the minimum of the cost function Υ
 - 4: ~~Initialization~~
 - 5: **for all** $i = 1, \dots, N_p$ **do**
 - 6: Generate a population with random position χ_i^0 in the 3D ($\wp = 3$) parametric space (E, G_c, l_c) within the search space.
 - 7: Evaluate cost function $\Upsilon(\chi_i^0)$ by the phase-field for fracture FE model.
 - 8: **end for**
 - 9: Assign $\mathbf{P}_{\text{opt}} \leftarrow \text{argmin} \Upsilon(\chi_i^0)$
 - 10: ~~Main loop of MLA algorithm~~
 - 11: **for** $k = 1, \dots, It_{\max}$ **do**
 - 12: **for all** $i = 1, \dots, N_p$ **do**
 - 13: Update solution χ_i^k based on the MLA algorithm
 - 14: **if** $\chi_i^k \notin \wp$ **then**
 - 15: reassign randomly χ_i^k in \wp
 - 16: **end if**
 - 17: **end for**
 - 18: $\mathbf{P}_{\text{opt}} \leftarrow \chi_{\text{opt}}$
 - 19: **end for**
-



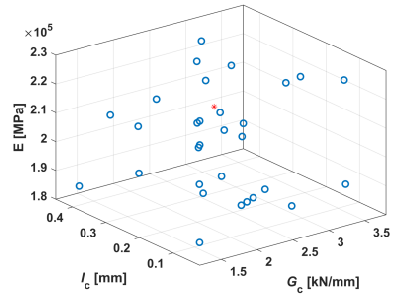
(a) PSO



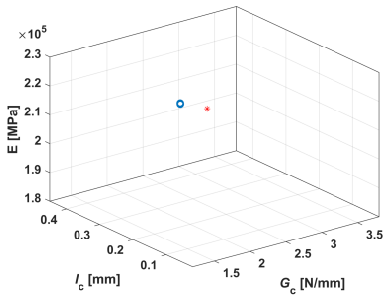
(b) PSO-GA



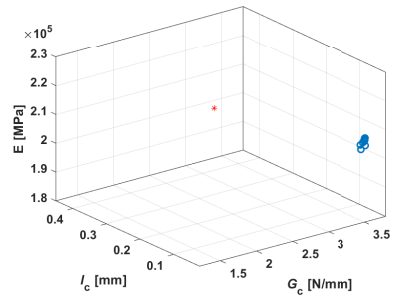
(c) ABC-PSO



(d) CS



(e) EJAYA



(f) TLBO

Figure 21: Comparison of the particles' position predicted by the different optimization algorithms for the tensile test problem with an edge-notched specimen. Not all the algorithms converge to the target response shown with a red star.

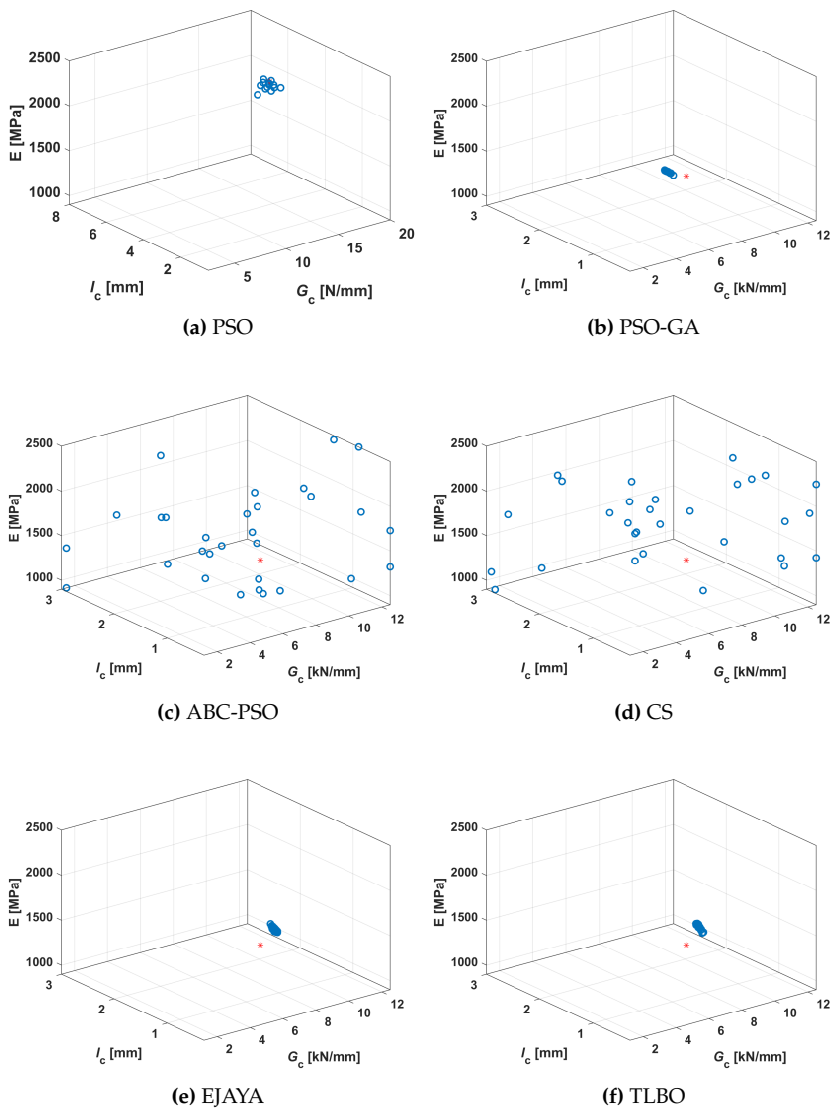
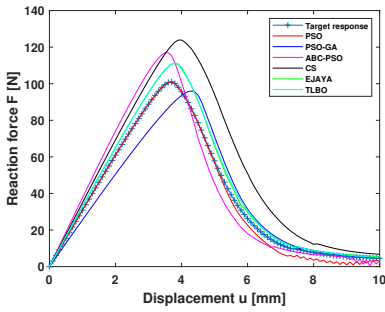
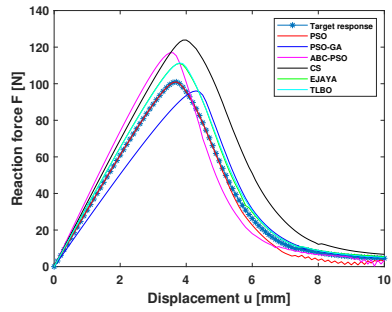


Figure 22: Comparison of the particles' position predicted by the different optimization algorithms for the SENB test problem. Not all the algorithms converge to the target response shown with a red star.

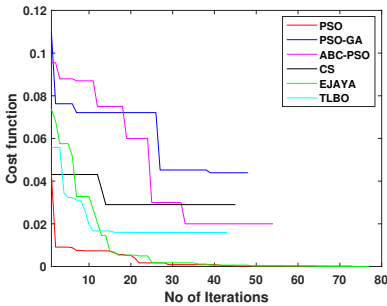


(a) Tensile test with edge-notched specimen

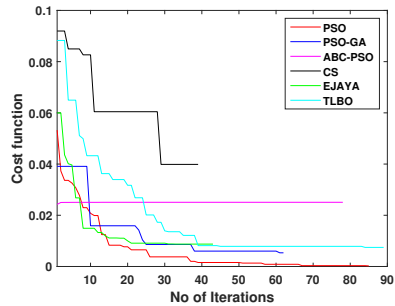


(b) SENB test

Figure 23: Force vs. displacement curves at the end of the execution of the different optimization algorithms; the target response is highlighted by blue stars.



(a) Tensile test with edge-notched specimen



(b) SENB test

Figure 24: Cost function vs. number of iterations for the different meta-heuristic algorithms.

Chapter 4

Topology optimization methods for structural problems

Chapter 4 is partially based on the content of article in press [3].

Topology optimization of structures is a sophisticated computational technique focused on optimizing material distribution within a designated design space to achieve superior structural performance with minimal material use. We define an objective function, such as minimizing weight or maximizing stiffness, and apply various constraints, iteratively adjusting the material layout using methods like Solid Isotropic Material with Penalization (SIMP). Finite Element Analysis (FEA) is used to assess structural performance under applied loads at each step. This iterative process continues until an optimal or near-optimal design is achieved, effectively balancing efficiency and performance. Topology optimization is widely applied in aerospace, automotive, civil engineering, and biomedical fields to develop lightweight, cost-effective, and innovative designs. Despite challenges such as high computational costs and manufacturability issues, advances in additive manufacturing are making the realization of complex optimized structures increasingly feasible. Motivated by the above aspects, this chapter provides a detailed discussion of the mathematical formulation and numerical implementation of the topology optimization method for structural

problems, with a particular focus on fracture issues.

4.1 Mathematical formulation of topology optimization

Consider a design domain Ω discretized into N_e finite elements, and each element e is assigned a topology density variable ϕ_e . The solid isotropic with penalization (SIMP) material interpolation [119] is incorporated in the design domain, which is controlled by the continuous design density variable ϕ_e . The design variable ϕ_e ranges between 0 – 1, which varies within the discrete element of the structure, with 0 being for void material and 1 for solid material. Hence, the material is interpolated as follows:

$$E(\phi_e) = E_{\min} + \phi_e^p (E_0 - E_{\min}), \quad \phi_e \in [0, 1] \quad (4.1)$$

where $E(\phi_e)$ denotes Young's modulus of the e -th element, E_{\min} is a dummy Young's modulus much smaller than the other ones to model a void (here we set it equal to 10^{-9}). E_0 is Young's modulus of the material whose shape has to be optimized, p is a penalty coefficient, and in the literature, a value of 3 [164] is typically chosen to ensure a clear distinction between a solid and a void.

The general mathematical formulation of the optimization problem reads as follows:

$$\begin{aligned} \text{Minimize: } C(\phi) &= \mathbf{U}^T \mathbf{K} \mathbf{U} = \sum_{e=1}^N E_e(\phi_e) \mathbf{u}_e^T \mathbf{k}_0 \mathbf{u}_e \\ \text{subject to: } & \mathbf{K} \mathbf{U} = \mathbf{F} \\ & \sum_{e=1}^{N_e} \phi_e v_e / \left(\sum_{e=1}^{N_e} v_e \right) = f \\ & 0 \leq \phi_e \leq 1; \quad e = 1, 2, \dots, N_e \end{aligned} \quad (4.2)$$

where $C(\phi)$ is the objective function that depends on the design variable ϕ , and it is proportional to the internal work of the mechanical system. v_e represents the e -th elemental volume in the design domain, such that the

material distribution has to comply with the prescribed volume fraction f . \mathbf{K}, \mathbf{U} , and \mathbf{F} represent the assembled global stiffness vector, displacement vector, and load vector.

The optimization problem in Eq. (4.2) can be solved by means of optimality criteria method [171, 198] based on the following heuristic updating scheme:

$$\phi_e^{\text{new}} = \begin{cases} \max(0, \phi_e - m) & \text{if } \phi_e B_e^\zeta \leq \max(0, \phi_e - m) \\ \min(1, \phi_e + m) & \text{if } \phi_e B_e^\zeta \geq \min(1, \phi_e - m) \\ \phi_e B_e^\zeta & \text{otherwise} \end{cases} \quad (4.3)$$

where m is a positive moving limit, $\zeta = 1/2$ is a numerical damping coefficient, and B_e is obtained from the KKT optimality condition given below:

$$B_e = -\frac{\partial c(x)}{\partial \phi_e} \left(\Lambda \frac{\partial v(x)}{\partial \phi_e} \right)^{-1} \quad (4.4)$$

where Λ is a Lagrangian multiplier chosen to satisfy the volume constraint, and its appropriate value can be found by employing a bisection algorithm. Moreover, the sensitivities of the objective function $c(x)$ and the material volume v concerning the element densities ϕ_e are computed as:

$$\begin{aligned} \frac{\partial c(\phi)}{\partial \phi_e} &= -p\phi_e^{p-1} (E_0 - E_{\min}) \mathbf{u}_e^T \mathbf{k}_0 \mathbf{u}, \\ \frac{\partial v(\phi)}{\partial \phi_e} &= 1. \end{aligned} \quad (4.5)$$

4.1.1 Filtering technique

To ensure the existence of solutions to the topology optimization problem and to avoid the formation of checkerboard patterns [199, 200] the sensitivity filtering technique [164] is introduced as follows:

$$\tilde{\rho}_e = \frac{\sum_{j \in N_e} W_{e,j} \phi_j \frac{\partial c(\phi)}{\partial x_j}}{\max(\varpi, \phi_e) \sum_{j \in N_e} W_{e,j}} \quad (4.6)$$

where

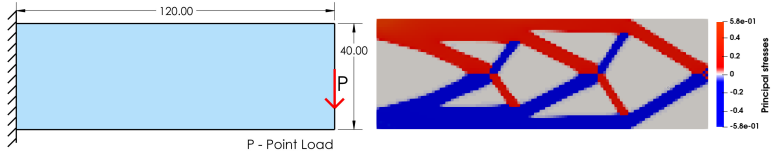
$$W_{e,j} = \begin{cases} \frac{R_0 - r_{ej}}{R_0} & \text{for } r_{ej} < R_0 \\ 0 & \text{for } r_{ej} \geq R_0 \end{cases} \quad (4.7)$$

being $\tilde{\rho}_e$ the sensitivity filter which modifies the sensitivities of the objective function $c(\phi)$ in Eq. (4.5), N_e is the subset containing the surrounding elements within the filtered radius R_0 to the e -th element, ϖ in Eq. (4.7) is set equal to 10^{-3} to avoid division by zero. $W_{e,j}$ is the linearly decaying cone shape weighted filtering function of elements e and j , x_j is the non-filtered density of the j -th element within the filtered radius R_0 , r_{ej} is the distance between the center of the element e to that of the element j .

4.1.2 Benchmark tests for structural topology optimization

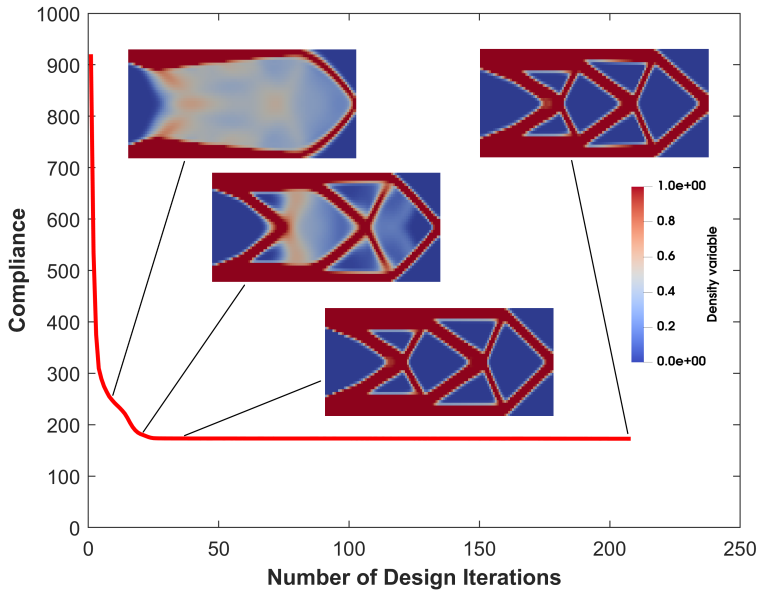
The results of a series of benchmark tests well-known in the literature used to test the structural topology optimization algorithm. The algorithm for topology optimization proposed in [171] is dealt with in the present work. The problems are related to beams with different constraints and loads, and all are discretized with 120×40 finite elements. The results in terms of compliance vs. number of iterations are shown in the figures below, see Figs. 25, 26, 27 and 28. Finally, the method is applied to an L-geometry in Fig. 29.

For all the benchmark problems, a filtered radius $r_{\min} = 2$ mm, a Young modulus $E_0 = 210$ GPa, a Poisson ratio $\nu = 0.3$ and a Young modulus $E_{\min} = 1 \times 10^{-9}$ assigned to void regions are considered. The constrained volumetric fraction f has been set equal to 0.5. The compliance decreases with respect to the number of design iterations and converges to a minimal value. The optimized topology of the structure is greatly affected by boundary conditions and correctly predicted as in the related literature [201, 164, 202]. The principal stress distribution for each optimum structural topology has been highlighted, where red and blue colors refer to tensile and compressive stresses, respectively. Principal stress distribution diagrams might be useful and can be converted to STL (Standard Triangle Language) file format, which can be exploited for 3D printing operations.



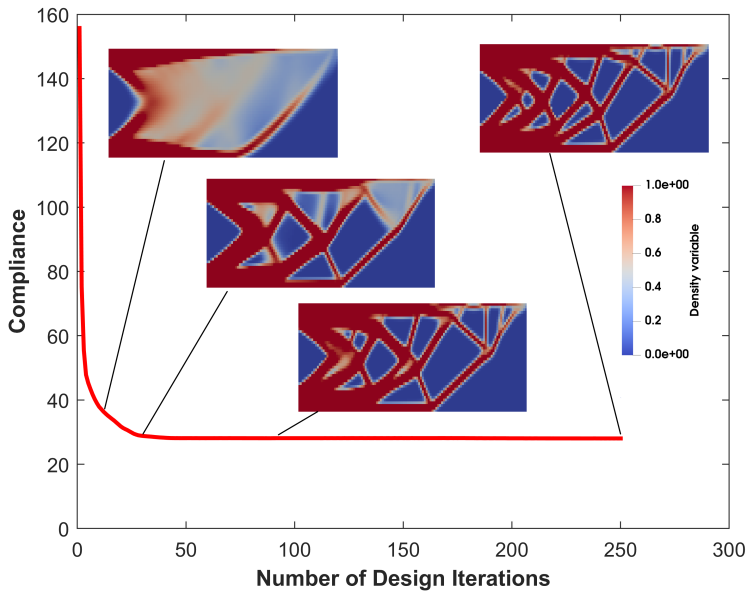
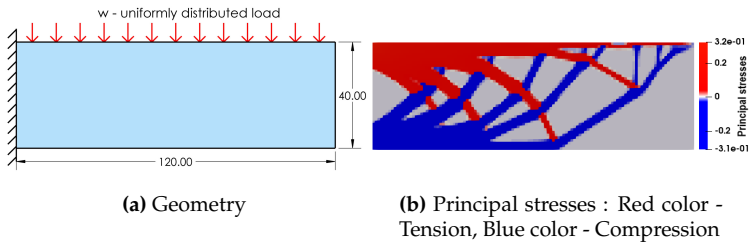
(a) Geometry

(b) Principal stresses : Red color - Tension, Blue color - Compression



(c) Compliance versus Number of design iterations

Figure 25: Structural topology evolution of cantilever beam subjected to point load



(c) Compliance versus Number of design iterations

Figure 26: Structural topology evolution of cantilever beam subjected to uniformly distributed load

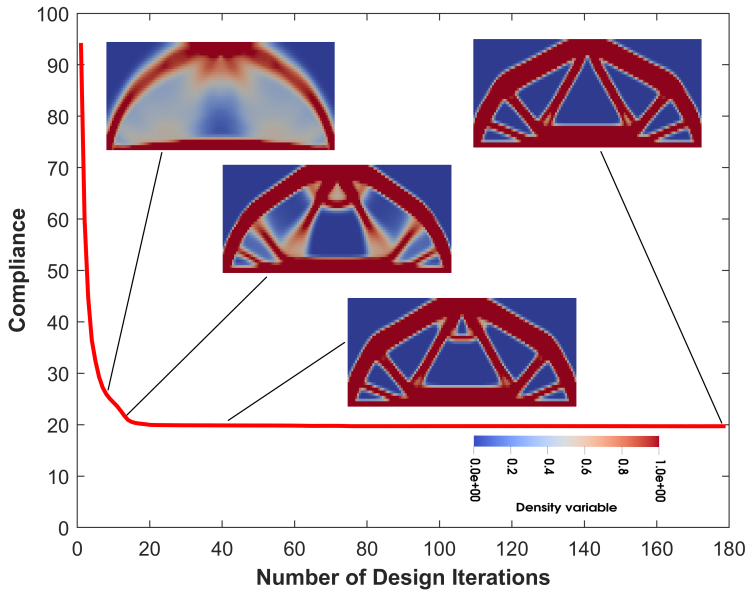
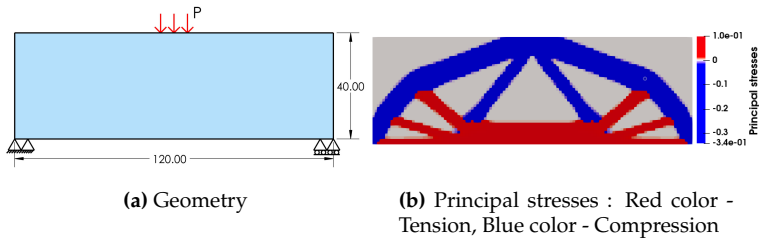


Figure 27: Structural topology evolution of simple supported beam subjected to point load

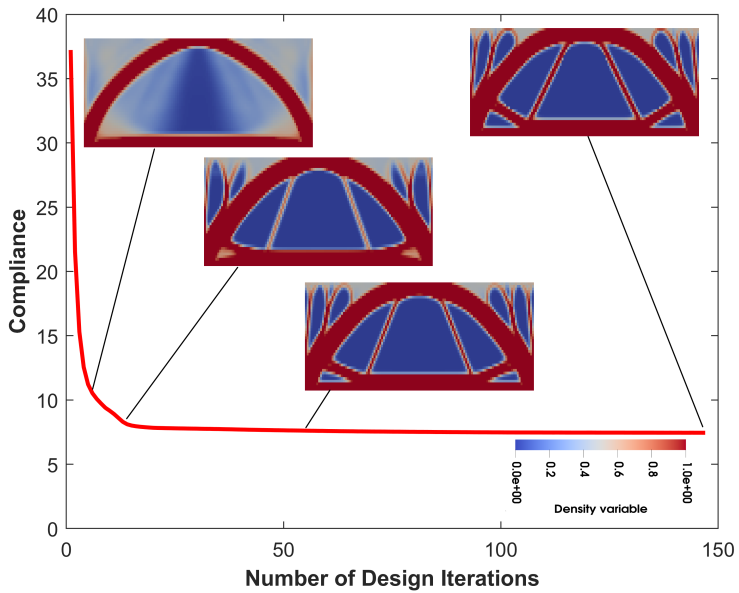
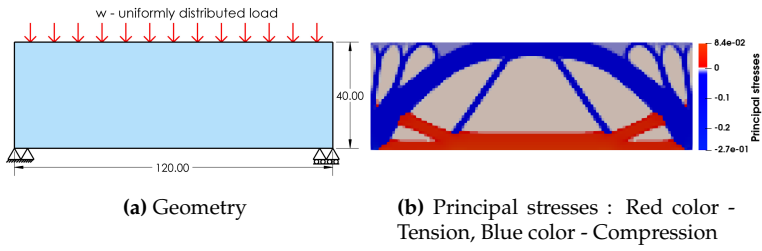
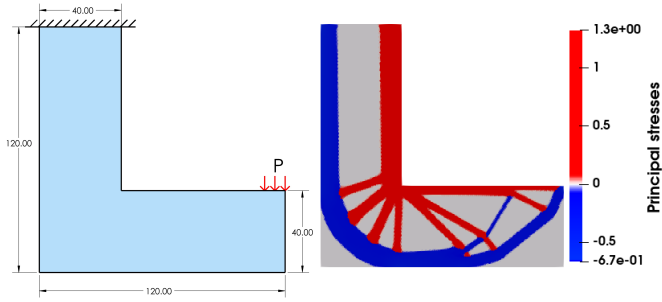
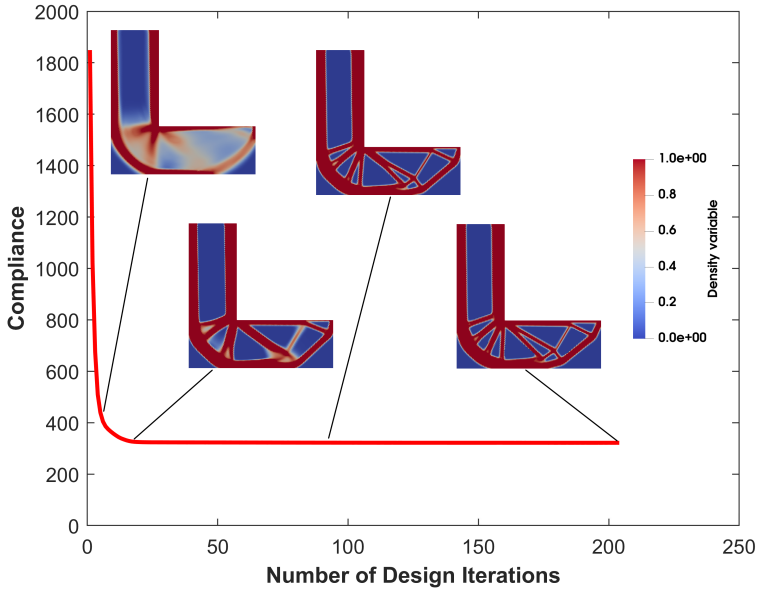


Figure 28: Structural topology evolution of simple supported beam subjected to uniformly distributed load



(a) Geometry

(b) Principal stresses : Red color - Tension, Blue color - Compression



(c) Compliance versus Number of design iteration

Figure 29: Structural topology evolution of L-bracket subjected to point load

4.2 Topology optimization of substrates prone to delamination

Now, in this section, we deal with structural design topology optimization problems under the influence of cohesive interface fracture. The methodology is challenged here in relation to the problem geometry already investigated in the Section 2.5.1, where a thin layer is peeled off from the substrate; see the sketch in Fig. 30. In this problem, the interface region has been discretized with 75 elements along its length, while the deformable layer has been discretized with 75 elements along its length and 8 over its thickness, and the optimization region (substrate) is discretized with 75×75 elements. The top right corner of the deformable layer has a prescribed displacement imposed, that leads to a reaction force P during the evolution of delamination.

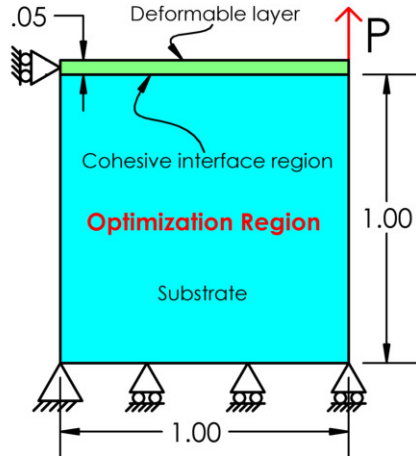


Figure 30: Sketch of peeling test with boundary conditions for a substrate with a delaminating interface, where the topology of the substrate has to be optimized to maximize the stiffness of the mechanical system for different levels of delamination.

The substrate region is the focus of our study concerning topology optimization. Linearly graded cohesive interfacial properties are set equal

to $\sigma_{\max} = \tau_{\max} = 10$ MPa, $g_{n_c} = g_{t_c} \in (2.5 - 7.5)$ mm, where the critical normal and tangential gaps vary both linearly from 2.5 mm at $x = 0$, up to 7.5 mm at $x = L$.

Considering a displacement load that increases linearly over a pseudo-time variable, we can simulate stress conditions in the substrate corresponding to varying degrees of progressive delamination of the bonded layer, focusing on scenarios typical of the onset of debonding. The topology optimization algorithm is applied after a specific portion of the interface layer has debonded, and the structural topology evolution of the substrate is studied. Further results investigate the influence of the substrate volume fraction on optimum topology and compliance values, followed by a study on topology optimization of the substrate subject to different prescribed displacement loading conditions, which in the present case correspond to different portions of initial interface delamination.

4.2.1 Impact of volume fraction

The optimum topology of the substrate was initially studied for different volume fractions under identical loading conditions. For this analysis, five different substrate volume fractions $f = 10\%$, 20% , 30% , 40% , and 50% were examined. The numerical topology optimization process, as outlined in Fig. 33, was applied. Initially, a total displacement of 9 mm was imposed at the top-right corner node, resulting in delamination up to 0.08 mm along the interface. Subsequently, the topology optimization (TO) process was conducted for various substrate volume fractions. The findings indicate that the volume fractions $f = 10\%$ and 20% did not yield practically feasible designs and exhibited very high oscillations in compliance value throughout the iterations. However, volume fractions $f = 40\%$ and 50% are promising for achieving feasible optimized topological designs as depicted in Figs. 34(b),(c). In the figures, red represents the solid material, while blue indicates the void. Interestingly, the topology pattern remains consistent for $f = 30\%$, 40% and 50% volume fraction-optimized structures. The impact of volume fraction f on the mean compliance for $f = 30\%$, 40% and 50% is shown in Fig. 32, which

shows a decrease in the mean compliance with an increase in volume fraction f . A comparison of the compliance value with respect to the number of design iterations for volume fractions $f = 30\%$, 40% and 50% is shown in Fig. 31, revealing that the optimized substrate with $f = 50\%$ is stiffer than those with $f = 30\%$ and 40% , as more material volume is available to resist delamination. This study provides valuable insights into evaluating the best-optimized designs for interface problems while considering cost implications without compromising the system's performance. This analysis is highly beneficial for industrial applications focused on finding optimized structures, especially when design constraints are clearly defined, to ensure better functionality of the structure.

4.2.2 Examples

We examined two cases to study the topology evolution of the substrate under different far-field imposed displacements. The volume fraction f of the substrate is set to 0.5, which provides better structural strength out of $f = 30\%$, 40% and 50% as mentioned in Section 4.2.1. In the first case, a total displacement of 9 mm is applied to the top right corner node, resulting in delamination of up to 0.08 mm along the interface. With the displacement load fixed, the topology optimization algorithm is iteratively applied. The detailed algorithmic implementation of FEM-TO is illustrated in Fig. 33. The resulting structural topology evolution of the substrate is shown in Fig. 35. In the second case, a total displacement load of 12 mm is applied, leading to a longer delamination of 0.2133 mm along the interface. The structural topology evolution of the substrate was recomputed and is displayed in Fig. 36. The different far-field total imposed displacements in cases 1 and 2 cause the non-linear response of the linearly graded cohesive interface properties to generate different stress fields and compliance values. Consequently, different optimized structural topology patterns emerge, as seen in Figs. 35 and 36 for the two test problems. Despite some local variations, the patterns are quite similar, suggesting that it is effective to design substrate topologies with localized densities to maximize the structure's stiffness and resist delam-

ination events.

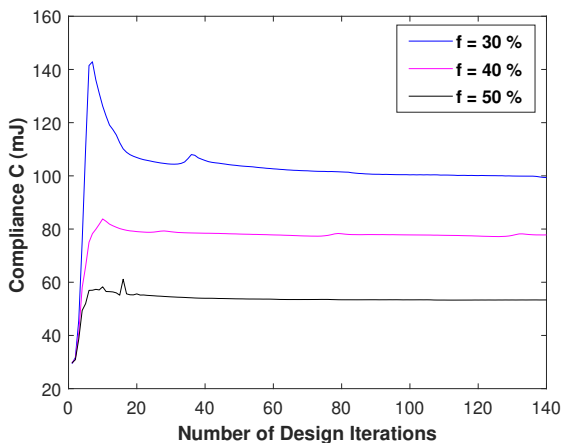


Figure 31: Comparison of compliance value with respect to number of design iterations for different volume fractions f .

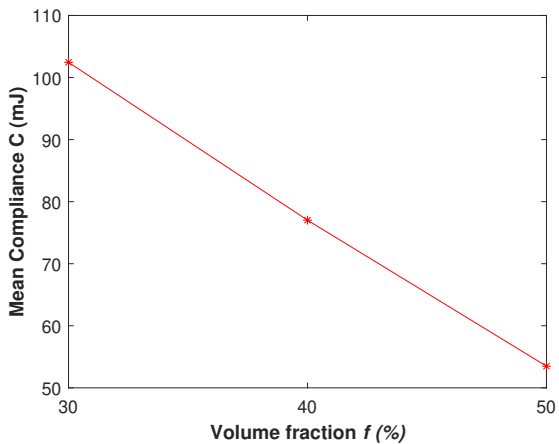


Figure 32: Trend showing mean compliance (C) as a function of volume fraction (f)

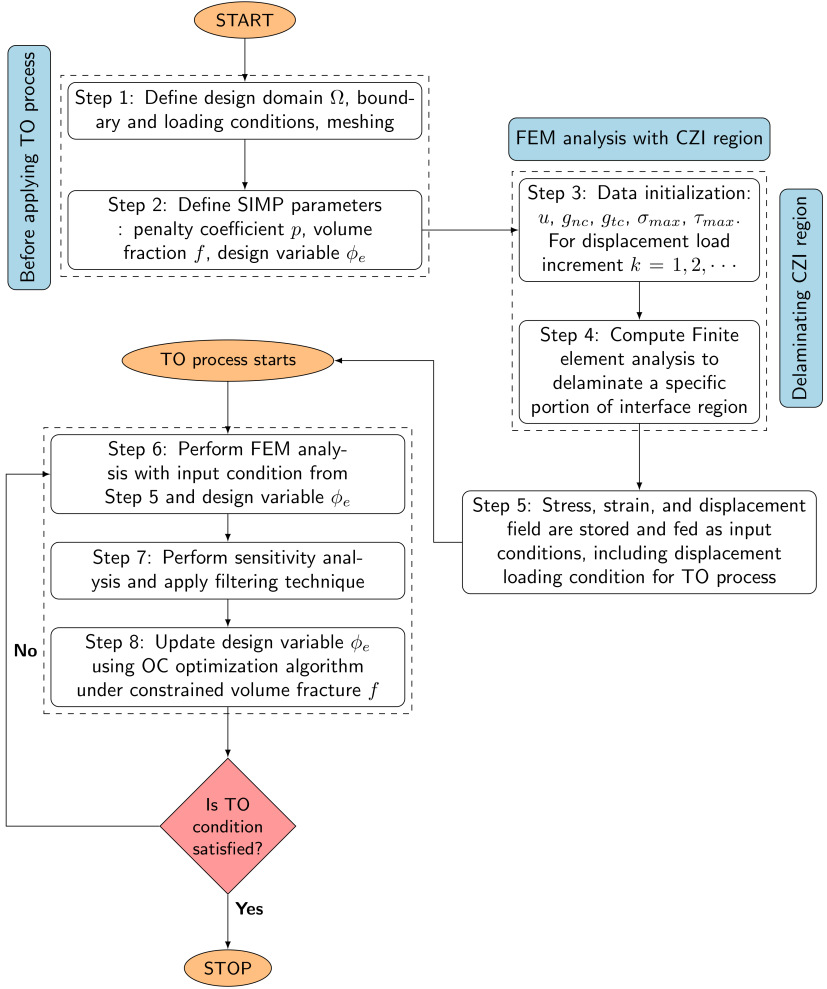


Figure 33: Flow chart showing combined FEM-TO algorithm for topology optimization of substrate in correspondence of different portions of initial delamination along the interface.

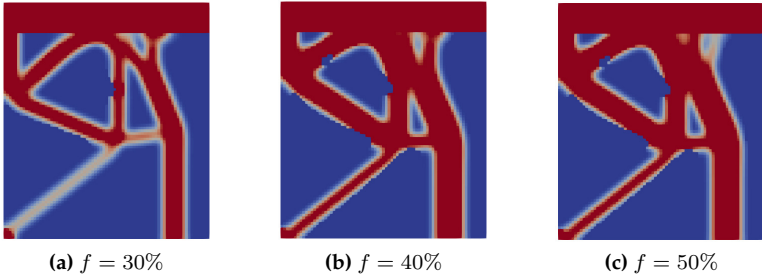


Figure 34: Optimized substrate topology for different volume fractions.

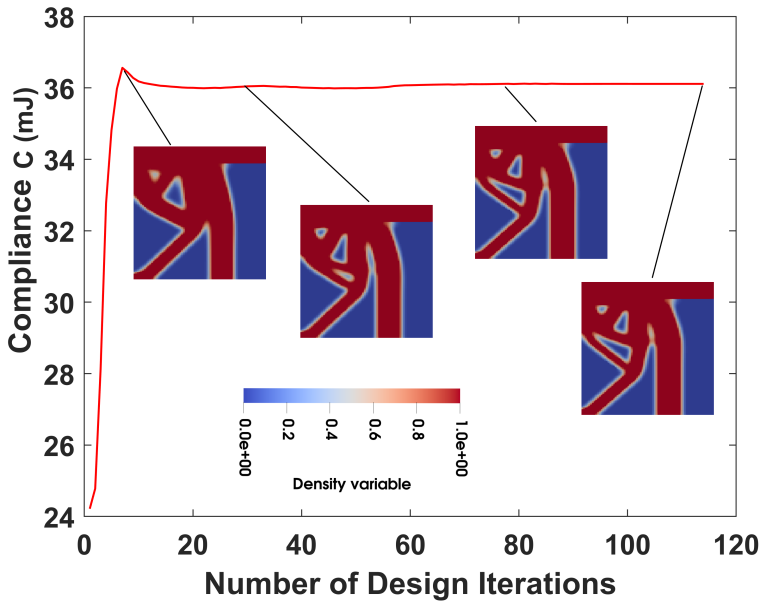


Figure 35: Structural topology evolution of the substrate for an interface with initial debonding of 0.08 mm.

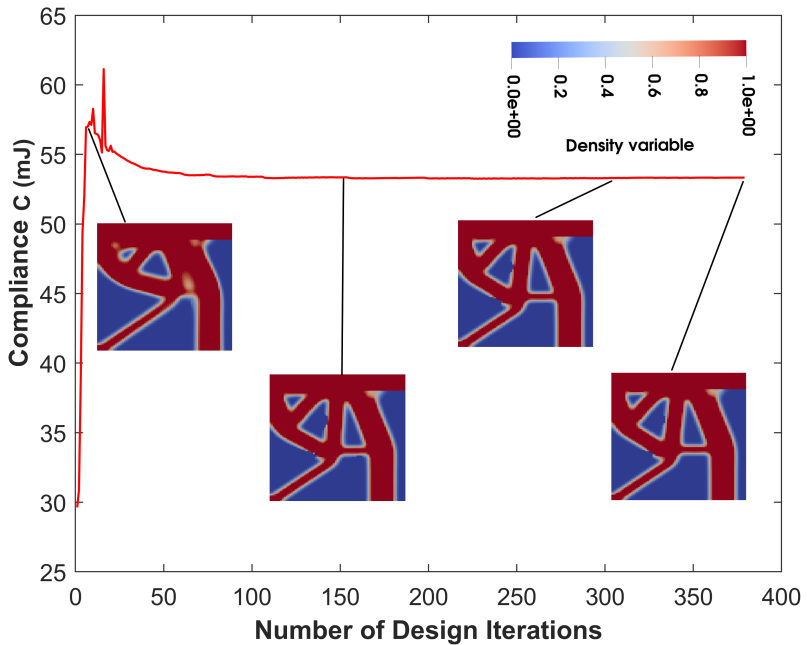


Figure 36: Structural topology evolution of the substrate for an interface with initial debonding of 0.2133 mm.

The current topology optimization framework has been extended to investigate L-shaped structural geometry similar to as mentioned in Fig. 29(a). The cohesive zone interface is located in between the vertical and horizontal sections, as shown in Fig. 37. In this study, the vertical section considered as the substrate to be optimized measures $0.5 \times 0.5 \text{ mm}^2$ and is meshed with 2500 elements. The horizontal section, a deformable region with dimensions $1 \times 0.3 \text{ mm}^2$, is meshed with 3000 elements, and a linear graded interface region of thickness 0.01mm is discretized with 50 elements. A vertical point load P , is applied at top right corner of the deformable region. For numerical analysis, the substrate, deformable, and linearly graded interface region properties are set the same as the previous peeling test problem.

Two cases were examined to study the topology evolution of the substrate under different far-field imposed displacements of 9 mm and 24 mm, respectively. The topology optimization process, as outlined in Fig. 33, was applied. Preliminary investigation reveals that volume fraction $f = 50\%$ is not able to provide a feasible optimized design structure. The material discontinuity in the substrate region makes it unsuitable to achieve the desired structural performance. Therefore, the volume fraction $f = 60\%$ is considered for analysis. The total displacement of 9 mm and 24 mm leads to delamination of 0.14 mm and 0.2 mm, respectively. Hence, the topology evolution and optimized substrate region pattern are different, as one can observe from Figs. 38 and 39, respectively.

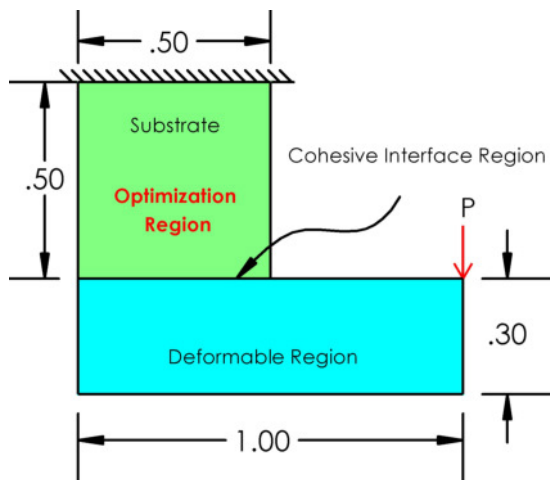


Figure 37: Sketch of L-shape structure with boundary condition and loading for a substrate with a delaminating interface, where the topology of the substrate has to be optimized to maximize the stiffness of the mechanical system for different levels of delamination.

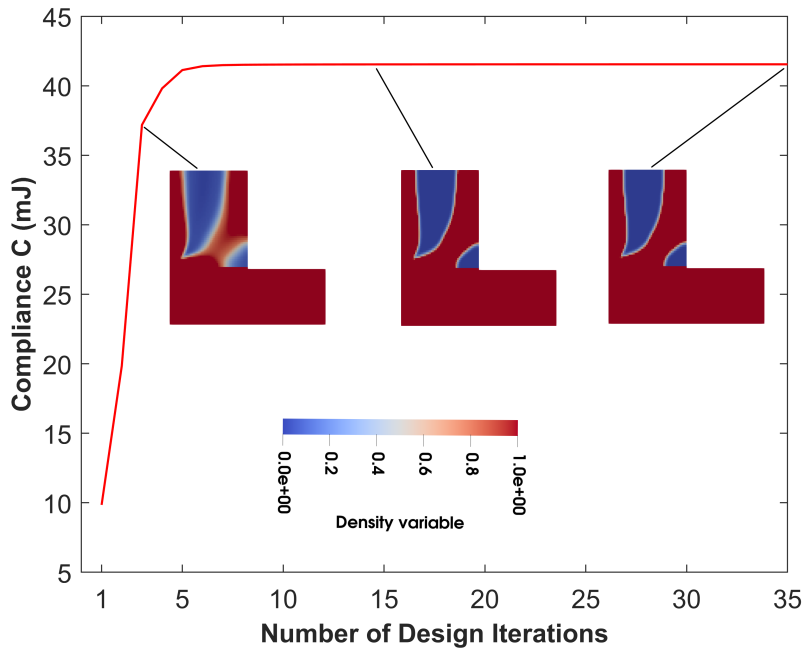


Figure 38: L-shape structural topology evolution of the substrate section for an interface with initial debonding of 0.14 mm.

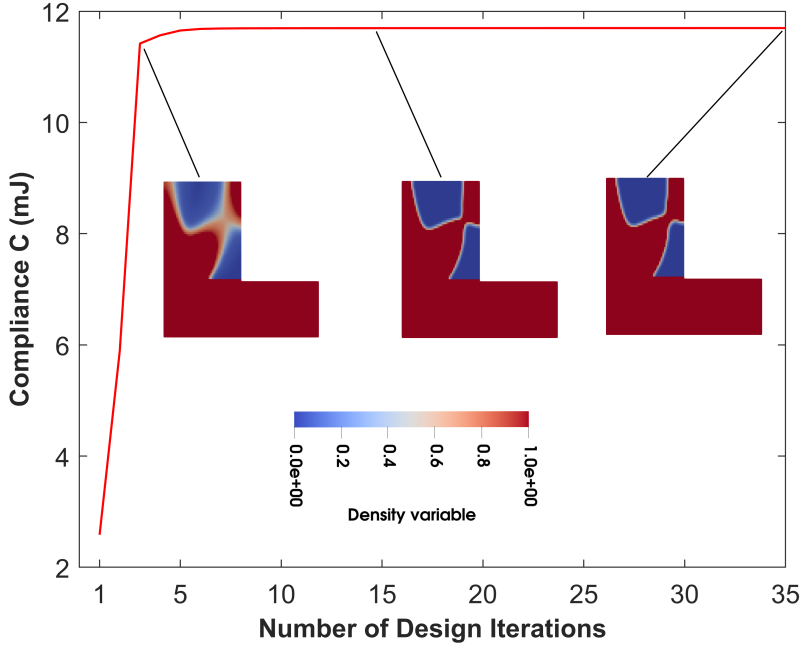


Figure 39: L-shape structural topology evolution of the substrate section for an interface with initial debonding of 0.2 mm.

4.3 Mathematical formulation for topology optimization applied to phase-field fracture

In this section, we address structures that have failed due to fracture and explore how to optimize these structures to resist fracture propagation. The phase-field for fracture is integrated with topology optimization, which optimizes material distribution within a given design space and allows for structural optimization with enhanced fracture resistance. Consider a design domain Ω discretized into N_e finite elements, and each element e is assigned a topology density variable ϕ_e . The density variable $\phi_e = 1$ corresponds to an inclusion phase, and $\phi_e = 0$ corresponds to the matrix phase. $\{\phi\} = \{\phi_1, \phi_2, \dots, \phi_{N_e}\}$ represents density values in the

finite element mesh domain with a range $\phi \in \{0 - 1\}$.

In the present work, we employ SIMP methodology considering two-phase material. The material interpolation follows.

$$\begin{cases} E_e = \phi_e^p E_{inc_e} + (1 - \phi_e^p) E_{mat_e}, \\ \psi_{c_e} = \phi_e^p \psi_{c,inc_e} + (1 - \phi_e^p) \psi_{c,mat_e} \end{cases} \quad (4.8)$$

where $\{E_{inc}, \psi_{c,inc}\}$, $\{E_{mat}, \psi_{c,mat}\}$ are {Young's modulus, fracture energy density} properties of inclusion and matrix phase respectively. p represents the penalty coefficient set value as 3 in SIMP methodology for convergence of ϕ to $\{0, 1\}$

Displacement loading condition is applied for structural stability. For the applied displacement load, the objective function is to maximize the mechanical work of the structure during the event of the fracture process. In mathematical formulation the total mechanical work $W_{\Delta \mathbf{u}}$ is approximated using trapezoidal rule

$$W_{\Delta \mathbf{u}} = \sum_{k=1}^{n_{load}} \Delta W^{(k)} \approx \frac{1}{2} \sum_{k=1}^{n_{load}} \left(\mathbf{f}_{ext}^{(k)} + \mathbf{f}_{ext}^{(k-1)} \right)^T \Delta \mathbf{u}^{(k)} \quad (4.9)$$

where n_{load} represents the number of displacement loading increments till failure of the structure, $\{\mathbf{f}_{ext}^{(k)}, \mathbf{f}_{ext}^{(k-1)}\}$ represents external nodal force vector which includes nodal reaction force, surface traction, and volume forces at the $\{(k)\text{-th}, (k-1)\text{-th}\}$ loading increment.

The optimization formulation in discretized form is given as

$$\begin{aligned} & \text{Maximize : } W_{\Delta \mathbf{u}}(\phi, \mathbf{u}, \phi) \\ & \text{subject : } \mathbf{K}_u^{(k)} \mathbf{u}^{(k)} - \mathbf{f}_u^{(k)} = \mathbf{0}, \quad k = 1, 2, \dots, n_{load} \\ & \quad \sum_{e=1}^{N_e} \phi_e v_e / \left(\sum_{e=1}^{N_e} v_e \right) = v^{inc} \\ & \quad 0 \leq \phi_e \leq 1, \quad e = 1, 2, \dots, N_e \\ & \quad \mathbf{u}^n \in \mathcal{S}_u, \quad n = 1, 2, \dots, k_{load} \\ & \quad \phi^n \in \mathcal{S}_\phi, \quad n = 1, 2, \dots, k_{load}, \end{aligned} \quad (4.10)$$

where v^{inc} represents target design inclusion volume. In this work, we employ a gradient-based optimization algorithm named the Optimal-

ity Criteria (OC) method. Sensitivity analysis is an important step in the topology evolution process, which is the change in objective function with respect to density variables. Here, we considered the methodology applied in [153].

4.4 Non linear system sensitivity analysis

The variation of the objective function with respect to the density variable using the adjoint method given as

$$W_{\Delta \mathbf{u}} \approx W^* = \frac{1}{2} \sum_{k=1}^{n_{\text{load}}} \{(\mathbf{f}_u^{(k)} + \mathbf{f}_u^{(k-1)})^T \Delta \mathbf{u}^{(k)} + (\mathcal{L}_1^{(k)})^T \mathbf{R}_u^{(k)} + (\mathcal{L}_2^{(k)})^T \mathbf{R}_u^{(k-1)}\} \quad (4.11)$$

$\mathcal{L}_1, \mathcal{L}_2$ are the lagrangian multiplier having the same dimensions as displacement vector \mathbf{u} , $\mathbf{R}_u^{(k)}$ and $\mathbf{R}_u^{(k-1)}$ are the mechanical residual (see Section 2.3) at (k)-th,(k-1)-th loading increment.

The displacement components at the prescribed nodes and the force components at the free nodes for the displacement-controlled loading problem are unaffected by the current value of ϕ . Here, we introduce the concept of essential (E) linked to Dirichlet boundary conditions and non-essential degrees of freedom (F) linked to free nodal values. Then we have a vector \mathbf{q} and a matrix \mathbf{Z} represented as

$$\mathbf{q} \sim \begin{bmatrix} \mathbf{q}_E \\ \mathbf{q}_F \end{bmatrix} \quad \mathbf{Z} \sim \begin{bmatrix} \mathbf{Z}_{EE} & \mathbf{Z}_{EF} \\ \mathbf{Z}_{FE} & \mathbf{Z}_{FF} \end{bmatrix} \quad (4.12)$$

With the above concept, the differentiation of displacement and force components with respect to ϕ at k-th load increment is given as

$$\begin{aligned} \frac{\partial \mathbf{u}^{(k)}}{\partial \phi_e} &= \begin{bmatrix} \mathbf{0} \\ \frac{\partial \mathbf{u}_F^{(k)}}{\partial \phi_e} \end{bmatrix}, & \frac{\partial \Delta \mathbf{u}^{(k)}}{\partial \phi_e} &= \begin{bmatrix} \mathbf{0} \\ \frac{\partial \Delta \mathbf{u}_F^{(k)}}{\partial \phi_e} \end{bmatrix}, \\ \mathbf{f}_u^{(k)} &= \begin{bmatrix} \mathbf{f}_{u,E}^{(k)} \\ \mathbf{0} \end{bmatrix}, & \frac{\partial \mathbf{f}_u^{(k)}}{\partial \phi_e} &= \begin{bmatrix} \frac{\partial \mathbf{f}_{u,E}^{(k)}}{\partial \phi_e} \\ \mathbf{0} \end{bmatrix} \end{aligned} \quad (4.13)$$

Therefore for arbitrary load increment indices $l, k = 1, 2, \dots, n_{load}$ we have

$$\begin{aligned} \frac{\partial}{\partial \phi_e} \left(\left(\mathbf{f}_u^{(l)} \right)^T \Delta \mathbf{u}^{(k)} \right) &= \left(\frac{\partial \mathbf{f}_u^{(l)}}{\partial \phi_e} \right)^T \Delta \mathbf{u}^{(k)} + \left(\mathbf{f}_u^{(k)} \right)^T \frac{\partial \Delta \mathbf{u}^{(k)}}{\partial \phi_e} \\ &= \left(\frac{\partial \mathbf{f}_u^{(l)}}{\partial \phi_e} \right)^T \Delta \mathbf{u}^{(k)} \end{aligned} \quad (4.14)$$

The derivative of the objective function W^* with respect to density variable ϕ is given as

$$\begin{aligned} \frac{\partial W^*}{\partial \phi_e} &= \frac{1}{2} \sum_{k=1}^{n_{load}} \left\{ \frac{\partial (\mathbf{f}_u^{(k)} + \mathbf{f}_u^{(k-1)})^T}{\partial \phi_e} \Delta \mathbf{u}^{(k)} \right. \\ &\quad \left. + (\mathcal{L}_1^{(k)})^T \frac{\partial \mathbf{R}^{(k)}}{\partial \phi_e} + (\mathcal{L}_2^{(k)})^T \frac{\partial \mathbf{R}^{(k-1)}}{\partial \phi_e} \right\} \end{aligned} \quad (4.15)$$

where residual force terms can be rewritten as

$$\frac{\partial \mathbf{R}^{(l)}}{\partial \phi_e} = \frac{\partial \mathbf{f}_u^{(l)}}{\partial \phi_e} - \frac{\partial \mathbf{K}_u^{(l)}}{\partial \phi_e} \mathbf{u}^{(l)} - \mathbf{K}_u^{(l)} \frac{\partial \mathbf{u}^{(l)}}{\partial \phi_e} \quad (4.16)$$

Therefore Eq. (4.15) can be reformulated as

$$\begin{aligned} \frac{\partial W^*}{\partial \phi_e} &= \frac{1}{2} \sum_{k=1}^{n_{load}} \left\{ \left(\frac{\partial \mathbf{f}_{u,E}^{(k)}}{\partial \phi_e} \right)^T (\Delta \mathbf{u}_E^{(k)} + \mathcal{L}_{1,E}^{(k)}) + \left(\frac{\partial \mathbf{f}_{u,E}^{(k-1)}}{\partial \phi_e} \right)^T (\Delta \mathbf{u}_E^{(k)} + \mathcal{L}_{2,E}^{(k)}) \right. \\ &\quad - (\mathcal{L}_1^{(k)})^T \left(\frac{\partial \mathbf{K}_u^{(k)}}{\partial \phi_e} \mathbf{u}^{(k)} + \mathbf{K}_u^{(k)} \frac{\partial \mathbf{u}^{(k)}}{\partial \phi_e} \right) \\ &\quad \left. - (\mathcal{L}_2^{(k)})^T \left(\frac{\partial \mathbf{K}_u^{(k-1)}}{\partial \phi_e} \mathbf{u}^{(k-1)} + \mathbf{K}_u^{(k-1)} \frac{\partial \mathbf{u}^{(k-1)}}{\partial \phi_e} \right) \right\} \end{aligned} \quad (4.17)$$

The important step is to choose Lagrangian multipliers $\mathcal{L}_1^{(k)}$, $\mathcal{L}_2^{(k)}$ carefully in order to eliminate implicit terms so that sensitivity of the objective function can be calculated explicitly. The first two terms of the

Eq. (4.17) can be eliminated by setting it as

$$\mathcal{L}_{1,E}^{(k)} = -\Delta \mathbf{u}_E^{(k)} \quad \text{and} \quad \mathcal{L}_{2,E}^{(k)} = -\Delta \mathbf{u}_E^{(k)} \quad (4.18)$$

Now the Eq. (4.18) can be re-written as

$$\begin{aligned} \frac{\partial W^*}{\partial \phi_e} = & -\frac{1}{2} \sum_{k=1}^{n_{\text{load}}} \left\{ \left(\mathcal{L}_1^{(k)} \right)^T \frac{\partial \mathbf{K}_u^n}{\partial \phi_e} \mathbf{u}^{(k)} + \left(\mathbf{K}_{u,FE}^{(k)} \mathcal{L}_{1,E}^{(k)} + \mathbf{K}_{u,FF}^{(k)} \mathcal{L}_{1,F}^{(k)} \right)^T \frac{\partial \mathbf{u}_F^{(k)}}{\partial \phi_e} \right. \\ & \left. + \left(\mathcal{L}_2^{(k)} \right)^T \frac{\partial \mathbf{K}_u^{(k-1)}}{\partial \phi_e} \mathbf{u}^{(k-1)} + \left(\mathbf{K}_{u,FE}^{(k-1)} \mathcal{L}_{2,E}^{(k)} + \mathbf{K}_{u,FE}^{(k-1)} \mathcal{L}_{2,F}^{(k)} \right)^T \frac{\partial \mathbf{u}_F^{(k-1)}}{\partial \phi_e} \right\} \end{aligned} \quad (4.19)$$

From Eq. (4.19) to eliminate the second and fourth terms of implicit in nature, we choose

$$\mathcal{L}_{1,F}^{(k)} = \left(\mathbf{K}_{u,FF}^n \right)^{-1} \mathbf{K}_{u,FE}^{(k)} \Delta \mathbf{u}_E^{(k)} \quad \text{and} \quad \mathcal{L}_{2,F}^{(k)} = \left(\mathbf{K}_{u,FF}^{(k-1)} \right)^{-1} \mathbf{K}_{u,FE}^{(k-1)} \Delta \mathbf{u}_E^{(k)} \quad (4.20)$$

Finally, using Eq. (4.18) and Eq. (4.20), the sensitivity of the objective function at the element level χ_e can be obtained as

$$\begin{aligned} \chi_e &= \frac{\partial W^*}{\partial \phi_e} \\ &= -\frac{1}{2} \sum_{k=1}^{n_{\text{load}}} \left\{ \left(\mathcal{L}_{1,e}^{(k)} \right)^T \frac{\partial \mathbf{k}_{u,e}^{(k)}}{\partial \phi_e} \mathbf{u}_e^{(k)} + \left(\mathcal{L}_{2,e}^{(k)} \right)^T \frac{\partial \mathbf{k}_{u,e}^{(k-1)}}{\partial \phi_e} \mathbf{u}_e^{(k-1)} \right\}, \quad (4.21) \\ &e = 1, \dots, N_e, \end{aligned}$$

in which $\frac{\partial \mathbf{k}_{u,e}^{(k)}}{\partial \phi_e}$ represents a change in elemental stiffness value concerning density variable at k-th load increment. The detailed procedure of execution of the problem is explained in Algorithm.4

The topology optimization process suffers from check-board pattern, mesh dependency, singularity phenomenon, jagged edges, local stress constraints, and grey regions in the structural elements. To overcome these issues partially or fully cone-shaped density filtering scheme proposed in Section 4.1.1 is implemented.

Algorithm 4 Topology optimization of fracture problems

```
1: Input : Density vector  $\Phi^k$ ,  $i=1$ 
2: while Err > Tol do
3:   Data initialization  $\mathbf{u}_0, \Phi_0$  and  $\mathcal{H}_0$  at time  $t_0$  are known
4:   for all time incremental steps  $k = 1, \dots, n_{load}$ : starts at  $k = 1$  do
5:      $t_k \leftarrow t_0 + \Delta t$  ( $\Delta t$  :small time increment)
6:     Step 1: Compute  $\mathbf{K}_u$  from Eq. (2.41)
7:     Compute displacement field  $\mathbf{u}_{t_i}^k$  from Eq. (2.40)
8:     Step 2: Compute  $\mathbf{K}_\Phi$  from Eq. (2.44)
9:     Compute maximum strain energy  $\mathcal{H}_{\max}$  at each gauss points
       from Eq. (2.34)
10:    Computer phase-field  $\Phi_{t_i}^k$  from Eq. (2.43)
11:     $\mathbf{u}_0 \leftarrow \mathbf{u}_{t_i}^k, \phi_0 \leftarrow \phi_{t_i}^k$ 
12:     $k \leftarrow k+1, t_o \leftarrow t_i$ 
13:    Compute incremental sensitivity Calculation  $\chi^{t_k}$  and incremen-
       tal mechanical work  $W^{t_k}$ 
14:  end for
15:  Output :  $\chi^k = \chi^{n_{load}}$  and  $W^k = W^{n_{load}}$ 
16:  Filtering scheme
17:  Optimality criteria method
18:  if  $i > 10$  then
19:     $Err = \frac{|\sum_{m=i-4}^i W^m - \sum_{n=i-9}^{i-5} W^n|}{\sum_{n=i-9}^{i-5} W^n}$ 
20:  else
21:    Err=1
22:  end if
23:   $i \leftarrow i+1$ 
24: end while
```

Now, we introduce a novel framework that integrates structural TO with fracture simulations using PFF. This approach determines the optimal topology for structures with initial damage, a scenario not previously addressed in existing literature [160, 152, 156, 153, 157] e.t.c to name a few. For example, consider a scenario where the phase-field method is applied to an undamaged structure under a specific load, termed the service load—to test the structure’s response, potentially inducing minor initial damage. Following this, topology optimization is employed on the now-damaged structure to determine the optimal distribution of

materials to mitigate the initial damage or crack effects. Typically, the algorithm is expected to suggest reinforcements around the defect or crack to fortify it. This process necessitates clearly explaining the optimization objectives and conditions, such as maximizing stiffness with the same material quantity or achieving the same stiffness with less material. Beyond the standard response maximization through topology optimization, conducting a phase-field simulation on the optimized structure is beneficial in evaluating its behavior and determining if the new internal arrangement of materials can prevent or slow down crack propagation. This combined approach first triggers initial damage in the structure using PFF optimizes the configuration to reinforce it near the crack zone with the help of TO and subsequently evaluates its enhanced fracture resistance. The detailed procedure of the proposed approach is mentioned in Fig. 52 for full implementation in the PFF-TO regime.

4.5 Examples

This section analyzes three benchmark test problems to show the robustness of the proposed PFF-TO formulation outlined in Fig. 52. In all the numerical examples considered, quadrilateral bi-linear finite elements are chosen with plain strain assumption. 2D CAD models are prepared in the Gmsh software [203]. In test problems, we examine composite structures composed of matrix and inclusion phases. We aim to determine the optimal shape of the inclusion material during the TO process, maximizing fracture resistance across the entire structure. The inclusion volume fraction (v^{inc}) remains constant throughout the TO process. The material properties of both the matrix and inclusion phases are consistent across all test cases, as detailed in Table. 4. The proposed PFF-TO formulation is coded in Matlab-based FEM software [186]. Finally, result analysis is carried out in the Paraview platform [204], an open-source scientific visualization software best suited for post-processing work.

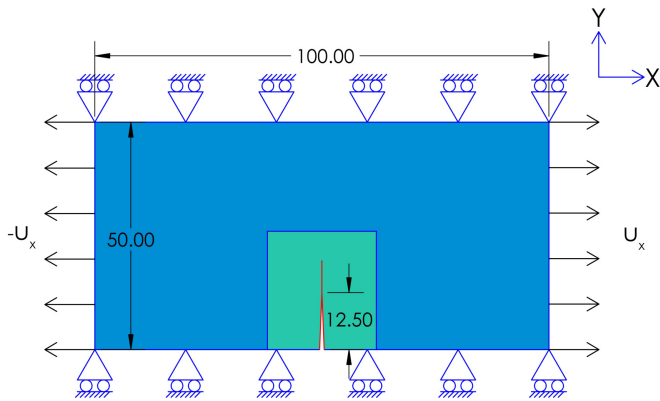
Phase material	Young's modulus E (MPa)	Poission's ratio ν	Critical fracture strength σ_c (MPa)
Inclusion	52000	0.3	30
Matrix	10500	0.3	10

Table 4: Material properties of the matrix and inclusion phase during numerical simulations

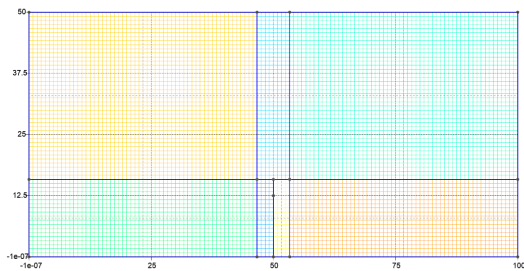
A rectangular composite plate measuring $100 \times 50 \text{ mm}^2$ is analyzed, featuring a pre-existing notch with a width of 0.01 mm. The domain is discretized into a grid of 120×60 square finite elements. Fig. 40(a),(b) provides an illustration of the geometric configuration, boundary conditions, and meshing arrangement pertinent to the test problem scenario. The phase-field model characteristic length scale parameter (l_c) and filtered radius (r_{min}), both set to twice the length of the finite elements (h_e), denoted as $l_c = r_{min} = 2 h_e$. Boundary conditions entail constraining the plate's top and bottom edges along the y-direction while the left and right edges undergo prescribed horizontal displacements. Initially, a displacement increment (ΔU) of 0.004 mm is applied for the first five load increments, followed by a reduced increment of 0.001 mm for subsequent increments until plate failure. Dirichlet boundary conditions are prescribed at nodes along the pre-existing notch, setting the phase-field variable (Φ) to 1.

The investigation focuses on the structured problem, considered to be an initially damaged structure. Given the pre-existing fracture, the material properties exhibit non-homogeneity across the structure's region. Our objective is to conduct topology optimization for damaged structures, with a primary emphasis on fracture resistance. Initially, a displacement loading increment of 0.022 mm is applied to induce damage within the material, as illustrated in Fig. 40(a). Subsequently, a topology optimization algorithm is employed to facilitate the evolution of the structure's topology. The convergence criterion for optimality is set at a tolerance error of 10^{-5} to terminate the iterative optimization process. To maintain the integrity of the optimization process and not interfere with sensitivity analysis, particular attention is paid to the region proximal to the fractured surface. We ensure this by selecting a cluster of nodes near the fractured area, encompassing all nodes at a reasonable distance from

the fractured surface. This constraint is enforced by designating the design variable $\phi = 1$ (representing the matrix material) in Fig. 40, depicted in green.



(a) Test model 1 with damage



(b) Finite element mesh

Figure 40: Geometry, boundary conditions and meshing details of already fractured composite plate subjected to incremental traction load along x -direction

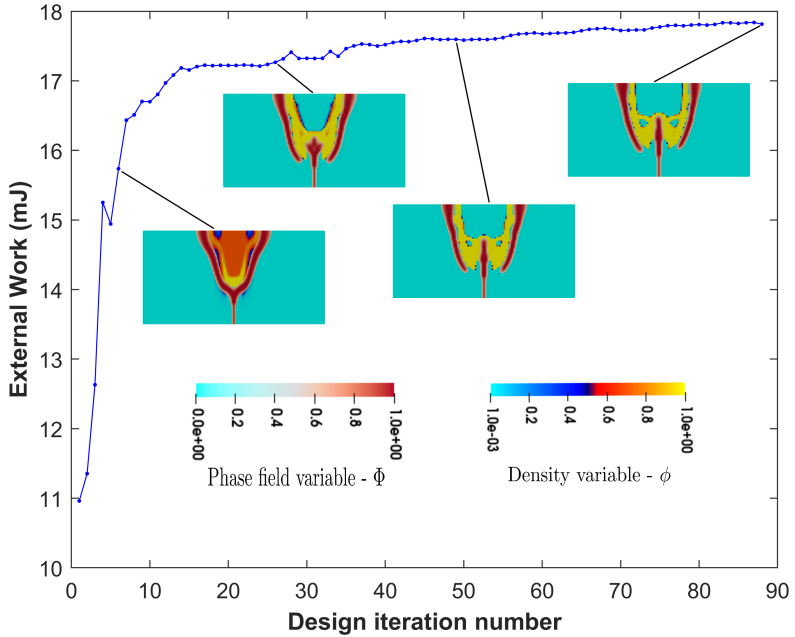


Figure 41: Topology evolution of inclusion region ($v^{inc} = 10\%$) and respective crack pattern for induced damaged structure of test problem 1

The target volume fraction for the inclusion phase region is established at 10%. Fig. 41 illustrates the progressive evolution of the inclusion topology region alongside the corresponding crack patterns throughout the optimization process. Notably, the emergence of inclusion material initiates from the fractured tip and gradually accumulates along the path of the crack from preceding design iterations. Eventually, the evolution of the inclusion material within the structure culminates in an optimal state, achieving a value of 17.81 mJ, surpassing the initial design objective value of 10.96 mJ as one can observe in Fig. 41. The crack propagation and fracture resistance of the initial and final optimized design are depicted in Fig. 43. In the analysis of crack evolution, the crack initiates from the tip of the initial fracture during the displacement loading phase.

Subsequently, it bifurcates into two branches around the left and right corners of the inclusion pattern region, extending until structural failure occurs. Fig. 42 presents the relationship between reaction force and imposed displacements for the initial and final optimized design structures for specified volume fraction ($v^{inc} = 10\%$). The optimized design demonstrates a notable increase of 58.15% in peak load before fracture and a corresponding 67.3% enhancement in toughness value compared to the initial design structure.

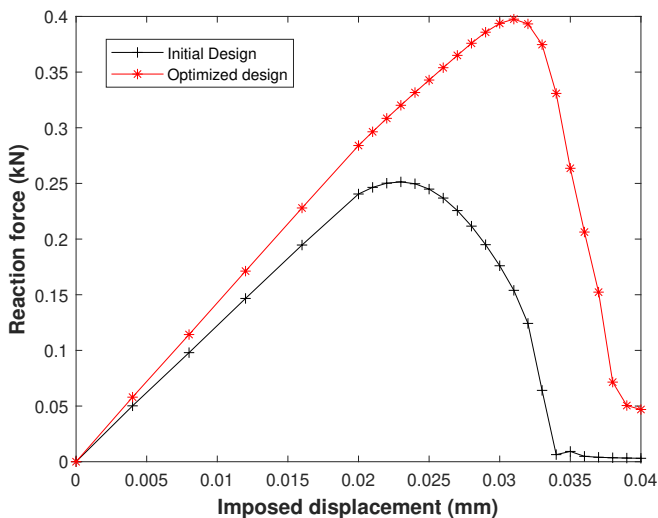
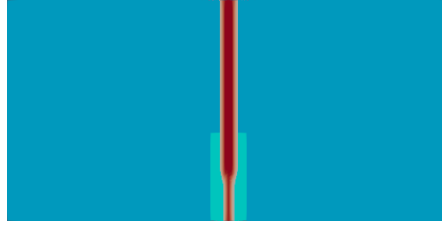
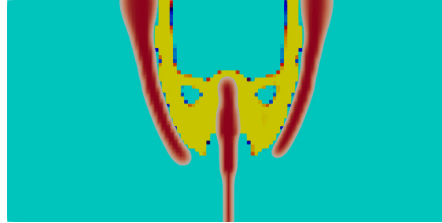


Figure 42: Reaction force-displacement curve of the already fractured structure for the initial and final optimized design ($v^{inc} = 10\%$) for test problem

1



(a) Initial design



(b) Final design

Figure 43: Fracture resistance and crack growth of the initial design and final optimized inclusion phase design ($v^{inc} = 10\%$) of test problem 1

The numerical setup for test problem 2 involves a 2D plate containing a singular pre-existing crack notch of width 0.1 mm at the center on the left side of the plate, as illustrated in Fig. 44(a). The plate dimensions are $50 \times 100 \text{ mm}^2$. It is uniformly discretized into 60×120 square-shaped bilinear elements (see Fig. 44(b)). The lower end of the plate is constrained vertically and free horizontally, while the left bottom corner node is fixed in both directions to prevent rigid body motions. Incremental displacement loads are applied at the upper end of the plate, with an initial displacement of 0.01 mm for the first five load increments, followed by 0.0025 mm for subsequent increments. Loading continues until the reaction force falls below a predetermined threshold, indicating complete structural failure.

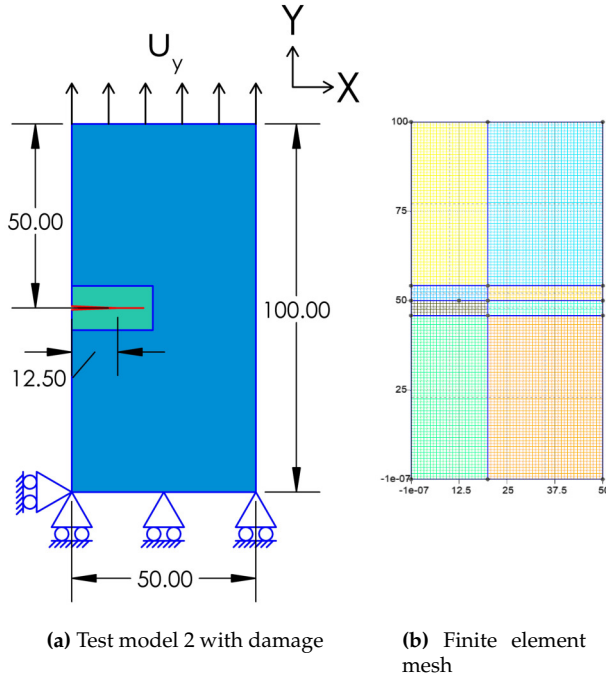


Figure 44: Geometry, boundary conditions and meshing details of already fractured plate subjected to incremental normal load along y-direction

Dirichlet conditions are enforced on the crack phase-field to emulate the presence of a pre-existing crack notch, maintaining a prescribed value ($\Phi = 1$) along the crack. Initially, the structure undergoes damage, as illustrated in Fig. 44(a), induced by an applied displacement loading increment of 0.0525 mm. This step is undertaken further to investigate the fracture resistance within the damaged composite structure utilizing the Topology Optimization (TO) procedure. The vicinity surrounding the initial induced damage is designated as a non-designable area to prevent the inadvertent inclusion of material within the pre-existing fracture region. This precautionary measure ensures the exclusion of irrelevant optimized designs. The selection of an appropriate region sufficiently distant from the fracture surface is crucial to avoid undue influence on the

sensitivity analysis of the objective function during the optimization process. This is achieved by confining the region with the design variable $\phi = 1$ (representing the matrix material) in Fig. 44(a), indicated in green.

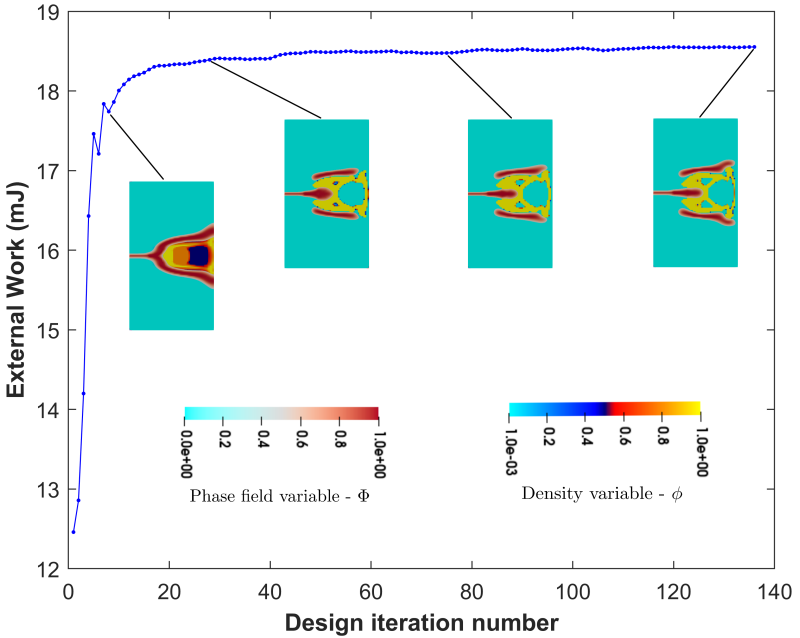


Figure 45: Topology evolution of inclusion region ($v^{inc} = 10\%$) and respective crack pattern for a predefined matrix region of test problem 2

The evolution of inclusion typologies, final crack patterns, and the history of the design objective value (mJ) is illustrated in Fig. 45. The results demonstrate a gradual enhancement in the fracture resistance of the composite structure in tandem with the associated crack propagation patterns during the optimization process. Regarding the discussion on crack evolution, the crack commences from the tip of the initial fracture region during the displacement loading phase. It then divides into two branches around the upper and lower corners of the inclusion pattern region, extending until structural failure becomes evident during the op-

timization iteration process, as illustrated in Fig. 45. Fracture resistance between the optimally designed composite structure and the initial design is compared through a comprehensive fracture simulation for both cases, as illustrated in Fig. 47. Notably, Fig. 46, which represents the reaction force-displacement plot of an initial and optimal structure design, indicates a substantial increase of 70.94% in fracture toughness and 47.61% in peak force. Moreover, the design objective values for the initial and final optimized designs are determined to be 12.46 mJ and 18.56 mJ, respectively, as depicted in Fig. 45.

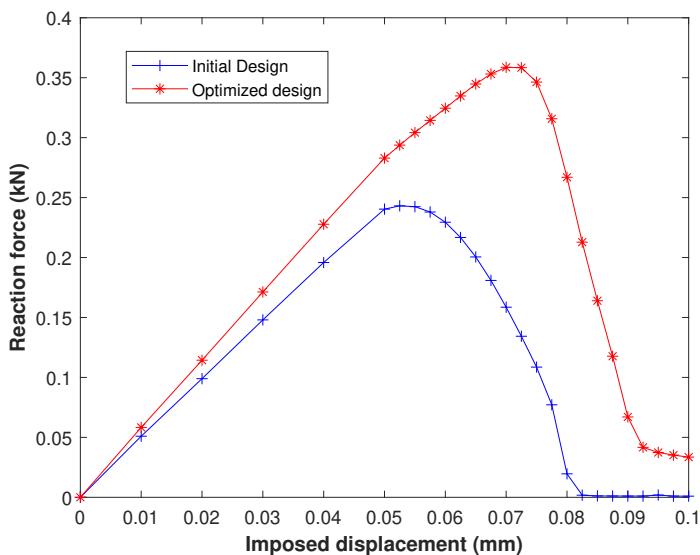


Figure 46: Reaction force-displacement curve of the already fractured structure for the initial and final optimized design ($v^{inc} = 10\%$) of test problem 2

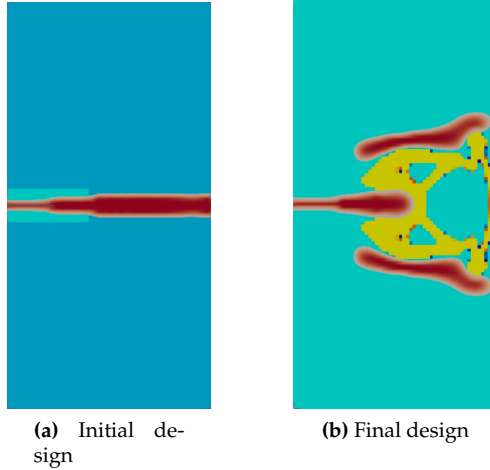


Figure 47: Fracture resistance and crack growth of the initial design and final optimized inclusion phase design ($v^{inc} = 10\%$) of test problem 2

The numerical setup for test problem 3 involves a 2D plate with two pre-existing crack notches of width 0.1 mm at the left and right sides of the plate. The plate, with dimensions of 50×100 mm, is uniformly divided into 60×120 square-shaped bilinear elements (Fig. 48(b)) with the position of the notch, boundary, and loading conditions shown in Fig. 48(a). Its lower end is constrained vertically and free horizontally, while the left bottom corner node is fixed in both directions to prevent rigid body motions. Incremental displacement loads are applied at the upper end of the plate, beginning with an initial displacement of 0.01 mm for the first five load increments, followed by 0.005 mm for subsequent increments. Loading persists until the reaction force diminishes below a predetermined threshold, indicating full structural failure.

Dirichlet conditions are imposed on the crack phase-field to simulate the presence of a pre-existing crack notch, maintaining a prescribed value ($\Phi = 1$) along both cracks. Initially, the structure experiences damage (see Fig. 48(a)) induced by an applied displacement loading increment of 0.055 mm. This step is taken to investigate the fracture resistance within

the damaged composite structure using the Topology Optimization (TO) procedure. To prevent the inadvertent inclusion of material within the pre-existing fracture region, the vicinity surrounding the initial induced damage is designated as a non-designable area. This precaution ensures the exclusion of irrelevant optimized designs. Selecting an appropriate region at a sufficient distance from the fracture area is crucial to avoid interfering with the calculation of sensitivity analysis during the optimization process. This is accomplished by confining the region with the design variable $\phi = 1$ (representing the matrix material), as shown in green in Fig. 48(a).

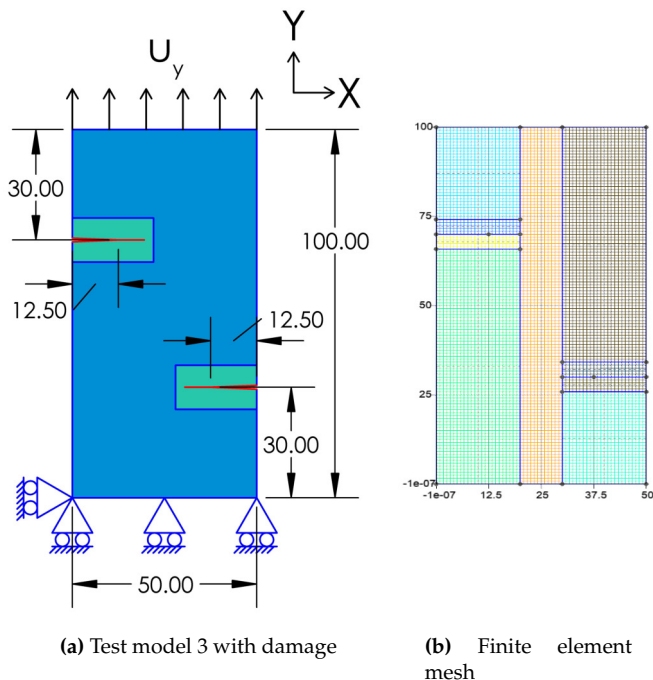


Figure 48: Geometry, boundary conditions and meshing details of already fractured plate subjected to incremental normal load along y-direction

Fig. 50 illustrates the progression of inclusion types alongside their

eventual crack patterns and the history of design objectives. Similar to the previous test problems, the composite structure's fracture resistance gradually improved with increase in fracture toughness, peak force to 46.6 %, 19.18% respectively compared to initial design as depicted in Fig. 50. Additionally, the design objective values for the initial and final optimized designs are established as 9.64 mJ and 14.5 mJ, respectively, as shown in Fig. 50. Due to the placement of cracks on opposite sides of the plate, cracks manifest in an anti-symmetric fashion towards the left and right sections of the structure. Fig. 51 depicts the propagation of cracks through the initial and optimum design of the inclusion phase of the composite structure. The crack propagation through the inclusion region might be due to two cracks placed on opposite sides of the plate.

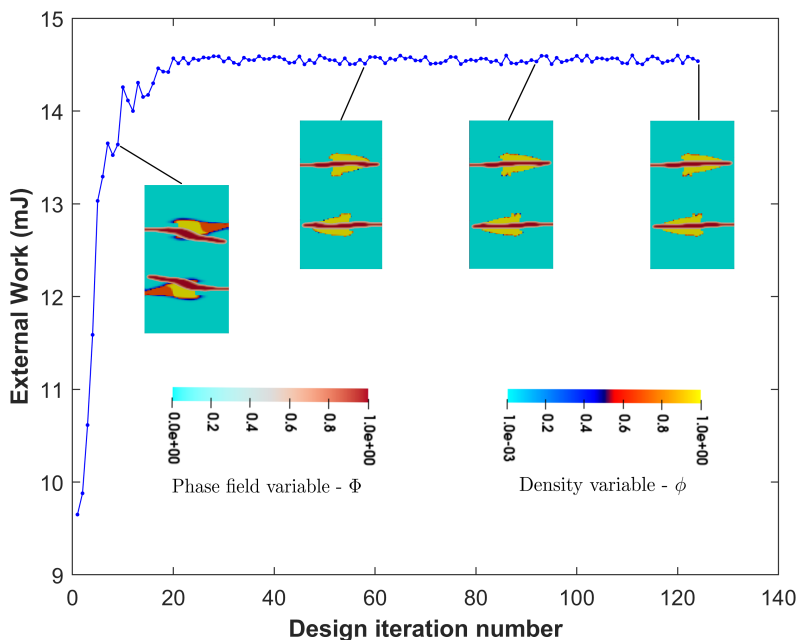


Figure 49: Topology evolution of inclusion region ($v^{inc} = 10\%$) and respective crack pattern for induced damaged structure of test problem 3

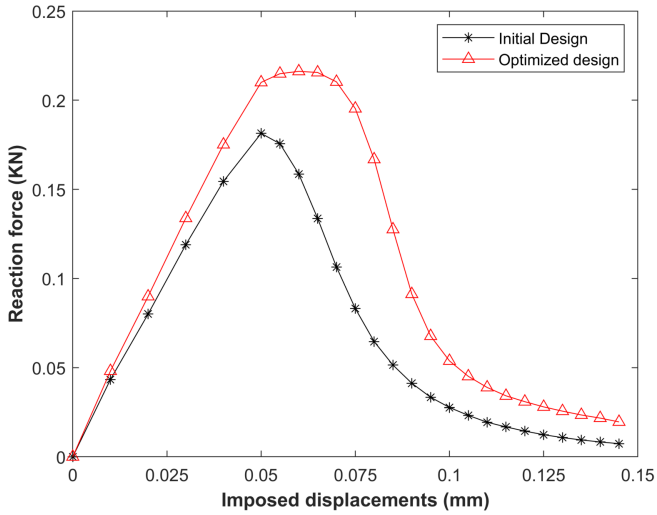


Figure 50: Reaction force-displacement curve of the already fractured structure for the initial and final optimized design of test problem 3 ($v^{inc} = 10\%$)

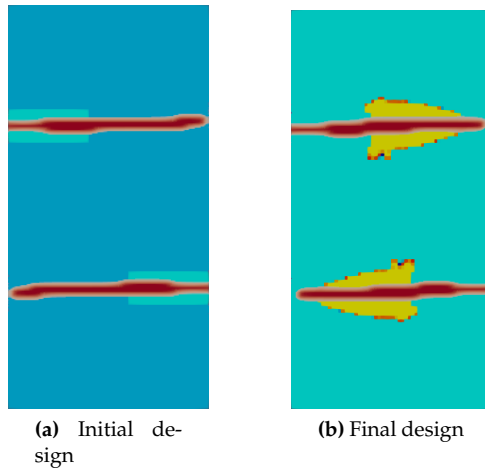


Figure 51: Fracture resistance and crack growth of the initial design and final optimized inclusion phase design ($v^{inc} = 10\%$) concern test problem 3

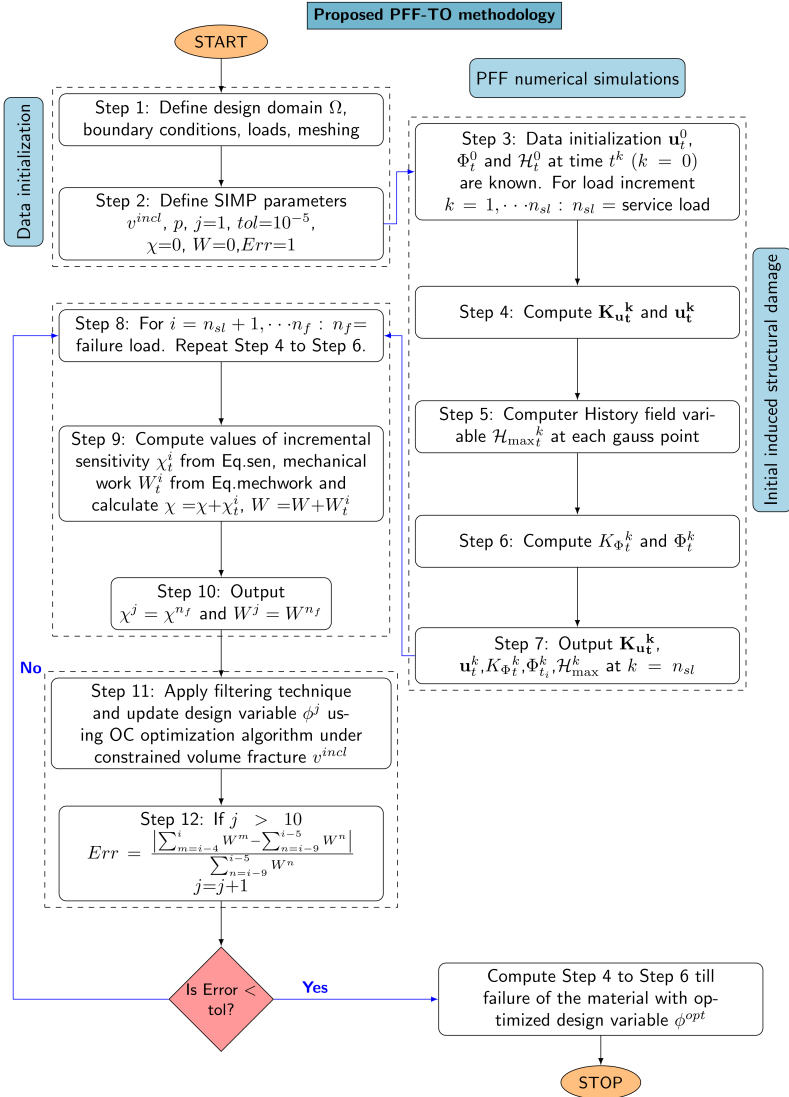


Figure 52: Flow chart showing combined PFF-TO algorithm for topology optimization of initial damaged structures to enhance crack resistance.

Chapter 5

Machine learning applied to polymer materials

Chapter 5 is partially based on the content of the publication [1].

Applying the particle swarm optimization (PSO) algorithm, a machine learning technique to the identification of material properties in polymer materials, represents an advanced computational approach to solving inverse problems. In the context of polymers, PSO can be utilized to infer intrinsic material properties—such as modulus of elasticity, yield strength, maximum load, etc.— from experimental data, like stress-strain responses or load-displacement results. By iteratively adjusting the positions of the particles towards the optimal solution, PSO effectively tackles the complex, nonlinear relationships between observed data and material properties. This method enhances the accuracy of predictions and minimizes the need for extensive physical testing, facilitating the efficient design and optimization of polymer materials with desired properties. Consequently, PSO provides a powerful tool for researchers and engineers to develop advanced polymer-based materials tailored for specific applications using additive manufacturing technology applied to automotive, aerospace, and biomedical industries. The Chapter mainly focuses on examining in detail the critical parameters of PFF models, such as the internal length scale parameter l_c in the isotropic case and the penalty parameter β in the anisotropic, which are sensitive to numerical results when subjected to different geometry, loading and

boundary conditions.

5.1 Application to ABS co-polymer

The robustness of the PSO algorithm applied to the identification of fracture mechanics parameters is herein assessed in relation to experimental results of ABS co-polymer material subjected to tensile and three-point bending loading conditions. A series of uni-axial and three-point bending experimental tests was carried out using the universal testing machine Zwick/Roell Z010TH available in the experimental laboratory of the Multi-scale Analysis of Materials Research Unit at IMT Lucca. The scatter in the experimental curves shown in Figs. 54(a) and 57(a) is due to the typical effect induced by a slight variation in the amount of additives used to reduce swelling in ABS materials for injection moulding [205].

The PF formulation based on the AT-2 model proposed in Chapter2 has been applied to simulate the corresponding tests, and coupled with the PSO algorithm, parameter identification has been performed. All the routines are coded in MATLAB, release 2020b. Young's modulus E , fracture parameters G_c (fracture energy), and l_c (internal length scale) were chosen as PSO swarm particle parameters to be identified. The range of ABS properties to conduct PSO-PF simulations were taken from literature: tensile strength $\sigma_{\max} \in \{22, 49\}$ MPa, $E \in \{1100, 2900\}$ MPa, Poisson's ratio $\nu = 0.37$ and fracture toughness $K_{IC} \in \{1.2, 4.2\}$ MPa \sqrt{m} . Exploiting the correlations $G_c = \frac{K_{IC}^2(1-\nu^2)}{E}$ and $l_c = \frac{27}{256} \frac{G_c E}{(1-\nu^2)\sigma_{\max}^2}$, we derived the following range of variability for $G_c \in \{1.25, 13.8\}$ N/mm and $l_c \in \{0.25, 3.8\}$ mm.

5.1.1 Uni-axial tensile tests

Experimental tests were conducted and repeated 15 times on specimens of ABS material under uni-axial tensile loading conditions as per ASTM D638[53] standards. The specimen geometry is length \times width \times thickness = 114 \times 10.2 \times 4.5 mm and boundary conditions are depicted in Fig.

53. Stress-strain curves are shown in Fig. 54(a). PF numerical simulations have been performed by replicating the experimental conditions (see Fig. 53) with a Dirichlet boundary condition $\Phi = 0$ [177, 206] imposed on the phase-field at both ends of the tensile test model.

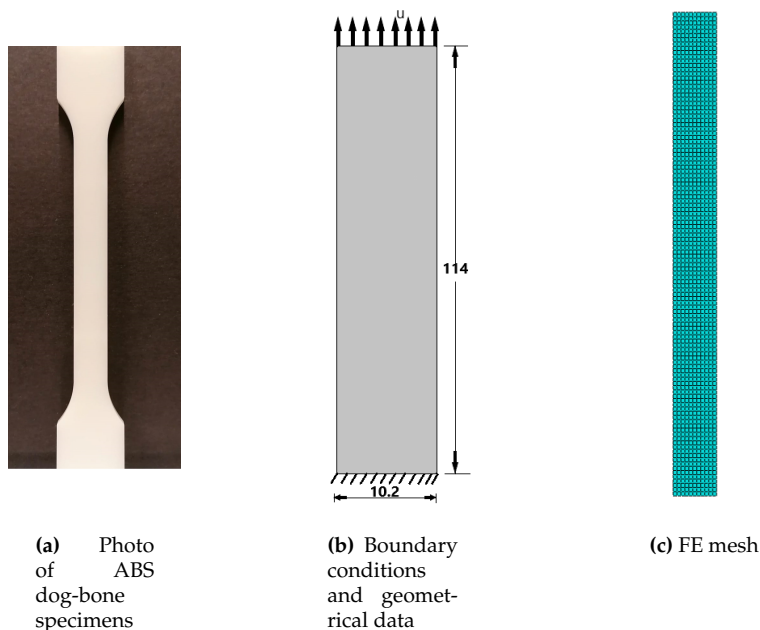


Figure 53: Photo of the specimen, dimensions and boundary conditions, FE mesh.

Since uni-axial tensile tests are not suitable for fracture mechanics characterization, we set an average value of $G_C = 7.5$ N/mm taken from the literature for all the 15 numerical simulations, and we identify the parameters E and l_c which influence the initial linear elastic regime of the stress-strain curves and the material tensile strength (computed from the peak load value before specimen failure). Therefore, the PF-PSO simulations are conducted with swarm particles in the parameter space (E, l_c) , with admissible range for $E \in \{1100, 2900\}$ MPa and for $l_c \in \{0.25, 3.8\}$

mm. Fig. 54(b) shows the optimal PSO-PF response of the 15 stress-strain curves that minimize the error from the experimental ones. Table. 5 collects the PSO-identified parameters for the 15 tests. From this analysis, considering the mean values and the standard deviations, the identified Young modulus corresponds to $\bar{E} \pm \sigma_E = 1157.904.01 \pm 34.8223$ MPa, and the internal length scale $\bar{l}_c \pm \sigma_{l_c} = 1.3361 \pm 0.0408$ mm.

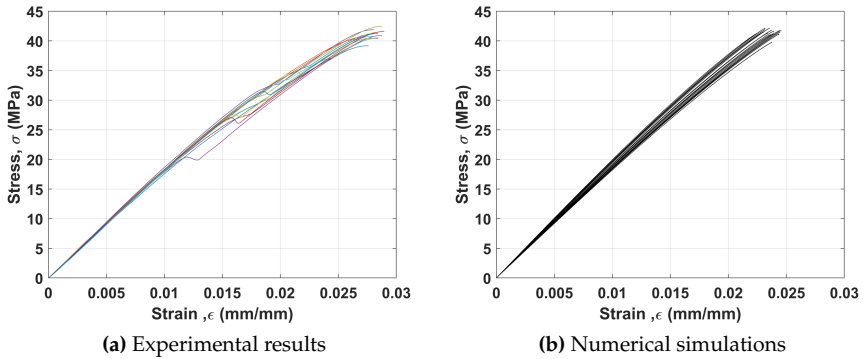


Figure 54: Experimental and numerical simulation results identified (corresponding to the identified model parameters).

5.1.2 Three-point bending tests

Three-point bending tests with notched samples are now considered since they can also be exploited for fracture mechanics characterization, and therefore, it is possible to apply the PSO algorithm combined with the PF simulation framework to identify all the three model parameters, E , l_c and G_{cr} , and critically compare the outcome with the results of the previous parameters' identification concerning uni-axial tensile tests.

Experimental tests were conducted on a set of ABS specimens with an initial sharp V-notch under the three-point bending loading as per ASTM D5045-14[55] standards, see Figs. 55(a) and (b), showing the initially undeformed configuration and the specimen at failure, with the formation of crazing at the notch tip which is highlighted by the change of color of

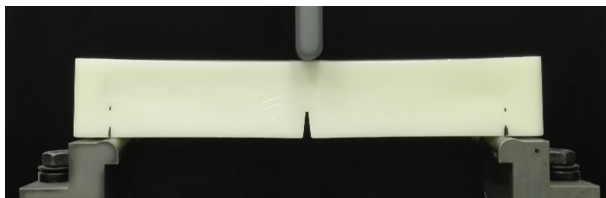
Test #	E (MPa)	l_c (mm)
1	1130.39	1.281
2	1116.48	1.306
3	1215.08	1.415
4	1197.61	1.362
5	1183.24	1.3201
6	1169.185	1.359
7	1120.501	1.29
8	1164.818	1.321
9	1123.67	1.273
10	1141.05	1.33
11	1107.73	1.3917
12	1193.6	1.376
13	1152.43	1.318
14	1203.6	1.3472
15	1149.186	1.3508
Mean	1157.904	1.3361
Std. dev.	34.8223	0.0408

Table 5: PSO identified E and l_c parameters for the 15 tests in Fig. 54, with their mean and standard deviation values.

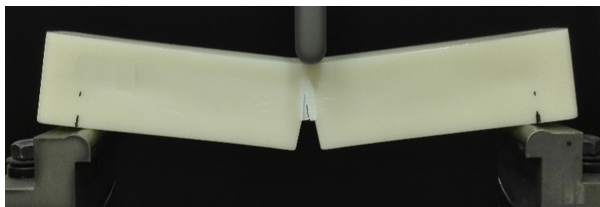
ABS from yellow to white, due to the stretching of the polymeric fibers during crack growth. The spread of crazing in the direction orthogonal to the mid-span cross-section is quite consistent and it certainly represents a zone of diffuse damage that could be simulated using the phase-field approach to fracture with a finite -not vanishing- internal length scale l_c . As compared to PMMA investigated in [25], ABS is, therefore, much less brittle.

The geometrical data are shown in Fig. 55(c) and a FE mesh with linear quadrilater finite elements with a fine discretization near the mid cross-section and a coarser one far from the perspective crack path has been used, see Fig. 55(d). A preliminary mesh sensitivity analysis has been performed for the PF simulations, considering 1614, 7076, or 13984 four-noded quadrilateral finite elements using different degrees of refinement of the mesh far from the mid-cross-section. Provided that the mid-cross-section is properly discretized, the numerical predictions were

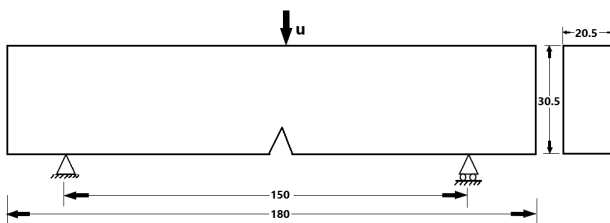
almost unaffected (see Fig. 56), and the discretization consisting in 1614 FE has been considered for the parameter identification issue to speed up computation time.



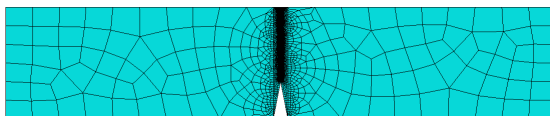
(a) Undeformed specimen



(b) Deformed specimen at failure



(c) Geometry and boundary conditions (measures in mm)



(d) FE model

Figure 55: Experiment specimen and geometrical details (in mm), loading, boundary condition, meshing details of a numerical model for three-point bending loading case

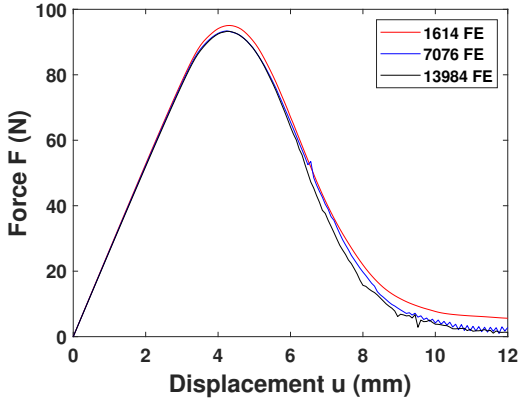


Figure 56: Mesh convergence study for 3pt bending PF simulation.

Force vs. mid-span displacement curves for the 15 tests are shown in Fig. 57, comparing the experimental curves (left panel) with the results of the numerical simulations (right panel) corresponding to the identified best model parameters by the PSO algorithm. Again, the following range of values has been considered for $E \in \{1100, 2900\}$ MPa, $G_c \in \{1.25, 13.8\}$ N/mm, $l_c \in \{0.25, 3.8\}$ mm.

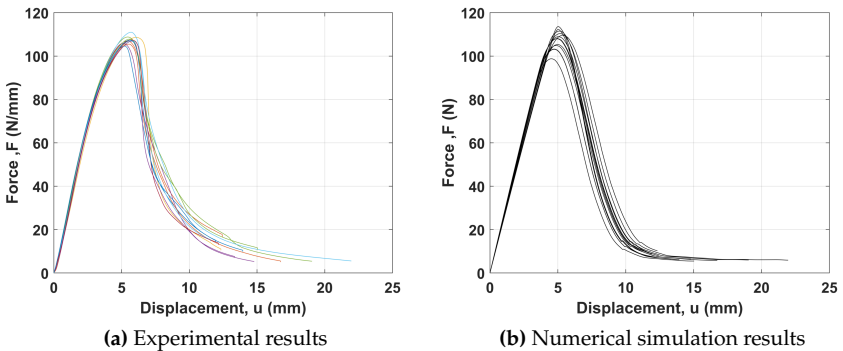


Figure 57: Representation of experimental and numerical simulations of 15 force-displacement curve results.

Table. 6 collects all the identified parameters E , G_c , and l_c , with their respective mean values and standard deviations. Results can now be compared with the outcome of the identification performed on uni-axial tensile tests on the same materials, which was limited to two model parameters, E and l_c . The identified Young modulus in the case of three-point bending tests was 1153.07 ± 35.03 MPa, and it is very close to the identified Young's modulus from the uni-axial tensile tests, which was estimated as 1157.90 ± 34.82 MPa. The identified fracture toughness from three-point bending tests is 8.85 ± 1.94 N/mm and it compares well with the average value taken from the literature and equal to 7.5 N/mm that was set for all the uni-axial tensile tests. A major discrepancy is on the other hand observed as far as the internal length scale parameter l_c is concerned: the identified value from the three-point bending tests is 0.346 ± 0.157 mm, while from the uni-axial tensile tests it was 1.336 ± 0.041 mm. In addition of being smaller, the scatter also increased, as one can notice from the higher value of the standard deviation. Henceforth inverse analysis procedure is strongly suggested to identify length scale parameters for different geometry loading test problems [207]

The comparison between the identified parameters for the two test geometries shows that estimating l_c from uni-axial tensile tests and applying it to other testing geometry can lead to wrong predictions. To better highlight this result, we propose in Fig. 58 a comparison between PF simulations for the two types of tests conducted with different identified values of the internal length scale parameter: (i) identified values from uni-axial tests: $l_c = 1.37$ mm, $E = 1157.90$ MPa and $G_c = 7.5$ N/mm; (ii) identified values from notched three-point bending tests: $l_c = 0.35$ mm, $E = 1153.07$ MPa and $G_c = 8.85$ N/mm. The value of l_c significantly affects both predictions. Therefore, it is highly recommended that the identification of model parameters for the AT2 PF model be performed in relation to meaningful test geometries for fracture mechanics, not using uni-axial tensile tests to infer the value of phase-field parameters.

Test #	E (MPa)	G_c (N/mm)	l_c (mm)
1	1189.39	7.56	0.250
2	1189.67	7.56	0.250
3	1101.17	8.83	0.256
4	1173.92	7.18	0.251
5	1176.29	7.84	0.250
6	1158.87	8.29	0.252
7	1179.82	7.38	0.290
8	1178.73	7.37	0.291
9	1133.36	8.35	0.303
10	1100.58	12.28	0.649
11	1100.40	12.21	0.639
12	1167.95	7.63	0.250
13	1139.86	10.23	0.369
14	1113.41	12.40	0.642
15	1192.62	7.62	0.256
Mean	1153.07	8.85	0.346
Std. dev. (STD)	35.03	1.94	0.157

Table 6: PSO identified E , G_c and l_c parameters for the 15 tests in Fig. 57, with their mean and standard deviation values.

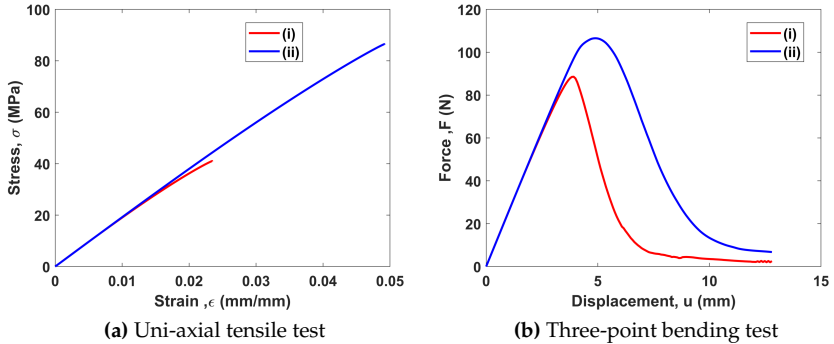
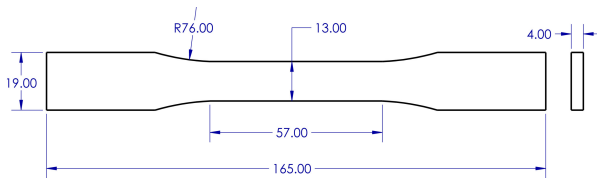


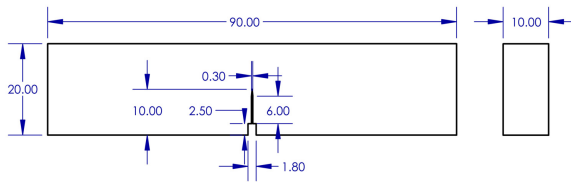
Figure 58: Comparison between numerical results with parameters identified: (i) from uni-axial tensile tests ($l_c = 1.37$ mm, $E = 1157.90$ MPa, $G_C = 7.5$ N/mm); (ii) from notched three-point bending tests ($l_c = 0.35$ mm, $E = 1153.07$ MPa, $G_C = 8.85$ N/mm). The comparison highlights that it is necessary to identify the AT2 PF model parameters independently for each type of test.

5.2 Applications to 3D printing PLA material

The PLA specimens to be tested were fabricated via a material extrusion additive manufacturing technique, namely the Fused Deposition Modelling (FDM). First, the specimen geometries for the tensile test (unnotched specimens) and for the SENB testing geometry were designed in SolidWorks 2021, a computer-aided design (CAD) software, see the geometrical data in Fig. 59. The modeled CAD geometry files were exported in STL files and then transferred to the 3D printer DIVIDE_BY ZERO AION 500 MK2. The G-codes for the FDM printing process were generated using the Slicing software - Simplify 3D. The tested specimens were produced from a PLA+ filament spool commercially available (<https://esun3dstore.com/>).



(a) Tensile specimen CAD model



(b) SENB specimen CAD model

Figure 59: SolidWorks generated CAD geometry models

The PLA filament with an initial diameter of 1.75 mm and density of 1.25 g/cm^3 is hot extruded through a nozzle of 0.6 mm diameter. The extruded filament is deposited layer by layer with respect to material orientation ($\alpha = 0$) onto a pre-heated metallic bed platform by following the G-codes pattern to obtain the desired geometry. The 3D printing process

parameters to manufacture tensile and SENB specimens made of PLA material have been selected according to the recommendations available in the literature (see Table. 7), since it is known that the strength of the tested specimens is greatly influenced by the choice of the printing process parameters [208].

Printing process parameters	Values
Nozzle diameter	0.6 mm
Layer height	0.1 mm
Infill pattern	Aligned
Infill density	100%
Pattern rotation	0°
Nozzle temperature	200 °C
Bed temperature	65 °C
Printing speed	70 mm/s
Travel speed	90 mm/s
Filament diameter	1.75 mm

Table 7: Process parameters for the DIVIDE_BY ZERO AION 500 MK2 3D printer.

5.2.1 Experimental characterization

The tensile and SENB specimens were manufactured with a 0° material orientation and according to the ASTM D638[53] and ASTM D5045-14[55] standards, respectively, as shown in Fig. 60. Ten replicas of tensile and SENB specimens were mechanically tested up to failure using the Tinius Olsen universal testing machine with a 10 kN load cell capacity. In all the tests, a crosshead displacement rate of 3 mm/min has been imposed. The Young’s modulus (E) and the tensile strength (σ_{max}) were collected from the tensile tests, and the data are reported with their mean and standard deviations in Table. 8. The obtained mean value of the Young’s modulus, 1067.2 MPa, is lower than that reported in previous publications [42, 50, 51]. A possible reason might be related to the effect of different printing process parameters [59, 208]. On the other hand, the mean value of the tensile strength, 43.1 MPa, is in the range reported in

the previous literature. The stress-strain curves for the ten tensile samples are shown in Fig. 61: the specimen breaks almost when it reaches the tensile strength, with no sign of plastic yielding and a very brittle behaviour, which justifies the application of the phase-field approach to fracture for brittle materials.

The experimental setup for the SENB tests followed the ASTM D5045-14 standards. The dimensions of the manufactured SENB specimens were set accordingly. Therefore, the fracture toughness K_{IC} ($\text{MPa}\sqrt{\text{m}}$) has been determined by meeting the requirements in Eqs. (5.1a) and (5.1b):

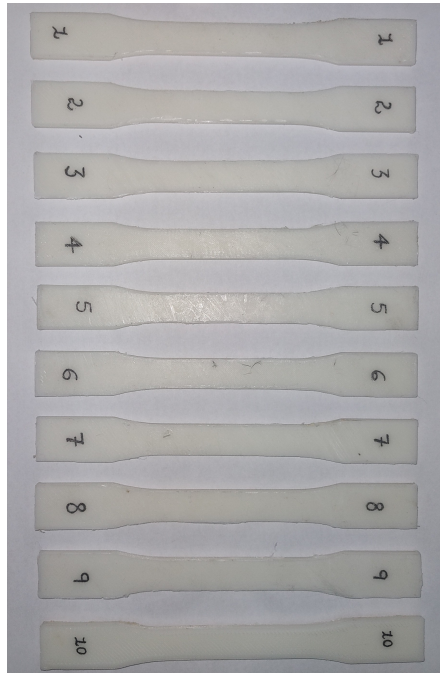
$$(W - a_c) > 2.5 \left(\frac{K_{IC}}{\sigma_{\max}} \right)^2 \quad (5.1a)$$

$$0.45 < \xi < 0.55 \quad (5.1b)$$

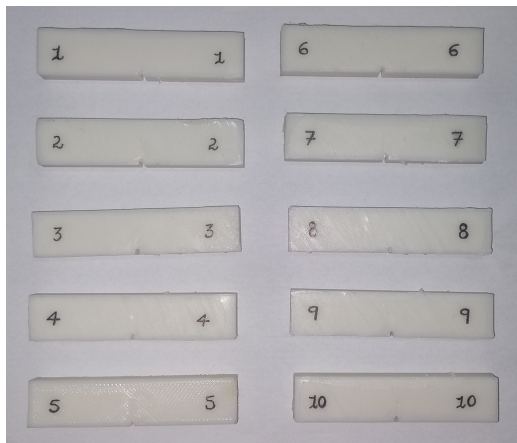
where $\xi = \frac{a_c}{W}$. B and W represent the specimen thickness and height equal to 10 mm and 20 mm, respectively; a_c is the pre-crack length equal to 10 mm; σ_{\max} is the maximum tensile stress at failure estimated from tensile tests, and K_{IC} is the plane-strain fracture toughness of the material. The pre-notch in the specimens has been manufactured during the 3D printing process, to minimize potential imperfections and variations in the value of this parameter.

The SENB tests were performed, and the maximum load (P_{\max}) at failure for each specimen was recorded; see Table. 8. The fracture toughness K_{IC} were determined according to [55] based on Eq. (5.2) for all the SENB specimens and results are reported in Table. 8 with values in the range of $[6 - 9] \text{MPa}\sqrt{\text{m}}$.

$$K_{IC} = \frac{P_{\max}}{B\sqrt{W}} f(\xi) \quad (5.2)$$



(a) Dog bone specimens for the tensile tests



(b) SENB specimens

Figure 60: Photos of the 3D printed PLA specimens.

Specimen No.	Tensile tests		SENB tests		
	E (MPa)	σ_{\max} (MPa)	P_{\max} (N)	K_{IC} (MPa \sqrt{m})	G_{IC} (N/mm)
1	1194.39	38.5	946	7.124	41.39
2	1175.31	46.2	826	6.22	31.56
3	1129.08	39.3	929	7	39.92
4	1072.68	46.1	893	6.72	36.88
5	1059.94	46.2	915	6.89	38.72
6	1003.52	43.9	1170	8.81	63.32
7	965.475	44.1	1200	9.04	66.6
8	994.125	40	1040	7.83	50.03
9	1060.68	42.5	1100	8.28	55.97
10	1016.81	44.2	965	7.52	43.07
Mean	1067.2	43.1	998.44	7.54	46.75
Std. dev.	77.532	124.1	0.93	111.77	1157.904

Table 8: Experimental data obtained by processing the tensile and the SENB tests of 3D printed PLA material.

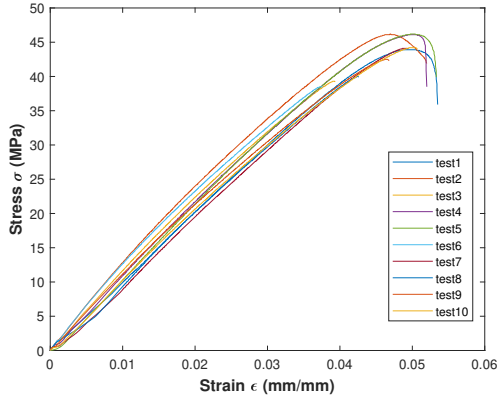


Figure 61: Experimental stress-strain curves from tensile tests.

where the function f for $0 < \xi < 1$ reads:

$$f(\xi) = 6(\xi)^{1/2} \left\{ \frac{1.99 - \xi[1 - \xi] \left[2.15 - 3.93\xi + 2.7(\xi)^2 \right]}{[1 + 2\xi][1 - \xi]^{3/2}} \right\} \quad (5.3)$$

For the application of the phase-field approach to fracture, the relation between fracture toughness K_{IC} and fracture energy G_{IC} for plane

strain conditions is calculated from [209]:

$$G_{IC} = \frac{K_{IC}^2(1 - \nu^2)}{E} \quad (5.4)$$

where E and ν are the Young's modulus and the Poisson's ratio of the material, respectively. To calculate G_{IC} values for SENB specimens, the mean value of $E = 1067.2$ MPa obtained from the tensile tests was considered, and $\nu = 0.36$ was also determined from uniaxial tensile tests and consistently with the literature. The calculated G_{IC} values are reported in Table. 8.

5.2.2 Parameters' identification and sensitivity analysis

The phase-field fracture parameters are herein identified according to the proposed PFF-MLA procedure in case of an anisotropic fracture model, (see Section 3.3). The results in Section 3.3 evidenced that particle swarm optimization (PSO) was outperforming the other metaheuristic algorithms and, therefore, is herein used. The FE mesh of the CAD model shown in Fig. 60(b) was realized with the software Gmsh [203], see Fig. 62. Plane strain conditions are assumed with a fine discretization along the potential direction of crack growth and a total of 1751 finite elements in the model.

The phase-field model for anisotropic fracture implemented into a fully integrated four-node quadrilateral element as a user element in the MATLAB software DAEDALON [186]. The model parameters considered for the initial study of sensitivity analysis were $G_{IC} = 12$ N/mm, $l_c = 2.5$ mm, $E = 2500$ MPa, $\beta = 25$. The design-constrained solution space of the problems is given in Eq. (5.5).

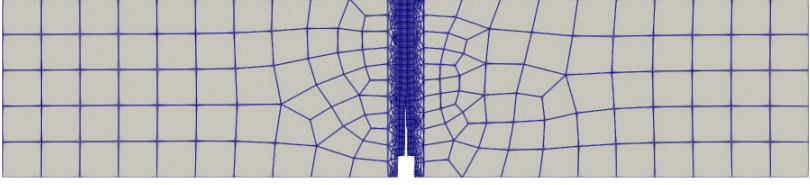


Figure 62: Finite element mesh of the simulated SENB tests.

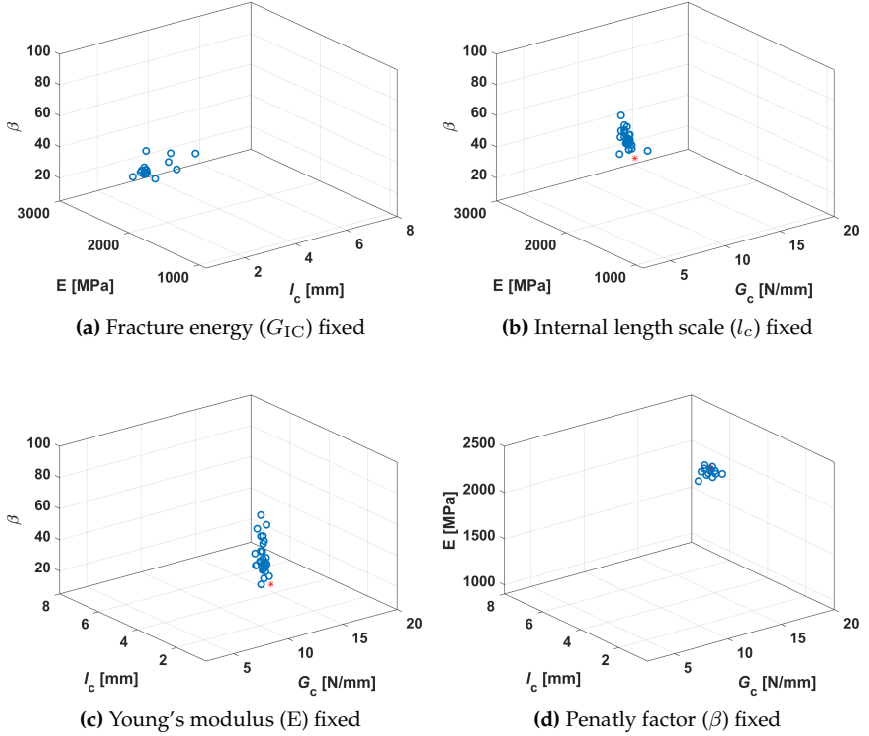


Figure 63: Sensitivity analysis of anisotropic phase-field fracture parameters

$$\mathcal{L} = \{2.5 < G_c < 20 \text{ N/mm}; 0.5 < l_c < 8 \text{ mm}; 900 < E < 3000 \text{ MPa}; 5 < \beta < 100\} \quad (5.5)$$

Fixed parameter	E (MPa)	G_c (N/mm)	l_c (mm)	β	Range E (GPa)	Range G_c (N/mm)	Range l_c (mm)	Range β
G_c	2500	12	2.5	25	900 - 2500	-	0.5 - 8	5 - 100
l_c	2500	12	2.5	25	900 - 2500	2.5 - 20	-	5 - 100
E	2500	12	2.5	25	-	2.5 - 20	0.5 - 8	5 - 100
β	2500	12	2.5	25	900 - 2500	2.5 - 20	0.5 - 8	-

Table 9: Set of input data to generate target responses and range of parameters for the sensitivity analysis of the anisotropic fracture tensor.

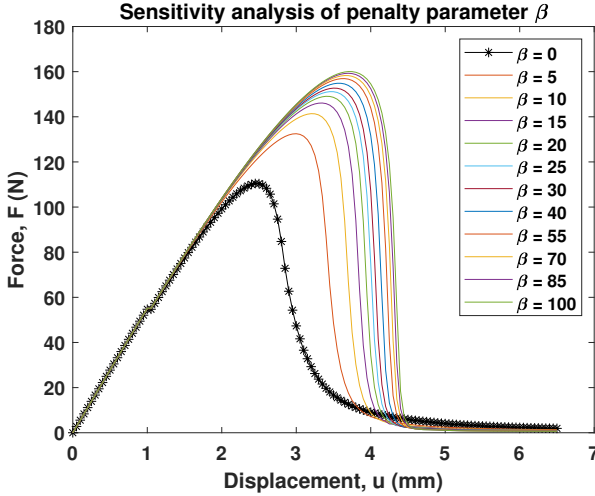


Figure 64: force - displacement curve for $\theta = 0^\circ$, and different β values

Preliminary investigation suggests that all the four design variables (G_c, l_c, E, β) would not yield to converge with the required target solution ($G_c = 12$ N/mm, $l_c = 2.5$ mm, $E = 2500$ MPa, $\beta = 25$). Therefore, it is proposed to investigate the effect of three design parameters by fixing the fourth parameter shown in Table. 9 with the solution ranges mentioned in Eq. (5.5). The optimization simulation results for four cases mentioned in Table. 9 are shown in Fig. 63 reveals that by fixing β the results are converged to the target solution (see Fig. 63(d)). In contrast, by fixing G_c, l_c , and E , the results are not converged to the target solution as in Fig. 63(a),(b),(c) respectively. Hence, the focus shifts to the penalty parameter β in conducting sensitivity analysis. This examination aims to understand the influence of β on determining fracture mechanics pa-

rameters within the anisotropic PFF numerical model. In the context of phase-field modeling for anisotropic fracture, several researchers [61, 64, 62, 65, 210, 211] have made diverse choices of the value of β regarding the constraint on crack orientation along the fracture plane. While the authors have not explicitly discussed the rationale behind the choice of β value, it is evident that selecting an appropriate value for the penalty parameter β is crucial to represent the behavior of anisotropic materials during fracture processes and accurately predict the force-displacement curve. Consequently, the study investigates how varying the penalty parameter β impacts the results of fracture energy (G_c) and peak force (P_{max}) values.

Penalty parameter β	% change with respect to $\alpha = 0^\circ, \beta = 0$	
0	-	-
0.5	0	0
5	19.971	28.457
10	28.024	44.111
15	32.294	53.653
20	34.987	60.222
25	36.856	65.079
30	38.268	68.845
35	39.364	71.866
40	40.215	74.388
45	40.965	76.4888
50	41.569	78.314
55	42.089	79.889
60	42.565	81.301
65	42.97	82.545
70	43.321	83.647
75	43.644	84.69
80	43.955	85.635
85	44.233	86.483
90	44.483	87.282
95	44.709	88.026
100	44.916	88.716

Table 10: Sensitivity analysis of β and percentage (%) change in P_{max}, G_c values for different values of β with respect to case - $\alpha = 0^\circ, \beta = 0$

For sensitivity analysis, the FE model as shown in Fig. 62 is explored and PFF FEA is carried out for different β values ranging from $\{0 - 100\}$ as shown in Table. 10 and compared with isotropic case $\beta = 0$ and material orientation $\alpha = 0^\circ$. The percentage (%) change in peak force (P_{max}) and fracture energy (G_c) values for different β values with respect to case

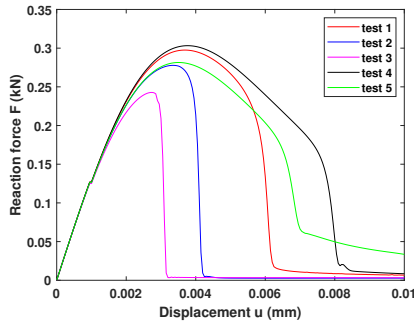
($\alpha = 0^\circ, \beta = 0$) are reported in Table. 10 confirms that there is a significant impact on the results due to the influence of penalty parameter $\beta \in \{0 - 40\}$ and change is negligible with $\beta \in \{45 - 100\}$. This observation is further supported by the force-displacement curve plotted for different β values, as shown in Fig. 64.

The above sensitivity analysis is a result of incorporating the penalty parameter β , which aids in tracking the crack path along material orientation planes α . By increasing the fracture energy G_c along preferential crack path directions, the penalty parameter β also enhances peak force. Therefore, it is advisable to adjust the values of G_c and l_c when employing an anisotropic phase-field for fracture model to improve the prediction of crack path direction and force-displacement curve. In a study by [65] efforts were made to correct the values of G_c and l_c (see Eq. (5.6) where $r=4$) in Eq. (2.13) to maintain the ratio $\frac{G_c}{l_c}$ unchanged, ensuring the physical value of G_c remains consistent within the fracture plane. This prompts the question of whether these corrected values of G_c and l_c can be generalized to any geometry, boundary and loading conditions. The investigation was conducted to validate findings by examining single edge notch tensile and bending test scenarios, as depicted in Figs. 19, 20 of Section 3.3, utilizing identical material properties as input conditions. Numerical tests were executed for various crack surface density functions ($\alpha = 0^\circ, \beta = 25$), as outlined in Table. 11. The force-displacement result plots for both numerical problems are shown in Fig. 65. Tests 1 through 4 were compared with test 5 (refer to Table. 11), revealing from Fig. 65 that the anisotropic crack density function, with or without correction factor, does not align with the isotropic case. In both test problems (see Fig. 65(a),(b)), the force-displacement results for $r = 2$ and $4/3$ underestimate the peak force, while for $r = 4$, test 4 overestimates the peak force compared to the isotropic case.

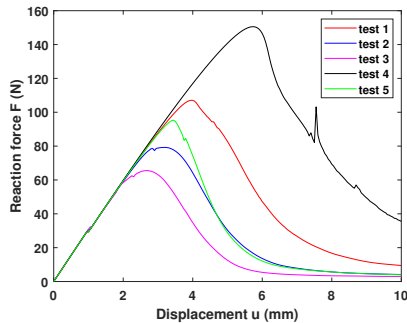
$$G_{cc} = \frac{G_c}{\sqrt{1+\beta}}, \quad l_{cc} = \frac{l_c}{\sqrt{1+\beta}} \quad (5.6)$$

	Crack density function	r value
test 1	Anisotropic crack density function correction	4
test 2	Anisotropic crack density function correction	2
test 3	Anisotropic crack density function correction	4/3
test 4	Anisotropic crack density function without correction	-
test 5	Isotropic crack density function ($\beta = 0$)	-

Table 11: Showing test cases involving varying crack density functions with and without the application of a correction factor for conducting PFF numerical test ($\alpha = 0^\circ, \beta = 25$).



(a) single edge notch tensile test



(b) single edge notch bending test

Figure 65: Force vs. displacement curves for different test cases ($\alpha = 0^\circ, \beta = 25$) as mentioned in Table. 11

Now we deal with the SENB testing problem with dimensions of 90

$\times 20 \text{ mm}^2$, as illustrated in Fig. 66, meshed with 108×24 square finite elements. Material properties selected for analysis were $G_c = 12 \text{ N/mm}$, $l_c = 2.5 \text{ mm}$, $E = 2500 \text{ MPa}$, $\beta = 25$. The pre-notch was introduced by imposing Dirichlet boundary conditions ($\Phi = 1$, depicted in red in Fig. 66). Numerical analysis was conducted for all test cases listed in Table 11. Results indicate that for $r = 2$ in Eq. (5.6), the force-displacement curve closely aligns with the isotropic crack density function while retaining the physical value of G_c . Based on this analysis, it is highly recommended that further investigation be carried out on anisotropic phase-field fracture models to accurately track crack paths and experimental force-displacement curves without compromising the physical value of G_c .

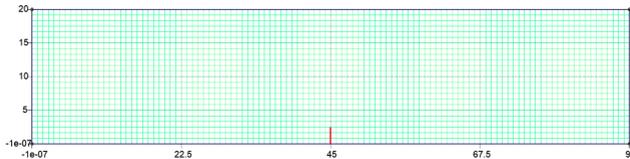


Figure 66: SENB geometric model with meshing details for case $\alpha = 0^\circ$, $\beta = 25$

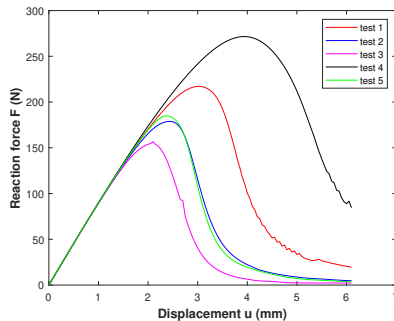


Figure 67: force-displacement curve for SENB numerical problem (see Fig. 66) for case $\alpha = 0^\circ$, $\beta = 25$

Chapter 6

Conclusions and future developments

Chapter 6 is partially based on the content of publications [1, 2] and article in press [3].

The main contribution of this thesis is divided into two sections. The first section describes about how machine learning algorithms evaluate and identify numerically the phase-field fracture and cohesive zone model parameters to accurately capture the experimental mechanical response of the structural problems. The second section summarizes how the SIMP topology optimization of structures using gradient based OC method can be applied to the complex structural problems undergoing delamination and fracture.

6.1 Conclusion on identification of fracture parameters

This section first discusses the identification of phase-field fracture parameters using metaheuristic algorithms, followed by a discussion on the identification of cohesive zone model parameters.

6.1.1 Investigation on phase-field fracture parameters

Chapter 2 described brief insights into the theory and FE numerical implementation of the phase-field for fracture (PFF) model, considering both isotropic and anisotropic cases. The critical issue of model parameters' identification for the phase-field approach to fracture, as outlined in Section 1.2 of Chapter 1, was systematically addressed in this work. The framework proposed in Section 3.2 combined the heuristic identification approach based on Particle Swarm Optimization (PSO) with the FE implementation of the phase-field (PF) approach to fracture, effectively identifying model parameters. Both formulations were implemented in MATLAB release 2020b in an ad hoc integrated FE software. Nevertheless, the methodology was general and required an FE solver equipped with PF finite elements to be called by the PSO algorithm with a set of model parameters. The outcome of the FE simulation, in terms of the force-displacement curve, was passed to the PSO algorithm, which computed the cost function and updated the particle coordinates, iterating the procedure until convergence. Therefore, any commercial FE software could be triggered using the system command called by the PSO algorithm. The robustness of the proposed approach was assessed in relation to a series of benchmark tests numerically generated in silico, i.e., by running a series of PF fracture simulations with known model parameters. The PSO algorithm accurately retrieved the known input parameters from the identification procedure.

The methodology was finally applied to the critical problem of identifying the AT2 PF model parameters concerning real experimental tests on ABS materials, which displayed a spread of diffuse damage typical of a quasi-brittle material. In Section 5.1, the PSO-PF combined approach was applied to uni-axial tensile tests, identifying only E and l_c from the experimental curve up to the decay of the peak load. The uni-axial tests for this material could not be used to assess the fracture energy, which was set equal to the average value taken from the literature since the material underwent strain localization with the crazing formation and large deformation in the post-peak branch, a situation far from the fracture.

In Section 5.1.2, the identification procedure was repeated for sharp V-notched samples tested under three-point bending. This time, all three model parameters (E , G_c , l_c) were identified since the post-peak branch could be reasonably well simulated as a result of a propagating crack.

To summarize the work, the proposed algorithm quantitatively tracked the crack path phenomenon of the fracture problem. In addition, it also captured numerically experimental force-displacement curve responses by identifying phase-field model parameters, which was a significant challenge due to the high dependence on the PF internal length scale parameter, as mentioned in Section 1.2 of Chapter 1. Therefore, the PSO-PF numerically coupled algorithm provided qualitative insight into fracture design problems by avoiding under or overestimating critical structural limits of the load, which saved computational time and the cost of the material.

Analogously, in Section 3.3, we proposed the combined PFF-MLA approach to tackle inverse problems and identify the phase-field fracture parameters. The metaheuristics machine learning algorithms (MLA) like PSO, PSO-GA, ABC-PSO, CS, TLBO, and EJAYA algorithms were compared to identify the best parametric analysis optimization algorithm. Mode-I tensile and SENB loading condition numerical test problems were chosen for analysis considering the isotropic case ($\beta = 0$). Results reported that particle swarm optimization (PSO) was more efficient and robust in identifying fracture mechanics parameters than PSO-GA, ABC-PSO, CS, TLBO, and EJAYA. Therefore, in Section 5.2.2, the sensitivity analysis of the fracture mechanics parameters was carried out using the PFF-PSO MLA considering the anisotropic case ($\beta \neq 0$). The fracture energy release rate G_c related to a crack along the interface was overestimated. Additionally, the peak force was increased due to the influence of the penalty parameter β . The sensitivity analysis reported that the anisotropic phase-field for the fracture model needed further investigation for a good prediction of quantitative results in addition to qualitative analysis of the crack path. Section 5.2 discussed the experimental analysis of 3D-printed PLA material. The study was limited to reporting material properties: Young's modulus (E), maximum tensile stress (σ_{max})

from tensile tests, and fracture energy properties K_{IC} , G_{IC} from single edge notch bending tests. The results were reported following ASTM standards.

6.1.2 Investigation on cohesive zone interface parameters

In this work, structures that could be subject to delamination were analyzed with reference to two methods to improve their mechanical response. In Section 2.4.1, the theory and FE numerical implementation of cohesive zone modeling were discussed. A nonlinear cohesive interface model described by the Tvergaard CZM, as a typical model traction-separation law, was considered, and the possibility of designing cohesive interfaces with a linear variation in the fracture properties along the interface to improve resistance to peeling was investigated. This novel solution, which is now technically feasible by exploiting micro-structured adhesives, was investigated by framing the problem within an inverse analysis, where the extremal values of the fracture energy were considered as design variables. The application of the data-driven heuristic optimization approach based on the PSO algorithm proposed in Section 3.2.1 allowed the identification of optimal values of the fracture properties to match a target mechanical response. The obtained solution was found to surpass the response of an interface with a uniform average interface fracture energy. The future scope of work included addressing more complex problems by conducting experiments on curvilinear adhesive bonding structures and performing numerical validation for the identification of cohesive zone model physical parameters using machine learning models to accurately predict the underlying physics of the problem.

6.2 Conclusion of topology optimization of fracture resistant structures

The first aspect of this section concluded about cohesive interface

structures that were considered regarding the design of substrates with a topology optimized to withstand the onset of delamination. In this work, the optimal topology was found by applying a physics-based mathematical approach that relied on a density-based optimization algorithm using the gradient-based optimality criteria (OC) method, as mentioned in Section 4.1. The continuous design density variable adopted the solid isotropic material with penalization (SIMP) approach, along with a density filtering scheme implemented to avoid non-locality and checkerboard patterns, according to the state of the art. In Section 4.2, a linearly graded interface binding the substrate and the deformable layer was analyzed, and a peeling displacement was applied to delaminate a certain portion of the CZI region, considering extensions compatible with the onset of debonding. The substrate topology was identified for two cases with different amounts of delamination, and results showed that the identified optimal topology of the substrate was mildly dependent upon the extension of the onset of debonding. This provided good perspectives on the possibility of optimizing the internal material to maximize the stiffness of the system in case of potential delamination events. Furthermore, in Section 4.2.1, the effect of volume fraction on the optimized substrate topology was investigated and reported in identifying the best structural volume fraction optimized design. The results reported in this work contributed to the knowledge of structural mechanics, particularly for engineers and researchers working with composite materials or structures bonded with adhesives.

The second aspect presented a novel approach integrating phase-Field fracture (PFF) with Topology Optimization (TO), as mentioned in Section 4.3, to analyze composite structures composed of inclusion-matrix phase materials while considering initially induced damage. The phase-field numerical model, employing a staggered solution scheme, was proficient in capturing crack branching. By regularizing the discontinuous field, there was no necessity for re-meshing, providing a significant advantage during the TO process. Within the TO framework, the application of the Solid Isotropic Material with Penalization (SIMP) methodology aimed to maximize fracture resistance in damaged structures. The Optimality Cri-

teria (OC) algorithm was integrated into the SIMP methodology to iteratively update design variables during the optimization process. In Fig. 52, the proposed PFF-TO algorithm began with phase-field fracture (PFF) simulations to incorporate initial damage into the structure under service load effects. Subsequently, the Topology Optimization (TO) process iterated, employing PFF simulations until failure at each optimization step, aiming for an optimal distribution of inclusion phase material within a volume constraint, particularly in the vicinity of the crack influence region, while considering the entire loading history. This iterative process resulted in an optimized structural design capable of withstanding fracture. Following optimization, PFF simulations were conducted on the optimized structure until failure to assess crack patterns and evaluate its fracture-resistant capabilities compared to the initial design. In Section 4.5, several benchmark problems demonstrated promising outcomes, indicating the efficacy of this methodology in refining structural designs to enhance fracture resistance, particularly in scenarios involving structures affected by initial damage due to service loads. This offered valuable insights for innovative structural design applications.

The research on computational methods and material models continues to evolve, and the potential for further breakthroughs in fracture-resistant design is immense, promising a future where structural failures are minimized and performance is maximized.

6.3 Future developments

- The findings presented in Chapter 3 motivate us to further explore more complex issues through experiments involving curvilinear adhesive bonding structures. Subsequently, numerical validation is carried out to determine the physical parameters of the cohesive zone model (CZM) using machine learning models, which are designed to accurately predict the fundamental physics of the problem. The proposed inverse parameter identification framework is crucial for determining CZM properties in various engineering and biomedical applications, such as fiber-reinforced interfaces and bi-

ological materials with interfaces, among others.

- The FEM code implemented in MATLAB software [186] was extensively used in our PhD research to develop subroutines for phase-field and cohesive zone models. This experience motivated us to develop a FEM code on the Python platform, enabling the application to structural problems related to fracture mechanics. This approach leverages the robust Python libraries available for machine learning (ML) techniques and remaining useful life (RUL) predictions.
- The results reported in Chapter 5 motivate us to investigate and simulate the experimental force-displacement response curve with an anisotropic phase-field for fracture model tracking the crack path qualitatively without compromising the quantitative results (Force-displacement results) and for different material fiber orientations. This analysis is very useful and demanding in understanding fracture behavior in materials manufactured using the 3D printing process, which naturally exhibits anisotropic behavior.
- The thesis work on metaheuristic optimization techniques reported in Chapter 3, 5 requires high computational cost for more complex problems and needs more iterations using fracture numerical models to capture highly nonlinear behavior of the material. This motivates us to explore Physics-informed neural networks(PINN), which have been a promising research field in recent years. PINNs incorporate the underlying physics of the problem directly into the neural network's loss function. This enables PINNs to efficiently learn the parameters by minimizing discrepancies between the predicted and experimental observed behavior (force-displacement response). Furthermore, PINNs provide a more robust framework for handling complex, high-dimensional problems, as they can leverage both data and physics-based constraints, thus achieving faster convergence and higher accuracy in identifying fracture parameters than traditional metaheuristic approaches.

- The results presented in Chapter 4 suggest new possibilities for designing functionally optimized structures to resist fracture or delamination at interfaces, which is crucial for applications in aerospace, marine sectors, and additive manufacturing industries. This can be accomplished by employing metaheuristic algorithms or physics-informed neural networks (PINNs) for optimizing fracture model parameters to achieve the desired force-displacement response. Simultaneously, a topology optimization algorithm can be used to evolve the structure to achieve either minimized weight or maximized stiffness.

Bibliography

- [1] T. Rakesh Kumar and M. Paggi. “A robust identification procedure for phase field fracture mechanics parameters”. In: *Theoretical and Applied Fracture Mechanics* 127 (2023), p. 104005. DOI: <https://doi.org/10.1016/j.tafmec.2023.104005>.
- [2] JM Chandra Kishen, A Ramaswamy, S Ray, et al. “A PSO IDENTIFICATION PROCEDURE FOR PHASE FIELD FRACTURE MECHANICS PARAMETERS”. In: (). DOI: <https://doi.org/10.21012/FC11.092325>.
- [3] Tota Rakesh Kumar and Marco Paggi. “Data-driven and physics-based methods to optimize structures against delamination”. In: *Mechanics of Advanced Materials and Structures* -In press (2024). DOI: <https://doi.org/10.1080/15376494.2024.2372696>.
- [4] PA Wawrzynek and Ingraffea AR. “Interactive finite element analysis of fracture processes: an integrated approach”. In: *Theoretical and Applied Fracture Mechanics* 8 (1987), pp. 137–150. DOI: [https://doi.org/10.1016/0167-8442\(87\)90007-3](https://doi.org/10.1016/0167-8442(87)90007-3).
- [5] M Paggi and A Carpinteri. “On the Stress Singularities at Multi-material Interfaces and Related Analogies With Fluid Dynamics and Diffusion”. In: *Applied Mechanics Reviews* 61.2 (2008). 020801. DOI: <https://doi.org/10.1115/1.2885134>.
- [6] J Lemaitre and R Desmorat. *Engineering Damage Mechanics: Ductile, Creep, Fatigue and Brittle Failures*. Springer-Verlag, Berlin, 2005.
- [7] ZP Bažant and TGP Pijaudier-Cabot. “Nonlocal continuum damage, localization instability and convergence”. In: *Journal of Applied Mechanics* 55 (1988), pp. 287–293. DOI: <https://doi.org/10.1115/1.3173674>.

- [8] M Jirásek. “Nonlocal models for damage and fracture: Comparison of approaches”. In: *Int. J. Solids Struct.* 35 (1998), pp. 4133–4145. DOI: [Nonlocalmodelsfordamageandfracture:Comparisonofapproaches](https://doi.org/10.1016/S0020-7683(98)00087-7).
- [9] S Forest. “Micromorphic approach for gradient elasticity, viscoplasticity, and damage”. In: *Journal of Engineering Mechanics* 135 (2009), pp. 117–131. DOI: [https://doi.org/10.1061/\(ASCE\)0733-9399\(2009\)135:3\(117\)](https://doi.org/10.1061/(ASCE)0733-9399(2009)135:3(117)).
- [10] BJ Dimitrijevic and K Hackl. “A regularization framework for damage-plasticity models via gradient enhancement of the free energy”. In: *Int. J. Numer. Methods Biomed. Eng.* 27 (2011), pp. 1199–1210. DOI: <https://doi.org/10.1002/cnm.1350>.
- [11] R Peerlings et al. “A critical comparison of non local and gradient-enhanced softening continua”. In: *Int. J. Solids Struct.* 38 (2001), pp. 7723–7746. DOI: [https://doi.org/10.1016/S0020-7683\(01\)00087-7](https://doi.org/10.1016/S0020-7683(01)00087-7).
- [12] N Moës, J Dolbow, and T Belytschko. “A finite element method for crack growth without remeshing”. In: *Internat. J. Numer. Methods Engrg.* 46 (1999), pp. 131–150. DOI: [https://doi.org/10.1002/\(SICI\)1097-0207\(19990910\)46:1<131::AID-NME726>3.0.CO;2-J](https://doi.org/10.1002/(SICI)1097-0207(19990910)46:1<131::AID-NME726>3.0.CO;2-J).
- [13] J Dolbow, N Moës, and T Belytschko. “An extended finite element method for modeling crack growth with contact”. In: *Comput. Methods Appl. Mech. Engrg.* 190 (2001), pp. 6825–6846. DOI: [https://doi.org/10.1016/S0045-7825\(01\)00260-2](https://doi.org/10.1016/S0045-7825(01)00260-2).
- [14] TP Fries and T Belytschko. “The extended/generalized finite element method: an overview of the method and its applications”. In: *Internat. J. Numer. Methods Engrg.* 84 (2010), pp. 253–304. DOI: <https://doi.org/10.1002/nme.2914>.
- [15] JC Simo, J Oliver, and F Armero. “An analysis of strong discontinuities induced by strain-softening in rate-independent inelastic solids”. In: *Comput. Mech.* 12 (1993), pp. 277–296. DOI: <https://doi.org/10.1007/BF00372173>.
- [16] C Linder and F Armero. “Finite elements with embedded strong discontinuities for the modeling of failure in solids”. In: *Internat. J. Numer. Methods Engrg.* 72 (2007), pp. 1391–1433. DOI: <https://doi.org/10.1002/nme.2042>.

- [17] F Armero and C Linder. “New finite elements with embedded strong discontinuities for finite deformations”. In: *Comput. Methods Appl. Mech. Engrg.* 198 (2008), pp. 3138–3170. DOI: <https://doi.org/10.1016/j.cma.2008.02.021>.
- [18] J Oliver et al. “Stability and robustness issues in numerical modeling of material failure with the strong discontinuity approach”. In: *Comput. Methods Appl. Mech. Engrg.* 195 (2006), pp. 7093–7114. DOI: <https://doi.org/10.1016/j.cma.2005.04.018>.
- [19] GA Francfort and J-J Marigo. “Revisiting brittle fracture as an energy minimization problem”. In: *Journal of the Mechanics and Physics of Solids* 46.8 (1998), pp. 1319–1342. DOI: [https://doi.org/10.1016/S0022-5096\(98\)00034-9](https://doi.org/10.1016/S0022-5096(98)00034-9).
- [20] Luigi Ambrosio and Vincenzo Maria Tortorelli. “Approximation of functional depending on jumps by elliptic functional via Γ -convergence”. In: *Communications on Pure and Applied Mathematics* 43.8 (1990), pp. 999–1036. DOI: <https://doi.org/10.1002/cpa.3160430805>.
- [21] AA Griffith. “The phenomena of rupture and flow in solids”. In: *Philos. Trans. R. Soc. Lond. Ser. A* 221 (1921), pp. 163–198. DOI: <https://doi.org/10.1098/rsta.1921.0006>.
- [22] Blaise Bourdin, Gilles A Francfort, and Jean-Jacques Marigo. “Numerical experiments in revisited brittle fracture”. In: *Journal of the Mechanics and Physics of Solids* 48.4 (2000), pp. 797–826. DOI: [https://doi.org/10.1016/S0022-5096\(99\)00028-9](https://doi.org/10.1016/S0022-5096(99)00028-9).
- [23] Christian Miehe, Martina Hofacker, and Fabian Welschinger. “A phase field model for rate-independent crack propagation: Robust algorithmic implementation based on operator splits”. In: *Computer Methods in Applied Mechanics and Engineering* 199.45-48 (2010), pp. 2765–2778. DOI: <https://doi.org/10.1016/j.cma.2010.04.011>.
- [24] M Ambati, T Gerasimov, and L De Lorenzis. “A review on phase-field models of brittle fracture and a new fast hybrid formulation”. In: *Computational Mechanics* 55 (2015), pp. 383–405. DOI: <https://doi.org/10.1007/s00466-014-1109-y>.

- [25] R Cavuoto et al. "Failure through crack propagation in components with holes and notches: An experimental assessment of the phase field model". In: *International Journal of Solids and Structures* 257 (2022), p. 111798. DOI: <https://doi.org/10.1016/j.ijsolstr.2022.111798>.
- [26] Erwan Tanné et al. "Crack nucleation in variational phase-field models of brittle fracture". In: *Journal of the Mechanics and Physics of Solids* 110 (2018), pp. 80–99. DOI: <https://doi.org/10.1016/j.jmps.2017.09.006>.
- [27] Tao Wu et al. "Parameter identification for phase-field modeling of fracture: a Bayesian approach with sampling-free update". In: *Computational Mechanics* 67 (2021), pp. 435–453. DOI: <https://doi.org/10.1007/s00466-020-01942-x>.
- [28] V Carollo et al. "Identification of elasto-plastic and nonlinear fracture mechanics parameters of silver-plated copper busbars for photovoltaics". In: *Engineering Fracture Mechanics* 205 (2019), pp. 439–454. DOI: <https://doi.org/10.1016/j.engfracmech.2018.11.014>.
- [29] Ana Vafadar et al. "Advances in metal additive manufacturing: a review of common processes, industrial applications, and current challenges". In: *Applied Sciences* 11.3 (2021), p. 1213. DOI: <https://doi.org/10.3390/app11031213>.
- [30] Gulnaaz Rasiya, Abhinav Shukla, and Karan Saran. "Additive manufacturing-a review". In: *Materials Today: Proceedings* 47 (2021), pp. 6896–6901. DOI: <https://doi.org/10.1016/j.matpr.2021.05.181>.
- [31] Anketa Jandyal et al. "3D printing–A review of processes, materials and applications in industry 4.0". In: *Sustainable Operations and Computers* 3 (2022), pp. 33–42. DOI: <https://doi.org/10.1016/j.susoc.2021.09.004>.
- [32] Jinliang Zhang et al. "A review of selective laser melting of aluminum alloys: Processing, microstructure, property and developing trends". In: *Journal of Materials Science & Technology* 35.2 (2019), pp. 270–284. DOI: <https://doi.org/10.1016/j.jmst.2018.09.004>.
- [33] Jordi Delgado et al. "Selective Laser Sintering". In: *Modern Manufacturing Processes* (2019), pp. 481–499. DOI: <https://doi.org/10.1002/9781119120384.ch20>.

- [34] Daniela Fico et al. "A review of polymer-based materials for fused filament fabrication (FFF): focus on sustainability and recycled materials". In: *Polymers* 14.3 (2022), p. 465. DOI: <https://doi.org/10.3390/polym14030465>.
- [35] Kamaljit Singh Boparai, Rupinder Singh, and Harwinder Singh. "Development of rapid tooling using fused deposition modeling: a review". In: *Rapid Prototyping Journal* 22.2 (2016), pp. 281–299. DOI: <https://doi.org/10.1108/RPJ-04-2014-0048>.
- [36] Dong-Gyu Ahn. "Directed energy deposition (DED) process: State of the art". In: *International Journal of Precision Engineering and Manufacturing-Green Technology* 8 (2021), pp. 703–742. DOI: <https://doi.org/10.1007/s40684-020-00302-7>.
- [37] Sunpreet Singh, Seeram Ramakrishna, and Filippo Berto. "3D Printing of polymer composites: A short review". In: *Material Design & Processing Communications* 2.2 (2020), e97. DOI: <https://doi.org/10.1002/mdp2.97>.
- [38] Ankit Sharma and Aryan Rai. "Fused deposition modelling (FDM) based 3D & 4D Printing: A state of art review". In: *Materials Today: Proceedings* 62 (2022), pp. 367–372. DOI: <https://doi.org/10.1016/j.matpr.2022.03.679>.
- [39] Behzad Rankouhi et al. "Failure analysis and mechanical characterization of 3D printed ABS with respect to layer thickness and orientation". In: *Journal of Failure Analysis and Prevention* 16 (2016), pp. 467–481. DOI: <https://doi.org/10.1007/s11668-016-0113-2>.
- [40] T Panneerselvam, S Raghuraman, and N Vamsi Krishnan. "Investigating mechanical properties of 3D-printed polyethylene terephthalate glycol material under fused deposition modeling". In: *Journal of The Institution of Engineers (India): Series C* 102 (2021), pp. 375–387. DOI: <https://doi.org/10.1007/s40032-020-00646-8>.
- [41] Daniel-Alexander Türk et al. "Mechanical characterization of 3D printed polymers for fiber reinforced polymers processing". In: *Materials & Design* 118 (2017), pp. 256–265. DOI: <https://doi.org/10.1016/j.matdes.2017.01.050>.

- [42] Liviu Marşavina et al. "Effect of the manufacturing parameters on the tensile and fracture properties of FDM 3D-printed PLA specimens". In: *Engineering Fracture Mechanics* 274 (2022), p. 108766. DOI: <https://doi.org/10.1016/j.engfracmech.2022.108766>.
- [43] Reda M Felfel et al. "Accelerated in vitro degradation properties of polylactic acid/phosphate glass fibre composites". In: *Journal of Materials Science* 50 (2015), pp. 3942–3955. DOI: <https://doi.org/10.1007/s10853-015-8946-8>].
- [44] Moataz A Elsayw et al. "Hydrolytic degradation of polylactic acid (PLA) and its composites". In: *Renewable and Sustainable Energy Reviews* 79 (2017), pp. 1346–1352. DOI: <https://doi.org/10.1016/j.rser.2017.05.143>.
- [45] Vidhya Nagarajan, Amar K Mohanty, and Manjusri Misra. "Perspective on polylactic acid (PLA) based sustainable materials for durable applications: Focus on toughness and heat resistance". In: *ACS Sustainable Chemistry & Engineering* 4.6 (2016), pp. 2899–2916. DOI: <https://doi.org/10.1021/acssuschemeng.6b00321>.
- [46] Sara Zohoor, Nabiollah Abolfathi, and Mehran Solati-Hashjin. "Accelerated degradation mechanism and mechanical behavior of 3D-printed PLA scaffolds for bone regeneration". In: *Iranian Polymer Journal* 32.10 (2023), pp. 1209–1227. DOI: <https://doi.org/10.1007/s13726-023-01191-8>.
- [47] Pei Feng et al. "Degradation mechanisms and acceleration strategies of poly (lactic acid) scaffold for bone regeneration". In: *Materials & Design* 210 (2021), p. 110066. DOI: <https://doi.org/10.1016/j.matdes.2021.110066>.
- [48] Ravikumar Patel et al. "A review article on FDM process parameters in 3D printing for composite materials". In: *Materials Today: Proceedings* 60 (2022), pp. 2162–2166. DOI: <https://doi.org/10.1016/j.matpr.2022.02.385>.
- [49] JM Chacón et al. "Additive manufacturing of PLA structures using fused deposition modelling: Effect of process parameters on mechanical properties and their optimal selection". In: *Materials & Design* 124 (2017), pp. 143–157. DOI: <https://doi.org/10.1016/j.matdes.2017.03.065>.

- [50] Yu Zhao, Yuansong Chen, and Yongjun Zhou. "Novel mechanical models of tensile strength and elastic property of FDM AM PLA materials: Experimental and theoretical analyses". In: *Materials & Design* 181 (2019), p. 108089. DOI: <https://doi.org/10.1016/j.matdes.2019.108089>.
- [51] Shuheng Wang et al. "Effects of fused deposition modeling process parameters on tensile, dynamic mechanical properties of 3D printed polylactic acid materials". In: *Polymer testing* 86 (2020), p. 106483. DOI: <https://doi.org/10.1016/j.polymertesting.2020.106483>.
- [52] Rui Zou et al. "Isotropic and anisotropic elasticity and yielding of 3D printed material". In: *Composites Part B: Engineering* 99 (2016), pp. 506–513. DOI: <https://doi.org/10.1016/j.compositesb.2016.06.009>.
- [53] ASTM International. *Standard test method for tensile properties of plastics*. 2014. DOI: 10.1520/D0638-14.
- [54] Yichi Song et al. "Measurements of the mechanical response of unidirectional 3D-printed PLA". In: *Materials & Design* 123 (2017), pp. 154–164. DOI: <https://doi.org/10.1016/j.matdes.2017.03.051>.
- [55] ASTM International. "Standard test methods for plane-strain fracture toughness and strain energy release rate of plastic materials". In: *ASTM D5045-99* (2007). DOI: 10.1520/D5045-14.
- [56] Tait D McLouth et al. "The impact of print orientation and raster pattern on fracture toughness in additively manufactured ABS". In: *Additive Manufacturing* 18 (2017), pp. 103–109. DOI: <https://doi.org/10.1016/j.addma.2017.09.003>.
- [57] Kevin R Hart and Eric D Wetzel. "Fracture behavior of additively manufactured acrylonitrile butadiene styrene (ABS) materials". In: *Engineering Fracture Mechanics* 177 (2017), pp. 1–13. DOI: <https://doi.org/10.1016/j.engfracmech.2017.03.028>.
- [58] Omar S Es-Said et al. "Effect of layer orientation on mechanical properties of rapid prototyped samples". In: *Materials and Manufacturing Processes* 15.1 (2000), pp. 107–122. DOI: <https://doi.org/10.1080/10426910008912976>.

- [59] Makara Lay et al. "Comparison of physical and mechanical properties of PLA, ABS and nylon 6 fabricated using fused deposition modeling and injection molding". In: *Composites Part B: Engineering* 176 (2019), p. 107341. DOI: <https://doi.org/10.1016/j.compositesb.2019.107341>.
- [60] Christian Miehe, Martina Hofacker, and Fabian Welschinger. "A phase field model for rate-independent crack propagation: Robust algorithmic implementation based on operator splits". In: *Computer Methods in Applied Mechanics and Engineering* 199.45-48 (2010), pp. 2765–2778. DOI: <https://doi.org/10.1016/j.cma.2010.04.011>.
- [61] JD Clayton and JCMS Knap. "Phase field modeling of directional fracture in anisotropic polycrystals". In: *Computational Materials Science* 98 (2015), pp. 158–169. DOI: <https://doi.org/10.1016/j.commatsci.2014.11.009>.
- [62] S Teichtmeister et al. "Phase field modeling of fracture in anisotropic brittle solids". In: *International Journal of Non-Linear Mechanics* 97 (2017), pp. 1–21. DOI: <https://doi.org/10.1016/j.ijnonlinmec.2017.06.018>.
- [63] Bin Li and Corrado Maurini. "Crack kinking in a variational phase-field model of brittle fracture with strongly anisotropic surface energy". In: *Journal of the Mechanics and Physics of Solids* 125 (2019), pp. 502–522. DOI: <https://doi.org/10.1016/j.jmps.2019.01.010>.
- [64] Thanh-Tung Nguyen et al. "Multi-phase-field modeling of anisotropic crack propagation for polycrystalline materials". In: *Computational Mechanics* 60 (2017), pp. 289–314. DOI: [10.1007/s00466-017-1409-0](https://doi.org/10.1007/s00466-017-1409-0).
- [65] Soukaina Riad, Didier Bardel, and Julien Réthoré. "Unified phase field model to simulate both intergranular and transgranular failure in polycrystalline aggregates". In: *Finite Elements in Analysis and Design* 194 (2021), p. 103555. DOI: <https://doi.org/10.1016/j.finel.2021.103555>.
- [66] Jeremy Bleyer and Roberto Alessi. "Phase-field modeling of anisotropic brittle fracture including several damage mechanisms". In: *Computer Methods in Applied Mechanics and Engineering* 336 (2018), pp. 213–236. DOI: <https://doi.org/10.1016/j.cma.2018.03.012>.

- [67] James Kennedy and Russell Eberhart. "Particle swarm optimization". In: *Proceedings of ICNN'95-international conference on neural networks*. Vol. 4. 1995, pp. 1942–1948. DOI: 10.1109/ICNN.1995.488968.
- [68] Rakesh Kumar Tota and Marco Paggi. "A robust identification procedure for phase field fracture mechanics parameters". In: *Theoretical and Applied Fracture Mechanics* 127 (2023), p. 104005. DOI: <https://doi.org/10.1016/j.tafmec.2023.104005>.
- [69] V Carollo et al. "Identification of elasto-plastic and nonlinear fracture mechanics parameters of silver-plated copper busbars for photovoltaics". In: *Engineering Fracture Mechanics* 205 (2019), pp. 439–454. DOI: <https://doi.org/10.1016/j.engfracmech.2018.11.014>.
- [70] Russ C Eberhart and Yuhui Shi. "Comparing inertia weights and constriction factors in particle swarm optimization". In: *Proceedings of the 2000 congress on evolutionary computation. CEC00 (Cat. No. 00TH8512)*. Vol. 1. 2000, pp. 84–88. DOI: 10.1109/CEC.2000.870279.
- [71] Qiang Zhang, Ryan M Ogren, and Song-Charng Kong. "A comparative study of biodiesel engine performance optimization using enhanced hybrid PSO–GA and basic GA". In: *Applied energy* 165 (2016), pp. 676–684. DOI: <https://doi.org/10.1016/j.apenergy.2015.12.044>.
- [72] Mohammed El-Abd. "A hybrid ABC-SPSO algorithm for continuous function optimization". In: *2011 IEEE Symposium on Swarm Intelligence*. 2011, pp. 1–6. DOI: 10.1109/SIS.2011.5952576.
- [73] Zhiyong Li et al. "PS–ABC: A hybrid algorithm based on particle swarm and artificial bee colony for high-dimensional optimization problems". In: *Expert Systems with Applications* 42.22 (2015), pp. 8881–8895. DOI: <https://doi.org/10.1016/j.eswa.2015.07.043>.
- [74] Rohit Salgotra, Urvinder Singh, and Sriparna Saha. "New cuckoo search algorithms with enhanced exploration and exploitation properties". In: *Expert Systems with Applications* 95 (2018), pp. 384–420. DOI: <https://doi.org/10.1016/j.eswa.2017.11.044>.

- [75] R Venkata Rao and Vivek D Kalyankar. "Parameter optimization of modern machining processes using teaching–learning-based optimization algorithm". In: *Engineering Applications of Artificial Intelligence* 26.1 (2013), pp. 524–531. DOI: <https://doi.org/10.1016/j.engappai.2012.06.007>.
- [76] Yiyang Zhang, Aining Chi, and Seyedali Mirjalili. "Enhanced Jaya algorithm: A simple but efficient optimization method for constrained engineering design problems". In: *Knowledge-Based Systems* 233 (2021), p. 107555. DOI: <https://doi.org/10.1016/j.knosys.2021.107555>.
- [77] Raed Abu Zitar et al. "An intensive and comprehensive overview of JAYA algorithm, its versions and applications". In: *Archives of Computational Methods in Engineering* 29.2 (2022), pp. 763–792. DOI: <https://doi.org/10.1007/s11831-021-09585-8>.
- [78] A.N. Gent. "Adhesion and strength of viscoelastic solids. Is there a relationship between adhesion and bulk properties?" In: *Langmuir* 12.19 (1996), pp. 4492–4496. DOI: <https://doi.org/10.1021/la950887q>.
- [79] Y. Wang et al. "Lap shear of a soft and elastic adhesive". In: *Mechanics of Materials* 158 (2021), p. 103845. DOI: <https://doi.org/10.1016/j.mechmat.2021.103845>.
- [80] G.I. Barenblatt. "The mathematical theory of equilibrium cracks in brittle fracture". In: *Advances in applied mechanics* 7 (1962), pp. 55–129. DOI: [https://doi.org/10.1016/S0065-2156\(08\)70121-2](https://doi.org/10.1016/S0065-2156(08)70121-2).
- [81] M. Ortiz, Y. Leroy, and A. Needleman. "A finite element method for localized failure analysis". In: *Computer methods in applied mechanics and engineering* 61.2 (1987), pp. 189–214. DOI: [https://doi.org/10.1016/0045-7825\(87\)90004-1](https://doi.org/10.1016/0045-7825(87)90004-1).
- [82] V. Tvergaard. "Effect of fibre debonding in a whisker-reinforced metal". In: *Materials science and engineering: A* 125.2 (1990), pp. 203–213. DOI: [https://doi.org/10.1016/0921-5093\(90\)90170-8](https://doi.org/10.1016/0921-5093(90)90170-8).
- [83] P.H. Geubelle and J.S. Baylor. "Impact-induced delamination of composites: a 2D simulation". In: *Composites Part B: Engineering* 29.5 (1998), pp. 589–602. DOI: [https://doi.org/10.1016/S1359-8368\(98\)00013-4](https://doi.org/10.1016/S1359-8368(98)00013-4).

- [84] K. Willam and I. Rhee. "Interface damage model for thermomechanical degradation of heterogeneous materials". In: *Computer Methods in Applied Mechanics and Engineering* 193 (2004), pp. 3327–3350. DOI: <https://doi.org/10.1016/j.cma.2003.09.020>.
- [85] A. Caballero, K.J. Willam, and I. Carol. "Consistent tangent formulation for 3D interface modeling of cracking/fracture in quasi-brittle materials". In: *Computer Methods in Applied Mechanics and Engineering* 197 (2004), pp. 2804–2822. DOI: <https://doi.org/10.1016/j.cma.2008.01.011>.
- [86] D.H. Kaelble. "Theory and analysis of peel adhesion: bond stresses and distributions". In: *Transactions of the Society of Rheology* 4.1 (1960), pp. 45–73. DOI: [10.1088/0022-3727/8/13/005](https://doi.org/10.1088/0022-3727/8/13/005).
- [87] K. Kendall. "Thin-film peeling—the elastic term". In: *Journal of Physics D: Applied Physics* 8.13 (1975), p. 1449. DOI: [10.1088/0022-3727/8/13/005](https://doi.org/10.1088/0022-3727/8/13/005).
- [88] R. Villey et al. "In-situ measurement of the large strain response of the fibrillar debonding region during the steady peeling of pressure sensitive adhesives". In: *International Journal of Fracture* 204 (2017), pp. 175–190. DOI: <https://doi.org/10.1007/s10704-016-0171-1>.
- [89] I. Zreid, R. Fleischhauer, and M. Kaliske. "A thermomechanically coupled viscoelastic cohesive zone model at large deformation". In: *International Journal of Solids and Structures* 50.25-26 (2013), pp. 4279–4291. DOI: <https://doi.org/10.1016/j.ijsolstr.2013.08.031>.
- [90] A. Molinari and G. Ravichandran. "Peeling of elastic tapes: effects of large deformations, pre-straining, and of a peel-zone model". In: *The Journal of Adhesion* 84.12 (2008), pp. 961–995. DOI: <https://doi.org/10.1080/00218460802576995>.
- [91] M.J. Van den Bosch, P.J.G. Schreurs, and M. Geers. "A cohesive zone model with a large displacement formulation accounting for interfacial fibrillation". In: *European Journal of Mechanics-A/Solids* 26.1 (2007), pp. 1–19. DOI: <https://doi.org/10.1016/j.euromechsol.2006.09.003>.

- [92] J. Reinoso and M. Paggi. “A consistent interface element formulation for geometrical and material nonlinearities”. In: *Computational Mechanics* 54 (2014), pp. 1569–1581. DOI: <https://doi.org/10.1007/s00466-014-1077-2>.
- [93] Gregorio Mariggiò et al. “Peeling of thick adhesive interfaces: The role of dynamics and geometrical nonlinearity”. In: *Mechanics Research Communications* 94 (2018), pp. 21–27. DOI: <https://doi.org/10.1016/j.mechrescom.2018.08.018>.
- [94] M. Paggi and P. Wriggers. “Node-to-segment and node-to-surface interface finite elements for fracture mechanics”. In: *Computer Methods in Applied Mechanics and Engineering* 300 (2016), pp. 540–560. DOI: <https://doi.org/10.1016/j.cma.2015.11.023>.
- [95] L. Heepe and S.N. Gorb. “Biologically inspired mushroom-shaped adhesive microstructures”. In: *Annu. Rev. Mater. Res.* 44 (2014), pp. 173–203. DOI: <https://doi.org/10.1146/annurev-matsci-062910-100458>.
- [96] S. Gorb et al. “Biomimetic mushroom-shaped fibrillar adhesive microstructure”. In: *J. R. Soc. Interface* 4 (2007), pp. 271–275. DOI: <https://doi.org/10.1098/rsif.2006.0164>.
- [97] G. Carbone and E. Pierro. “A review of adhesion mechanisms of mushroom-shaped microstructured adhesives”. In: *Meccanica* 48 (2013), pp. 1819–1833. DOI: <https://doi.org/10.1007/s11012-013-9724-9>.
- [98] Y. Tian et al. “Adhesion and friction in gecko toe attachment and detachment”. In: *Proceedings of the National Academy of Sciences* 103.51 (2006), pp. 19320–19325. DOI: <https://doi.org/10.1073/pnas.0608841103>.
- [99] M.R. Marulli et al. “A finite element framework for the simulation of bio-inspired adhesives with mushroom-shaped microstructures”. In: *Mechanics Research Communications* 125 (2022). DOI: <https://doi.org/10.1016/j.mechrescom.2022.103963>.
- [100] N. Pugno et al. “Normal adhesive force-displacement curves of living geckos”. In: *Journal of Adhesion* 87 (2011), pp. 1059–1072. DOI: <https://doi.org/10.1080/00218464.2011.609439>.
- [101] D. Whitley. “A genetic algorithm tutorial”. In: *Statistics and computing* 4 (1994), pp. 65–85. DOI: <https://doi.org/10.1007/BF00175354>.

- [102] James Kennedy and Russell Eberhart. "Particle swarm optimization". In: *Proceedings of ICNN'95-international conference on neural networks*. Vol. 4. IEEE. 1995, pp. 1942–1948. DOI: [10.1109/ICNN.1995.488968](https://doi.org/10.1109/ICNN.1995.488968).
- [103] A.H. Gandomi, X.-S. Yang, and A.H. Alavi. "Cuckoo search algorithm: a metaheuristic approach to solve structural optimization problems". In: *Engineering with computers* 29 (2013), pp. 17–35. DOI: <https://doi.org/10.1007/s00366-011-0241-y>.
- [104] Y.M. Xie and G.P. Steven. "A simple evolutionary procedure for structural optimization". In: *Computers & structures* 49.5 (1993), pp. 885–896. DOI: [https://doi.org/10.1016/0045-7949\(93\)90035-c](https://doi.org/10.1016/0045-7949(93)90035-c).
- [105] R. Rao. "Jaya: A simple and new optimization algorithm for solving constrained and unconstrained optimization problems". In: *International Journal of Industrial Engineering Computations* 7.1 (2016), pp. 19–34. DOI: [10.5267/j.ijiec.2015.8.004](https://doi.org/10.5267/j.ijiec.2015.8.004).
- [106] Congjie Wei et al. "Data driven modeling of interfacial traction–separation relations using a thermodynamically consistent neural network". In: *Computer Methods in Applied Mechanics and Engineering* 404 (2023), p. 115826. DOI: <https://doi.org/10.1016/j.cma.2022.115826>.
- [107] Sanjida Ferdousi et al. "Characterize traction–separation relation and interfacial imperfections by data-driven machine learning models". In: *Scientific Reports* 11.1 (2021), p. 14330. DOI: <https://doi.org/10.1038/s41598-021-93852-y>.
- [108] Agathe Jaillon et al. "Mode I cohesive zone model parameters identification and comparison of measurement techniques based on uncertainty estimation". In: *International Journal of Solids and Structures* 191 (2020), pp. 577–587. DOI: <https://doi.org/10.1016/j.ijsolstr.2019.12.014>.
- [109] Shengjun Zhao et al. "Using Machine Learning and Finite Element Analysis to Extract Traction-Separation Relations at Bonding Wire Interfaces of Insulated Gate Bipolar Transistor Modules". In: *Materials* 17.5 (2024), p. 1002. DOI: [10.3390/ma17051002](https://doi.org/10.3390/ma17051002).
- [110] Dong Chen et al. "Efficient parameters identification of a modified GTN model of ductile fracture using machine learning". In: *Engineering Fracture Mechanics* 245 (2021), p. 107535. DOI: <https://doi.org/10.1016/j.engfracmech.2021.107535>.

- [111] Jia Zhang, Jinxi Zhang, and Dandan Cao. “Genetic algorithm optimization for cohesive zone modeling of viscoelastic asphalt mixture fracture based on SCB test”. In: *Engineering Fracture Mechanics* 271 (2022), p. 108663. DOI: <https://doi.org/10.1016/j.engfracmech.2022.108663>.
- [112] AB De Morais et al. “Bilinear approximations to the mixed-mode I–II delamination cohesive law using an inverse method”. In: *Composite Structures* 122 (2015), pp. 361–366. DOI: <https://doi.org/10.1016/j.compstruct.2014.11.058>.
- [113] Tianxiang Shi et al. “Inverse parameter identification framework for cohesive zone models based on multi-island genetic algorithm”. In: *Engineering Fracture Mechanics* 300 (2024), p. 110005. DOI: <https://doi.org/10.1016/j.engfracmech.2024.110005>.
- [114] ZHU Jihong et al. “A review of topology optimization for additive manufacturing: Status and challenges”. In: *Chinese Journal of Aeronautics* 34.1 (2021), pp. 91–110. DOI: <https://doi.org/10.1016/j.cja.2020.09.020>.
- [115] János Plocher and Ajit Panesar. “Review on design and structural optimisation in additive manufacturing: Towards next-generation lightweight structures”. In: *Materials & Design* 183 (2019), p. 108164. DOI: <https://doi.org/10.1016/j.matdes.2019.108164>.
- [116] Nurhalida Shahrubudin, Te Chuan Lee, and RJPM Ramlan. “An overview on 3D printing technology: Technological, materials, and applications”. In: *Procedia Manufacturing* 35 (2019), pp. 1286–1296. DOI: <https://doi.org/10.1016/j.promfg.2019.06.089>.
- [117] Vítor Alcácer and Virgílio Cruz-Machado. “Scanning the industry 4.0: A literature review on technologies for manufacturing systems”. In: *Engineering science and technology, an international journal* 22.3 (2019), pp. 899–919. DOI: <https://doi.org/10.1016/j.jestch.2019.01.006>.
- [118] Monica Bordegoni and Caterina Rizzi. *Innovation in product design: from CAD to virtual prototyping*. 2011. DOI: <https://doi.org/10.1007/978-0-85729-775-4>.
- [119] M.P. Bendsøe. “Optimal shape design as a material distribution problem”. In: *Structural optimization* 1 (1989), pp. 193–202. DOI: <https://doi.org/10.1007/BF01650949>.

- [120] M.P. Bendsøe and O. Sigmund. “Material interpolation schemes in topology optimization”. In: *Archive of applied mechanics* 69 (1999), pp. 635–654. DOI: <https://doi.org/10.1007/s004190050248>.
- [121] D Nha Chu et al. “Evolutionary structural optimization for problems with stiffness constraints”. In: *Finite elements in analysis and design* 21.4 (1996), pp. 239–251. DOI: [https://doi.org/10.1016/0168-874X\(95\)00043-S](https://doi.org/10.1016/0168-874X(95)00043-S).
- [122] Q. Li, G.P. Steven, and Y.M. Xie. “A simple checkerboard suppression algorithm for evolutionary structural optimization”. In: *Structural and Multidisciplinary Optimization* 22 (2001), pp. 230–239. DOI: <https://doi.org/10.1007/s001580100140>.
- [123] Xiaodong Huang and Mike Xie. *Evolutionary topology optimization of continuum structures: methods and applications*. John Wiley & Sons, 2010.
- [124] J.A. Sethian and A. Wiegmann. “Structural boundary design via level set and immersed interface methods”. In: *Journal of computational physics* 163.2 (2000), pp. 489–528. DOI: <https://doi.org/10.1006/jcph.2000.6581>.
- [125] Xiaodong Huang and YM Xie. “Topology optimization of nonlinear structures under displacement loading”. In: *Engineering structures* 30.7 (2008), pp. 2057–2068. DOI: <https://doi.org/10.1016/j.engstruct.2008.01.009>.
- [126] Majid Movahedi Rad, Muayad Habashneh, and Janos Logo. “Elasto-Plastic limit analysis of reliability based geometrically nonlinear bi-directional evolutionary topology optimization”. In: *Structures*. Vol. 34. 2021, pp. 1720–1733. DOI: <https://doi.org/10.1016/j.istruc.2021.08.105>.
- [127] Felix Fritzen et al. “Topology optimization of multiscale elastoviscoplastic structures”. In: *International Journal for Numerical Methods in Engineering* 106.6 (2016), pp. 430–453. DOI: <https://doi.org/10.1002/nme.5122>.
- [128] Qi Xia and Michael Yu Wang. “Topology optimization of thermoelastic structures using level set method”. In: *Computational Mechanics* 42 (2008), pp. 837–857. DOI: <https://doi.org/10.1007/s00466-008-0287-x>.

- [129] Vahid Shobeiri. "The topology optimization design for cracked structures". In: *Engineering Analysis with Boundary Elements* 58 (2015), pp. 26–38. DOI: <https://doi.org/10.1016/j.enganabound.2015.03.002>.
- [130] Gilles A Francfort and J-J Marigo. "Revisiting brittle fracture as an energy minimization problem". In: *Journal of the Mechanics and Physics of Solids* 46.8 (1998), pp. 1319–1342. DOI: [https://doi.org/10.1016/S0022-5096\(98\)00034-9](https://doi.org/10.1016/S0022-5096(98)00034-9).
- [131] Blaise Bourdin, Gilles A Francfort, and Jean-Jacques Marigo. "The variational approach to fracture". In: *Journal of elasticity* 91 (2008), pp. 5–148. DOI: <https://doi.org/10.1007/s10659-007-9107-3>.
- [132] Alan Arnold Griffith. "VI. The phenomena of rupture and flow in solids". In: *Philosophical transactions of the royal society of london. Series A, containing papers of a mathematical or physical character* 221.582-593 (1921), pp. 163–198. DOI: <https://doi.org/10.1098/rsta.1921.0006>.
- [133] Christian Linder and Francisco Armero. "Finite elements with embedded strong discontinuities for the modeling of failure in solids". In: *International Journal for Numerical Methods in Engineering* 72.12 (2007), pp. 1391–1433. DOI: <https://doi.org/10.1002/nme.2042>.
- [134] JUAN CARLOS Simo, JAVIER Oliver, and Francisco Armero. "An analysis of strong discontinuities induced by strain-softening in rate-independent inelastic solids". In: *Computational mechanics* 12.5 (1993), pp. 277–296. DOI: <https://doi.org/10.1007/BF00372173>.
- [135] John Dolbow, Nicolas Moës, and Ted Belytschko. "An extended finite element method for modeling crack growth with frictional contact". In: *Computer methods in applied Mechanics and engineering* 190.51-52 (2001), pp. 6825–6846. DOI: [https://doi.org/10.1016/S0045-7825\(01\)00260-2](https://doi.org/10.1016/S0045-7825(01)00260-2).
- [136] Nicolas Moës, John Dolbow, and Ted Belytschko. "A finite element method for crack growth without remeshing". In: *International journal for numerical methods in engineering* 46.1 (1999), pp. 131–150. DOI: [https://doi.org/10.1002/\(SICI\)1097-0207\(19990910\)46:1<131::AID-NME726>3.0.CO;2-J](https://doi.org/10.1002/(SICI)1097-0207(19990910)46:1<131::AID-NME726>3.0.CO;2-J).

- [137] Jean Lemaitre and Rodrigue Desmorat. *Engineering damage mechanics: ductile, creep, fatigue and brittle failures*. Springer Science & Business Media, 2006.
- [138] Valerio Carollo et al. “Recent advancements on the phase field approach to brittle fracture for heterogeneous materials and structures”. In: *Advanced modeling and simulation in engineering sciences* 5 (2018), pp. 1–29. DOI: <https://doi.org/10.1186/s40323-018-0102-y>.
- [139] Riccardo Cavuoto et al. “Failure through crack propagation in components with holes and notches: An experimental assessment of the phase field model”. In: *International Journal of Solids and Structures* 257 (2022), p. 111798. DOI: <https://doi.org/10.1016/j.ijsolstr.2022.111798>.
- [140] Zeng Liu, J Reinoso, and Marco Paggi. “Phase field modeling of brittle fracture in large-deformation solid shells with the efficient quasi-Newton solution and global–local approach”. In: *Computer Methods in Applied Mechanics and Engineering* 399 (2022), p. 115410. DOI: <https://doi.org/10.1016/j.cma.2022.115410>.
- [141] Aditya Kumar et al. “Revisiting nucleation in the phase-field approach to brittle fracture”. In: *Journal of the Mechanics and Physics of Solids* 142 (2020), p. 104027. DOI: <https://doi.org/10.1016/j.jmps.2020.104027>.
- [142] Michael J Borden et al. “A phase-field formulation for fracture in ductile materials: Finite deformation balance law derivation, plastic degradation, and stress triaxiality effects”. In: *Computer Methods in Applied Mechanics and Engineering* 312 (2016), pp. 130–166. DOI: <https://doi.org/10.1016/j.cma.2016.09.005>.
- [143] Cunyi Li et al. “Phase field fracture in elasto-plastic solids: Incorporating phenomenological failure criteria for ductile materials”. In: *Computer Methods in Applied Mechanics and Engineering* 391 (2022), p. 114580. DOI: <https://doi.org/10.1016/j.cma.2022.114580>.
- [144] Riccardo Cavuoto et al. “Phase-field modelling of failure in ceramics with multiscale porosity”. In: *Materials & Design* 238 (2024), p. 112708. DOI: <https://doi.org/10.1016/j.matdes.2024.112708>.

- [145] Pavan Kumar Asur Vijaya Kumar et al. "A phase-field fracture model for fatigue using locking-free solid shell finite elements: Analysis for homogeneous materials and layered composites". In: *Theoretical and Applied Fracture Mechanics* 127 (2023), p. 104029. DOI: <https://doi.org/10.1016/j.tafmec.2023.104029>.
- [146] Marlini Simoes and Emilio Martinez-Paneda. "Phase field modelling of fracture and fatigue in Shape Memory Alloys". In: *Computer Methods in Applied Mechanics and Engineering* 373 (2021), p. 113504. DOI: <https://doi.org/10.1016/j.cma.2020.113504>.
- [147] Pietro Carrara et al. "A framework to model the fatigue behavior of brittle materials based on a variational phase-field approach". In: *Computer Methods in Applied Mechanics and Engineering* 361 (2020), p. 112731. DOI: <https://doi.org/10.1016/j.cma.2019.112731>.
- [148] Daicong Da and Julien Yvonnet. "Topology optimization for maximizing the fracture resistance of periodic quasi-brittle composites structures". In: *Materials* 13.15 (2020), p. 3279. DOI: <https://doi.org/10.3390/ma13153279>.
- [149] Bingbing San and Haim Waisman. "Optimization of carbon black polymer composite microstructure for rupture resistance". In: *Journal of Applied Mechanics* 84.2 (2017), p. 021005. DOI: <https://doi.org/10.1115/1.4035050>.
- [150] Pengfei Li, Julien Yvonnet, and Yi Wu. "Improved fracture resistance of 3D-printed elastoplastic structures with respect to their topology and orientation of deposited layers". In: *International Journal of Mechanical Sciences* 220 (2022), p. 107147. DOI: <https://doi.org/10.1016/j.ijmecsci.2022.107147>.
- [151] Kai A James and Haim Waisman. "Failure mitigation in optimal topology design using a coupled nonlinear continuum damage model". In: *Computer methods in applied mechanics and engineering* 268 (2014), pp. 614–631. DOI: <http://dx.doi.org/10.1016/j.cma.2013.10.022>.
- [152] Liang Xia, Daicong Da, and Julien Yvonnet. "Topology optimization for maximizing the fracture resistance of quasi-brittle composites". In: *Computer Methods in Applied Mechanics and Engineering* 332 (2018), pp. 234–254. DOI: <https://doi.org/10.1016/j.cma.2017.12.021>.

- [153] Pengfei Li, Yi Wu, and Julien Yvonnet. "A SIMP-phase field topology optimization framework to maximize quasi-brittle fracture resistance of 2D and 3D composites". In: *Theoretical and applied fracture mechanics* 114 (2021), p. 102919. DOI: <https://doi.org/10.1016/j.tafmec.2021.102919>.
- [154] Pavan Kumar Asur Vijaya Kumar et al. "SIMP Phase-field topology optimization framework to maximize fracture resistance in FGMs". In: *Composite Structures* 329 (2024), p. 117750. DOI: <https://doi.org/10.1016/j.compstruct.2023.117750>.
- [155] Yi Wu et al. "Topology optimization for enhanced dynamic fracture resistance of structures". In: *Computer Methods in Applied Mechanics and Engineering* 394 (2022), p. 114846. DOI: <https://doi.org/10.1016/j.cma.2022.114846>.
- [156] Muayad Habashneh and Majid Movahedi Rad. "Optimizing structural topology design through consideration of fatigue crack propagation". In: *Computer Methods in Applied Mechanics and Engineering* 419 (2024), p. 116629. DOI: <https://doi.org/10.1016/j.cma.2023.116629>.
- [157] Jonathan B Russ and Haim Waisman. "Topology optimization for brittle fracture resistance". In: *Computer Methods in Applied Mechanics and Engineering* 347 (2019), pp. 238–263. DOI: <https://doi.org/10.1016/j.cma.2018.12.031>.
- [158] Jonathan B Russ and Haim Waisman. "A novel topology optimization formulation for enhancing fracture resistance with a single quasi-brittle material". In: *International Journal for Numerical Methods in Engineering* 121.13 (2020), pp. 2827–2856. DOI: <https://doi.org/10.1002/nme.6334>.
- [159] A Sohouli et al. "Continuous density-based topology optimization of cracked structures using peridynamics". In: *Structural and Multidisciplinary Optimization* 62 (2020), pp. 2375–2389. DOI: <https://doi.org/10.1007/s00158-020-02608-1>.
- [160] Anahita Habibian et al. "Multi-material topology optimization of structures with discontinuities using Peridynamics". In: *Composite Structures* 258 (2021), p. 113345. DOI: <https://doi.org/10.1016/j.compstruct.2020.113345>.

- [161] Thanh T Banh and Dongkyu Lee. “Multi-material topology optimization design for continuum structures with crack patterns”. In: *Composite Structures* 186 (2018), pp. 193–209. DOI: <https://doi.org/10.1016/j.compstruct.2017.11.088>.
- [162] Nima Nohi, Hassan Ali Jahangiry, and Haim Waisman. “Level-set topology optimization for ductile and brittle fracture resistance using the phase-field method”. In: *Computer Methods in Applied Mechanics and Engineering* 409 (2023), p. 115963. DOI: <https://doi.org/10.1016/j.cma.2023.115963>.
- [163] Daicong Da et al. “Topology optimization of particle-matrix composites for optimal fracture resistance taking into account interfacial damage”. In: *International Journal for Numerical Methods in Engineering* 115.5 (2018), pp. 604–626. DOI: <https://doi.org/10.1002/nme.5818>.
- [164] E. Andreassen et al. “Efficient topology optimization in MATLAB using 88 lines of code”. In: *Structural and Multidisciplinary Optimization* 43 (2011), pp. 1–16. DOI: <https://doi.org/10.1007/s00158-010-0594-7>.
- [165] K. Svanberg. “The method of moving asymptotes—a new method for structural optimization”. In: *International journal for numerical methods in engineering* 24.2 (1987), pp. 359–373. DOI: <https://doi.org/10.1002/nme.1620240207>.
- [166] R. Behrou, M. Lawry, and K. Maute. “Level set topology optimization of structural problems with interface cohesion”. In: *International Journal for Numerical Methods in Engineering* 112.8 (2017), pp. 990–1016. DOI: <https://doi.org/10.1002/nme.5540>.
- [167] A. Clausen, N. Aage, and O. Sigmund. “Topology optimization of coated structures and material interface problems”. In: *Computer Methods in Applied Mechanics and Engineering* 290 (2015), pp. 524–541. DOI: <https://doi.org/10.1016/j.cma.2015.02.011>.
- [168] F.J. Fernandes and R. Pavanollo. “Topology optimization of adhesive material in a single lap joint using an evolutionary structural optimization method and a cohesive zone model as failure criterion”. In: *Proceedings of the Institution of Mechanical Engineers, Part L: Journal of Materials: Design and Applications* 236.4 (2022), pp. 757–778. DOI: <https://doi.org/10.1177/14644207211056945>.

- [169] P. Liu, Y. Luo, and Z. Kang. “Multi-material topology optimization considering interface behavior via XFEM and level set method”. In: *Computer methods in applied mechanics and engineering* 308 (2016), pp. 113–133. DOI: <https://doi.org/10.1016/j.cma.2016.05.016>.
- [170] M.P. Bendsøe and N. Kikuchi. “Generating optimal topologies in structural design using a homogenization method”. In: *Computer methods in applied mechanics and engineering* 71.2 (1988), pp. 197–224. DOI: [https://doi.org/10.1016/0045-7825\(88\)90086-2](https://doi.org/10.1016/0045-7825(88)90086-2).
- [171] O. Sigmund. “A 99 line topology optimization code written in Matlab”. In: *Structural and multidisciplinary optimization* 21.2 (2001), pp. 120–127. DOI: <https://doi.org/10.1007/s001580050176>.
- [172] Hongshi Ruan et al. “Biomimicry and topology optimization for adhesive toughness design in bonded heterogeneous films”. In: *International Journal of Adhesion and Adhesives* 132 (2024), p. 103684. DOI: <https://doi.org/10.1016/j.ijadhadh.2024.103684>.
- [173] P.K.A.V. Kumar et al. “SIMP Phase-field topology optimization framework to maximize fracture resistance in FGMs”. In: *Composite Structures* 329 (2024), p. 117750. DOI: <https://doi.org/10.1016/j.compstruct.2023.117750>.
- [174] Blaise Bourdin, Gilles A Francfort, and Jean-Jacques Marigo. “Numerical experiments in revisited brittle fracture”. In: *Journal of the Mechanics and Physics of Solids* 48.4 (2000), pp. 797–826. DOI: [https://doi.org/10.1016/S0022-5096\(99\)00028-9](https://doi.org/10.1016/S0022-5096(99)00028-9).
- [175] Eric Lorentz, Sam Cuvilliez, and Kyrlyo Kazymyrenko. “Modelling large crack propagation: from gradient damage to cohesive zone models”. In: *International journal of fracture* 178.1 (2012), pp. 85–95. DOI: <https://doi.org/10.1007/s10704-012-9746-7>.
- [176] JL Boldrini et al. “A non-isothermal thermodynamically consistent phase field framework for structural damage and fatigue”. In: *Computer Methods in Applied Mechanics and Engineering* 312 (2016), pp. 395–427. DOI: <https://doi.org/10.1016/j.cma.2016.08.030>.

- [177] Jian-Ying Wu. “A unified phase-field theory for the mechanics of damage and quasi-brittle failure”. In: *Journal of the Mechanics and Physics of Solids* 103 (2017), pp. 72–99. DOI: <https://doi.org/10.1016/j.jmps.2017.03.015>.
- [178] Giovanni Lancioni and Gianni Royer-Carfagni. “The variational approach to fracture mechanics. A practical application to the French Panthéon in Paris”. In: *Journal of elasticity* 95 (2009), pp. 1–30. DOI: <https://doi.org/10.1007/s10659-009-9189-1>.
- [179] Hanen Amor, Jean-Jacques Marigo, and Corrado Maurini. “Regularized formulation of the variational brittle fracture with unilateral contact: Numerical experiments”. In: *Journal of the Mechanics and Physics of Solids* 57.8 (2009), pp. 1209–1229. DOI: <https://doi.org/10.1016/j.jmps.2009.04.011>.
- [180] Jian-Ying Wu. “A unified phase-field theory for the mechanics of damage and quasi-brittle failure”. In: *Journal of the Mechanics and Physics of Solids* 103 (2017), pp. 72–99. DOI: <https://doi.org/10.1016/j.jmps.2017.03.015>.
- [181] Andrea Braides. *Approximation of free-discontinuity problems*. 1694. 1998. DOI: <https://doi.org/10.1007/BFb0097344>.
- [182] Siobhan Burke, Christoph Ortner, and Endre Süli. “An adaptive finite element approximation of a generalized Ambrosio–Tortorelli functional”. In: *Mathematical Models and Methods in Applied Sciences* 23.09 (2013), pp. 1663–1697. DOI: <https://doi.org/10.1142/S021820251350019X>.
- [183] Thomas JR Hughes, John A Cottrell, and Yuri Bazilevs. “Isogeometric analysis: CAD, finite elements, NURBS, exact geometry and mesh refinement”. In: *Computer methods in applied mechanics and engineering* 194.39-41 (2005), pp. 4135–4195. DOI: <https://doi.org/10.1016/j.cma.2004.10.008>.
- [184] Christian Miehe, Lisa-Marie Schaezel, and Heike Ulmer. “Phase field modeling of fracture in multi-physics problems. Part I. Balance of crack surface and failure criteria for brittle crack propagation in thermo-elastic solids”. In: *Computer Methods in Applied Mechanics and Engineering* 294 (2015), pp. 449–485. DOI: <https://doi.org/10.1016/j.cma.2014.11.016>.

- [185] Thanh Tung Nguyen et al. "A phase field method to simulate crack nucleation and propagation in strongly heterogeneous materials from direct imaging of their microstructure". In: *Engineering Fracture Mechanics* 139 (2015), pp. 18–39. DOI: <https://doi.org/10.1016/j.engfracmech.2015.03.045>.
- [186] Herbert Baaser. *Development and Application of the Finite Element Method based on MATLAB*. Springer Science & Business Media, 2010. DOI: [10.1007/978-3-642-13152-3](https://doi.org/10.1007/978-3-642-13152-3).
- [187] O. Rabinovitch. "Debonding analysis of fiber-reinforced-polymer strengthened beams: Cohesive zone modeling versus a linear elastic fracture mechanics approach". In: *Engineering Fracture Mechanics* 75.10 (2008), pp. 2842–2859. DOI: <https://doi.org/10.1016/j.engfracmech.2008.01.003>.
- [188] Mohamed Abdel-Basset, Laila Abdel-Fatah, and Arun Kumar Sangai. "Metaheuristic algorithms: A comprehensive review". In: *Computational intelligence for multimedia big data on the cloud with engineering applications* (2018), pp. 185–231. DOI: <https://doi.org/10.1016/B978-0-12-813314-9.00010-4>.
- [189] Xin-She Yang. *Nature-inspired metaheuristic algorithms*. Luniver press, 2010.
- [190] Amir Hossein Gandomi et al. "Metaheuristic algorithms in modeling and optimization". In: *Metaheuristic applications in structures and infrastructures* 1 (2013), pp. 1–24.
- [191] Maurice Clerc. "The swarm and the queen: towards a deterministic and adaptive particle swarm optimization". In: *Proceedings of the 1999 congress on evolutionary computation-CEC99 (Cat. No. 99TH8406)*. Vol. 3. IEEE, 1999, pp. 1951–1957. DOI: [10.1109/CEC.2000.870279](https://doi.org/10.1109/CEC.2000.870279).
- [192] SN Sivanandam et al. *Genetic algorithms*. 2008. DOI: https://doi.org/10.1007/978-3-540-73190-0_2.
- [193] Dervis Karaboga and Bahriye Basturk. "A powerful and efficient algorithm for numerical function optimization: artificial bee colony (ABC) algorithm". In: *Journal of global optimization* 39 (2007), pp. 459–471. DOI: <https://doi.org/10.1007/s10898-007-9149-x>.

- [194] R Venkata Rao and R Venkata Rao. *Teaching-learning-based optimization algorithm*. 2016. DOI: https://doi.org/10.1007/978-3-319-22732-0_2.
- [195] R Venkata Rao and Vivek Patel. "An improved teaching-learning-based optimization algorithm for solving unconstrained optimization problems". In: *Scientia Iranica* 20.3 (2013), pp. 710–720. DOI: <https://doi.org/10.1016/j.scient.2012.12.005>.
- [196] Russ C Eberhart and Yuhui Shi. "Comparing inertia weights and constriction factors in particle swarm optimization". In: *Proceedings of the 2000 congress on evolutionary computation. CEC00 (Cat. No. 00TH8512)*. Vol. 1. IEEE. 2000, pp. 84–88. DOI: <https://doi.org/10.1016/j.ijsolstr.2022.111798>.
- [197] T. Bäck and H.-P. Schwefel. "An overview of evolutionary algorithms for parameter optimization". In: *Evolutionary computation* 1.1 (1993), pp. 1–23. DOI: [10.1162/evco.1993.1.1.1](https://doi.org/10.1162/evco.1993.1.1.1).
- [198] O. Sigmund. "Materials with prescribed constitutive parameters: an inverse homogenization problem". In: *International Journal of Solids and Structures* 31.17 (1994), pp. 2313–2329. DOI: [https://doi.org/10.1016/0020-7683\(94\)90154-6](https://doi.org/10.1016/0020-7683(94)90154-6).
- [199] O. Sigmund. "Morphology-based black and white filters for topology optimization". In: *Structural and Multidisciplinary Optimization* 33.4 (2007), pp. 401–424. DOI: <https://doi.org/10.1007/s00158-006-0087-x>.
- [200] T.E. Bruns and D.A. Tortorelli. "Topology optimization of nonlinear elastic structures and compliant mechanisms". In: *Computer methods in applied mechanics and engineering* 190.26-27 (2001), pp. 3443–3459. DOI: [https://doi.org/10.1016/S0045-7825\(00\)00278-4](https://doi.org/10.1016/S0045-7825(00)00278-4).
- [201] H. Wang, J. Liu, and G. Wen. "An efficient evolutionary structural optimization method for multi-resolution designs". In: *Structural and Multidisciplinary Optimization* 62 (2020), pp. 787–803. DOI: <https://doi.org/10.1007/s00158-020-02536-0>.
- [202] E. Biyikli and A.C. To. "Proportional topology optimization: a new non-sensitivity method for solving stress constrained and minimum compliance problems and its implementation in MATLAB". In: *PloS one* 10.12 (2015), e0145041. DOI: <https://doi.org/10.1371/journal.pone.0145041>.

- [203] C. Geuzaine and J.-F. Remacle. "Gmsh: A 3-D finite element mesh generator with built-in pre-and post-processing facilities". In: *International journal for numerical methods in engineering* 79.11 (2009), pp. 1309–1331. DOI: <https://doi.org/10.1002/nme.2579>.
- [204] U. Ayachit. *The paraview guide: a parallel visualization application*. Kitware, Inc., 2015.
- [205] Angel R Torrado et al. "Characterizing the effect of additives to ABS on the mechanical property anisotropy of specimens fabricated by material extrusion 3D printing". In: *Additive Manufacturing* 6 (2015), pp. 16–29. DOI: <https://doi.org/10.1016/j.addma.2015.02.001>.
- [206] Kim Pham et al. "Gradient damage models and their use to approximate brittle fracture". In: *International Journal of Damage Mechanics* 20.4 (2011), pp. 618–652. DOI: <https://doi.org/10.1177/1056789510386852>.
- [207] Tushar Kanti Mandal, Vinh Phu Nguyen, and Jian-Ying Wu. "Length scale and mesh bias sensitivity of phase-field models for brittle and cohesive fracture". In: *Engineering Fracture Mechanics* 217 (2019), p. 106532. DOI: <https://doi.org/10.1016/j.engfracmech.2019.106532>.
- [208] Omar A Mohamed, Syed H Masood, and Jahar L Bhowmik. "Optimization of fused deposition modeling process parameters: a review of current research and future prospects". In: *Advances in manufacturing* 3 (2015), pp. 42–53. DOI: <https://doi.org/10.1007/s40436-014-0097-7>.
- [209] George R Irwin. "Analysis of stresses and strains near the end of a crack traversing a plate". In: (1957). DOI: <https://doi.org/10.1115/1.4011547>.
- [210] Sundararajan Natarajan, Ratna Kumar Annabattula, et al. "Modeling crack propagation in variable stiffness composite laminates using the phase field method". In: *Composite Structures* 209 (2019), pp. 424–433. DOI: <https://doi.org/10.1016/j.compstruct.2018.10.083>.
- [211] Thanh Tung Nguyen, Julien Réthoré, and Marie-Christine Baietto. "Phase field modelling of anisotropic crack propagation". In: *European Journal of Mechanics-A/Solids* 65 (2017), pp. 279–288. DOI: <http://dx.doi.org/10.1016/j.euromechsol.2017.05.002>.



Unless otherwise expressly stated, all original material of whatever nature created by Tota Rakesh Kumar and included in this thesis, is licensed under a Creative Commons Attribution Noncommercial Share Alike 3.0 Italy License.

Check on Creative Commons site:

<https://creativecommons.org/licenses/by-nc-sa/3.0/it/legalcode/>

<https://creativecommons.org/licenses/by-nc-sa/3.0/it/deed.en>

Ask the author about other uses.